This is to certify that the

dissertation entitled

INVESTIGATION OF HYDROBORATION AND METAL–BORON BOND FORMATION IN EARLY TRANSITION METAL BENT METALLOCENE SYSTEMS

presented by

DEAN R. LANTERO

has been accepted towards fulfillment
of the requirements for

_____Ph.D._____ degree in __CHEMISTRY__

_____
Major professor

Date __May 14, 1999_____

O-12771

PLACE IN RETURN BOX to remove this checkout from your record.
TO AVOID FINES return on or before date due.
MAY BE RECALLED with earlier due date if requested.

DATE DUE	DATE DUE	DATE DUE

INVESTIGATION OF HYDROBORATION AND METAL–BORON BOND FORMATION IN EARLY TRANSITION METAL BENT METALLOCENE SYSTEMS

By

Dean R. Lantero

A DISSERTATION

Submitted to
Michigan State University
in partial fulfillment of the requirements
for the degree of

DOCTOR OF PHILOSOPHY

Department of Chemistry

1999

ABSTRACT

INVESTIGATION OF HYDROBORATION AND METAL–BORON BOND FORMATION IN EARLY TRANSITION METAL BENT METALLOCENE SYSTEMS

By

Dean R. Lantero

Hydroboration of unsaturated organic substrates under catalytic conditions is accomplished with the use of transition metal systems. Most of the known transition metal boron complexes, which are proposed hydroboration intermediates, have contained a late transition metal often supported with phosphine ligands. The lack of early transition metal–boron complexes prompted study within the well understood bent metallocene framework. Judicious use of early transition metals within the bent metallocene framework, Cp'_2M (Cp' = cyclopentadienyl (Cp) or pentamethylcyclopentadienyl (Cp*); M = Nb or Ta), has led to accessible early transition metal complexes that display unique structural connectivity and interesting chemical reactivity.

Two primary synthetic methodologies have been investigated for metal–boron bond formation. The first method involved the reaction of an anionic metal complex, $\{Cp_2TaH_2Li\}_x$, with a haloborane, B–chlorocatecholborane (Cl–BCat) to form $Cp_2TaH_2(BCat)$. NMR spectroscopy revealed the formation of two isomers, *exo* and *endo*–$Cp_2TaH_2(BCat)$, in which the BCat fragment occupies the outer and central positions of the metallocene wedge, respectively. For the first time, group 5 regioisomers have been successfully separated and structurally characterized.

The second method involves the reaction of olefin hydride complexes $Cp'_2MH(\eta^2-CH_2=CH(R))$ (R = H or CH_3) with substituted catecholboranes (HBCat') and pinacolborane (HBPin) yielding complexes with the general formulae $Cp'_2M(H_2B(OR)_2)$ $((OR)_2 =$ Cat' or Pin). Products unique to the individual metals are isolated when Cp* ligands are employed. Niobium complexes ligated with Cp* form metal–boron compounds best described as "borane adducts" of "$Cp*_2NbH$" while the tantalum complexes are best described as Ta^V metal–dihydridoboryls based on NMR spectroscopy, X–ray crystallography and reactivity.

The Cp based metallocenes also yield compounds whose distinct reactivity and structural characteristics are dependent upon the transition metal. A new niobium diboryl, $Cp_2NbH(BCat)_2$, as well as $Cp_2NbH_2(BCat)$ are produced and isolated from the reaction of $Cp_2NbH(\eta^2-CH_2=CH(R))$ with HBCat. Detailed ^1H NMR studies of this reaction, at low temperatures, revealed the presence of an intermediate which isomerized to $Cp_2NbH_2(BCat)$ upon warming. Kinetic studies revealed independent pathways operate for the formation of each niobium boron compound. ^1H and ^{11}B NMR spectroscopy and X–ray crystallography support the formulation of $Cp_2NbH(BCat)_2$ as a Nb^V hydrido diboryl complex. The analogous reaction with the tantalum olefin complex yielded the aforementioned endo–$Cp_2TaH_2(BCat)$. Deuterium labeling, utilizing DBCat, provided valuable insight in the mechanisms operating for these systems.

$Cp*_2M(H_2BCat')$ compounds react cleanly with CO forming HBCat' and $Cp*_2MH(CO)$. The clean reactivity, observed over a range of temperatures, allowed kinetic studies to be performed. The activation parameters, $\Delta H^{\ddagger}$ and $\Delta S^{\ddagger}$, are consistent with a preequilibrium step in the Nb system and a three center intermediate in the Ta system. Isotopic substitution at the hydride positions yielded an inverse isotope effect ($k_H/k_D < 1$) for both metal boron complexes.

ACKNOWLEDGMENTS

A project of this magnitude is simply not complete by one's self: there is much time and effort put forth by others that has resulted in a successful conclusion of this undertaking, and for that I am deeply grateful. I would like to thank Mitch for the opportunity to learn chemistry from a gifted scientist and the chance to investigate some really remarkable compounds. But probably more importantly, teaching the qualities necessary to pursue the truth in chemistry. Carl, Doug and Baixin were crucial in keeping the atmosphere in the lab fun and to the other group members who would always offer advice, make suggestions and listen at times to incoherent ramblings. My many new friends were instrumental in making graduate school a much more enjoyable endeavor. Special thanks to the guys in the NMR facility, who were always willing to try an new experiment and the glass shop guys who always seemed to find a way to get it fixed by the next day. Finally, and most importantly, to my parents and sister who supported me through the entire process.

TABLE OF CONTENTS

LIST OF TABLES

LIST OF FIGURES

ix

LIST OF SYMBOLS AND ABBREVIATIONS

Å	Angstrom
BDE	Bond dissociation energy
Cat	$1,2-O_2C_6H_4^{2-}$
cm^{-1}	wave number
Cp	$\eta^5-C_5H_5$ (cyclopentadienyl)
Cp*	$\eta^5-C_5(CH_3)_5$ (pentamethylcyclopentadienyl)
d	day
d	doublet
D	Deuterium
d_x	deuterium substitution (x = number of substitutions)
e.u.	entropy units
endo	the "inner" position of the metallocene wedge
exo	the two "outer" positions of the metallocene wedge
h	hour
HBCat	catecholborane
HBPin	pinacolborane
J	coupling constant
m	multiplet
NOESY	Nuclear Overhauser Exchange Spectroscopy
ORTEP	Oak Ridge Thermal Ellipsoid Plot
Pin	$1,2-O_2C_2Me_4^{2-}$
ppb	parts per billion
psi	pounds per square inch
^tBu	*tert* butyl

$\Delta H^{\ddagger}$	change in enthalpy
$\Delta S^{\ddagger}$	change in entropy
Tp	hydridotris(pyrazolyl)borate ligand
$\Delta \nu_{1/2}$	full width at half height
δ	ppm (parts per million)
μ	reduced mass $m_1 m_2/(m_1 + m_2)$
ν	frequency

CHAPTER 1

INTRODUCTION

Reasons For Studying Metal–Boron Chemistry

While a wealth of chemistry involving metallacarborane complexes exists, [1] considerably less is known concerning simple boron bonds between transition metals, particularly when contrasted to the chemistry of metal–carbon, metal–nitrogen and metal–oxygen bonds. In stark contrast to chemistry of metal–carbon bonds, entire classes of metalloboron compounds have not yet been discovered. For instance, there are no examples of homoleptic boryl complexes and only recently has a terminal metal–borylene been reported.[2] This is somewhat surprising since metal alkyl, alkylidene and alkylidyne compounds are well known, and a terminal carbide has recently been reported as well.[3]

The development of metalloboron compounds is of interest a variety of reasons, both fundamental and practical. A practical reason for studying metal–boron interactions is their role in metal–mediated/catalyzed hydroboration reactions[4-6] and cross–coupling reactions of organic halides and boronic esters.[7,8] An understanding of the mechanisms of these processes can lead to the development of more efficient catalysts. These efforts have generally focused on the use of late transition metal complexes with little emphasis placed on early transition metal systems. The reactivity in these systems is potentially quite different and from a fundamental point of view, the scarcity of characterized metal–boron complexes provides an impetus for their synthesis. Prior to the start of this work late transition metal compounds, typically stabilized with phosphine ligands, composed the majority of the known metal–boryl complexes while few early transition metal examples had been isolated.

1

Metal–Boron and Metal–Carbon Bonds

A key difference between boryl and alkyl ligands is the hybridization of B (sp^2) compared to C (sp^3). Thus, appropriate carbon analogs to boryl ligands are carbenes. A similar analogy can be drawn between borylene (M=BR) and alkylidyne (M≡CR) compounds. These isolobal relationships are displayed in Figure 1. Synthetic strategies used to stabilize carbenes may translate to boron compounds due to the isolobal analogy that can be drawn between boron and carbon fragments. One of the most successful strategies has been the use of hetero–atom substitution on the carbene. The homoleptic carbene fragment, CH_2, is a ground state triplet whereas the hetero–atom substituted species C(OR)R are singlets.[9]
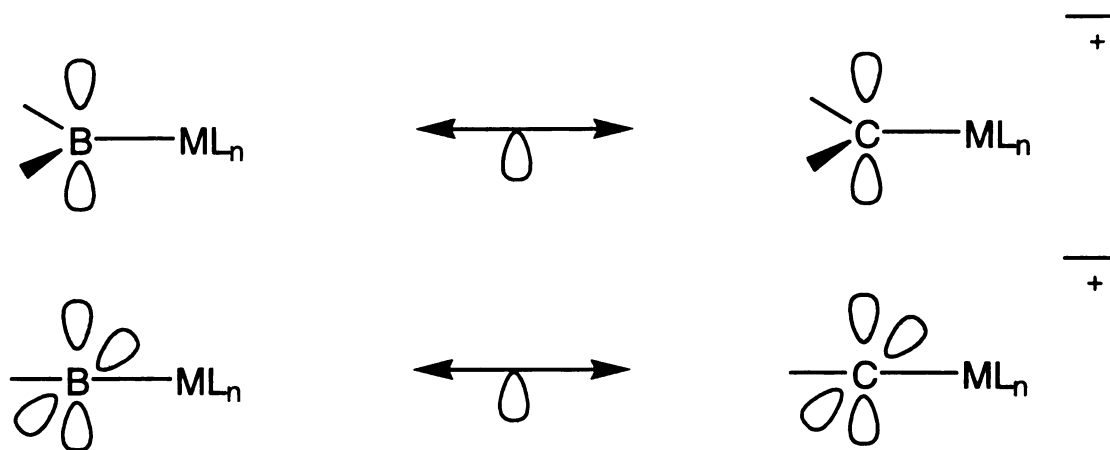
Figure 1. Isolobal relationship between boron and carbon fragments.

In spite of the general analogy that can be drawn between carbon–containing fragments and the related boron–containing fragments, a significant difference between the two atoms that may affect bonding is observed in their electronegativities. The less electronegative boron atom has a value of 2.0 on the Pauling scale while that of carbon is 2.5. The relatively large difference in the electronegativities between the two atoms will likely affect the polarity of M–B bonds relative to M–C bonds. Since boron's electronegativity approaches typical values for transition elements, M–B bonds should be more covalent than M–C bonds.

Hydroamination chemistry with lanthanide metals[10-13] can be loosely compared with hydroboration[14,15] chemistry in regard to the electronegativity of the atoms involved in the bond making and bond breaking processes. The bond between lanthanum and carbon has a dipole situated such that the lanthanum is electropositive and the carbon atom electronegative (Figure 2).[15] Using electronegativity arguments for the metathesis of a lanthanum–carbon bond with an amine, a new lanthanum–nitrogen bond is formed along with an alkane. Similar arguments for the metathesis between a borane and a lanthanum–carbon bond predict the formation of a lanthanum–hydrogen bond and an organoborane.
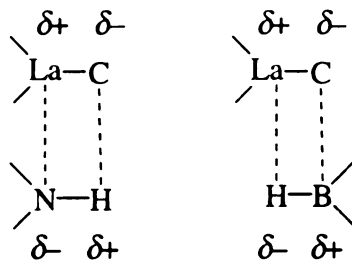
Figure 2. Lanthanum hydroamination and hydroboration comparison.

Synthesis of Metal–Boron Complexes

Several synthetic approaches have utilized the Lewis acidic nature of the borane fragment to generate new coordination compounds. The first successful attempt used triphenyl boron as the Lewis acid reacting with the Lewis basic lithium triphenylgermane (equation 1).[16] Similar compounds were prepared by reacting tin and germanium anions with boron triflouride.[17]

$$(Ph)_3MLi \ + \ (Ph)_3B \longrightarrow Li[(Ph)_3MB(Ph)_3] \quad M = Si, Ge \qquad (1)$$

Nöth and Schmid reported the first transition metal boryl complexes in which the boryl group was bound directly to the metal in 1963 (equation 2). The general approach involved a metathesis of a halo–borane with a metal anion.[18] This reaction induced formation of a metal–boron bond with concomitant loss of salt. The second method used

$$[Me_2N]_2BCl + NaMn(CO)_5 \longrightarrow [Me_2N]_2B-Mn(CO)_5 + NaCl \qquad (2)$$
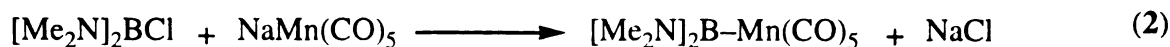
for metal–boron bond formation involves oxidative addition of a borane to the metal. This method was first utilized in 1975 in the reaction between catecholborane (HBCat, Cat $\equiv O_2C_6H_4{}^{2-}$) and Wilkinson's catalyst (ClRh(PPh$_3$)$_3$) forming a rhodium–boron bonded species (equation 3).[19] However, it wasn't until 1980 when interest was rekindled as metal–boryl complexes were postulated as intermediates in catalytic hydroborations of

$$(Ph_3P)_3RhX + HBCat \longrightarrow CatBRhHX(PPh_3)_2 \qquad (3)$$

olefins with catecholborane in rhodium–based systems. A third method for metal–boron bond formation is a σ–bond metathesis pathway. An example of this method of bond formation is pictured in equation 4.[20]

$$Cp_2NbH_3 + HBCat \longrightarrow Cp_2NBH_2(BCat) + H_2 \qquad (4)$$

Extreme care must be exercised in characterizing compounds where M–B bonding is believed to be present. This is highlighted by an early report of the reaction of Cp$_2$WH$_2$ with BF$_3$·OEt$_2$, which led to the formation of an insoluble compound.[21] This compound was originally postulated as containing a tungsten boron bond. However, subsequent reinvestigation of this reaction showed that the product actually formed is a cationic trihydride compound (equation 5).[22,23]

$$\begin{array}{c} Cp \\ \diagdown \\ \diagup W\text{---}\!\!\!^{\backslash\backslash\backslash}H \\ Cp \quad {}^{\blacktriangleright}H \end{array} \xrightarrow{\ BF_3\text{·}OEt_2\ } \left[\begin{array}{c} Cp \\ \diagdown \\ \diagup W\!\!-\!\!H \\ Cp \quad {}^{\blacktriangleright}H \end{array} \right]^{+} \quad BF_4^{-} \qquad (5)$$
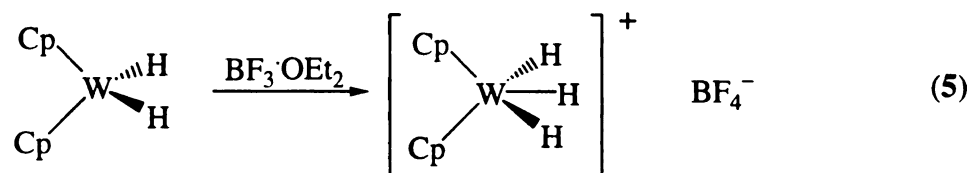
One aspect that hampered early investigations was the scarcity of single crystal X–ray diffraction studies to confirm the actual bonding nature of the boron–containing fragment to the metal center. The first such study examined fac-[IrH$_2$(PMe$_3$)$_3$(BC$_8$H$_{14}$)] in 1990.[24] Following this report, several other groups reported X–ray crystal structures of metal–boryl containing compounds from groups 5–10.[20,25-27]

4

Metal Catalyzed Hydroboration

In 1985, the discovery that Wilkinson's catalyst mediates olefin hydroboration revived metal–boron chemistry. In the absence of a catalyst, catecholborane reacts sluggishly with olefins, even at elevated temperatures. In addition to rate acceleration, metal–catalyzed reactions can alter the regioselectivity of the B–H addition. For example, the C–C double bond of 5–hexen–2–one is hydroborated in the catalytic reaction in stark contrast to the uncatalyzed reaction where the ketone group is hydroborated (Figure 3).[28] Since this initial report, metal–catalyzed hydroboration reactions have been extensively studied.[14,29]
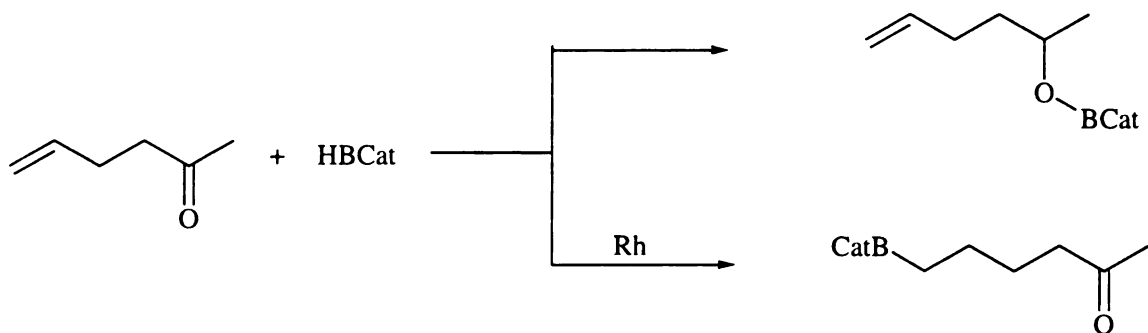
Figure 3. Catalyzed and uncatalyzed reaction of 5–hexen–2–one with catecholborane.

There have been two potential pathways proposed to account for rhodium–based hydroboration catalysis (Figure 4). Hydroboration through the first mechanism occurs with olefin insertion between a metal–hydrogen bond and subsequent loss of alkylborane. Hydroboration via the second mechanism occurs with olefin insertion between a metal–boron bond. Results from theoretical calculations have not clarified the controversy
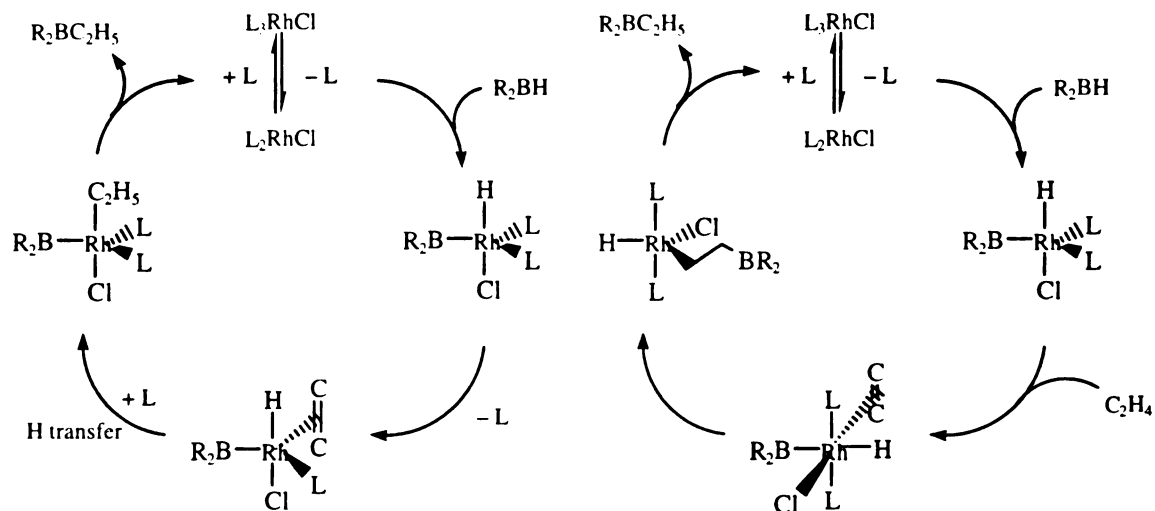
Figure 4. Two possible hydroboration mechanisms.

surrounding the two mechanisms.[30,31] Olefin diboration by $(Ph_3P)_2RhCl(BCat)_2$ provides compelling evidence for olefin insertion into M–B bonds (Figure 5).[32] Although oxidative–addition/reductive–elimination mechanisms are commonly invoked for late transition metal systems, σ–bond metathesis pathways have also been established (Figure 6).[33]
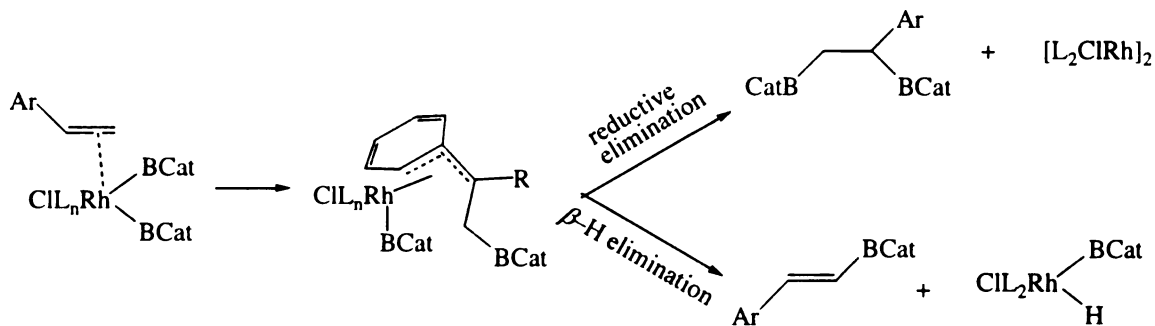
Figure 5. Olefin insertion mechanism.
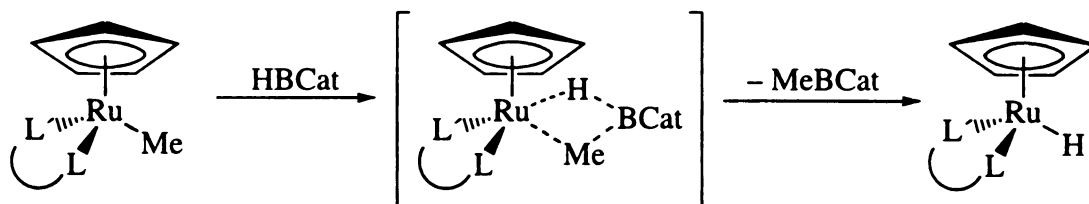
Figure 6. Proposed ruthenium σ–bond metathesis pathway.

Most metal–catalyzed hydroboration studies have centered on the late transition metal systems; however, catalytic hydroboration reactions have been reported for early transition metal systems. Marks has examined the viability of a bispentamethylcyclopentadienyl lanthanum compound, $Cp*_2La(CH(SiMe_3)_2)$, in hydroboration reactions.[15] This compound demonstrated the ability to hydroborate a wide variety of terminal, terminal or internal disubstituted and trisubstituted olefins with high anti–Markovnikov regioselectivity (>98% in all cases) and with minimal substrate hydrogenation. It was not effective, however, for the tetrasubstituted olefin 2,3–dimethyl–2–butene. Labeling studies with DBCat exhibited exclusive incorporation (by NMR) of the deuterium label in the β–C position of the alkylborane. A proposed scheme for lanthanum catalyzed hydroboration is shown in Figure 7.
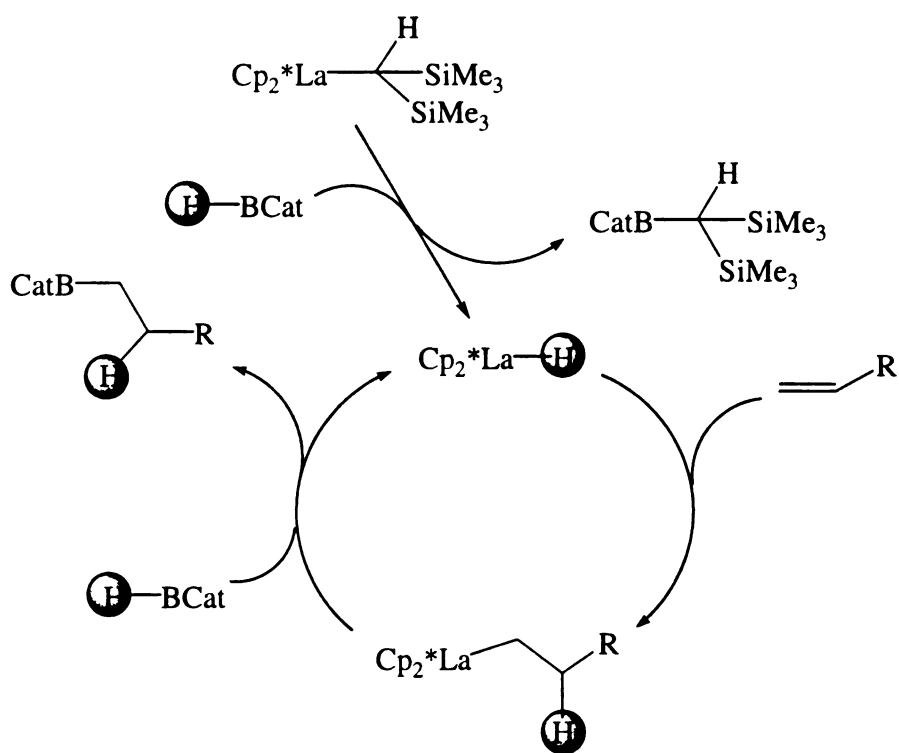
Figure 7. Proposed lanthanum metal–catalyzed hydroboration cycle.

Srebnik has examined the capacity of Schwartz's reagent, $Cp_2Zr(H)(Cl)$, to hydroborate both alkynes and alkenes.[34] In these studies pinacolborane (HBPin, Pin ≡

$O_2C_2(CH_3)_4{}^{2-}$) was used in place of HBCat for the hydroboration reactions with the major benefit being that the products are air and water stable and can be purified by column chromatography, whereas the analogous catecholborane products decompose. The proposed mechanism of alkyne hydroboration by this catalyst is shown in Figure 8. As in the lanthanum system described above, the reaction proceeds via insertion of the olefin between the metal–hydrogen bond.
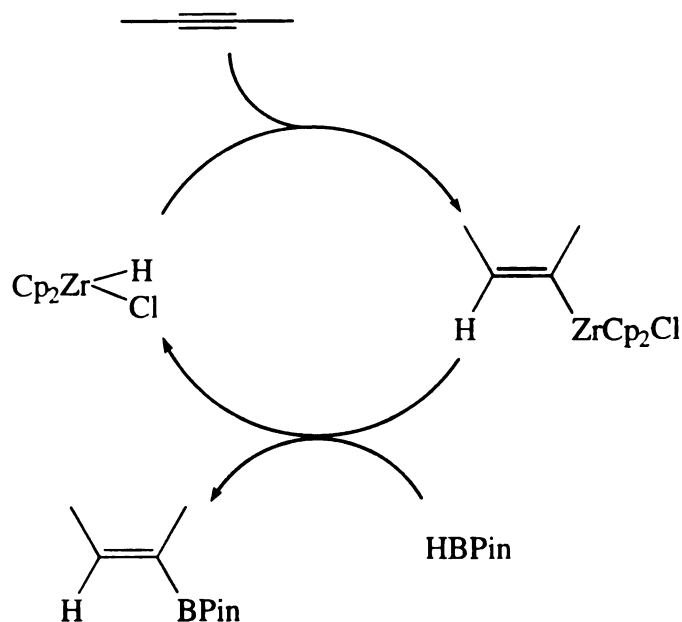
Figure 8. Cp_2Zr based hydroboration of alkynes.

HBCat can disproportionate to form BH_3 and B_2Cat_3, therefore, when HBCat is used as the hydroborating reagent, care must be exercised when determining whether B–C bond formation occurs at the metal center or as a result of "traditional" organic hydroboration.[35] For example, addition of HBCat to cyclohexene catalyzed by $(mes)_2Nb$ (mes = mesityl) does not afford cyclohexylcatecholborane as the major product. Instead, the di and trialkylboranes are the major organoborane products (Figure 9).[36] ^{11}B NMR
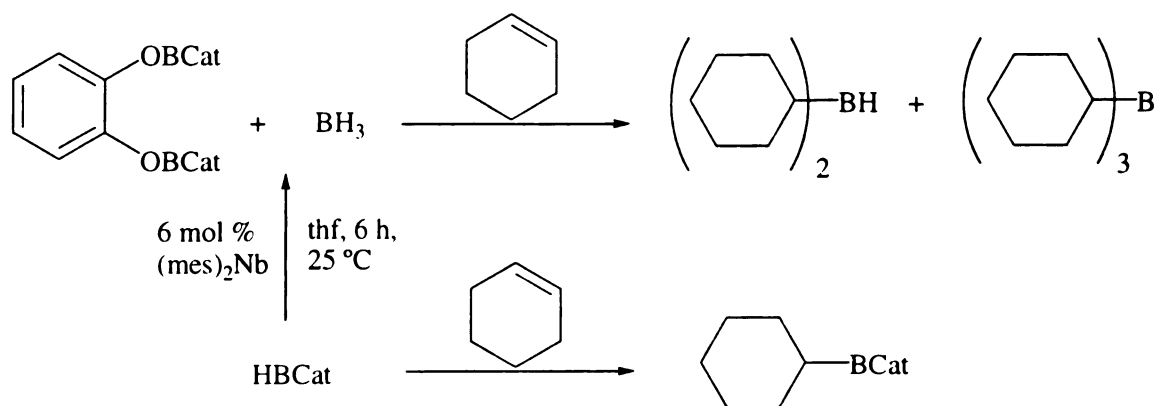
Figure 9. Bis(mesityl)niobium catalyzed "hydroboration."

experiments established that the products did not result from disproportionation of cyclohexylcatecholborane to tricyclohexylborane and B_2Cat_3. Instead, the alkylboranes are hydroboration products of cyclohexene and transient BH_3 generated by metal–catalyzed disproportionation of HBCat. In some early metal systems, catalysis is better behaved and B–C bond formation likely occurs at the metal. Hartwig has shown that conditions must be carefully controlled in order to achieve true metal–catalyzed hydroboration.[37]

Titanocene based systems have also been investigated. Bijpost, et. al., found that most titanocene complexes are inactive or experience rapid catalyst decomposition.[38] In the investigation of the two titanium complexes, $Cp_2Ti(CO)_2$ and Cp_2TiMe_2, Hartwig examined hydroboration of alkynes and alkenes and found near quantitative yields with good to exclusive anti–Markovnikov regioselectivity.[37] A proposed mechanism for titanium catalyzed addition of HBCat to alkenes that proceeds through a ring–opening σ–bond metathetic step is shown in Figure 10.

9
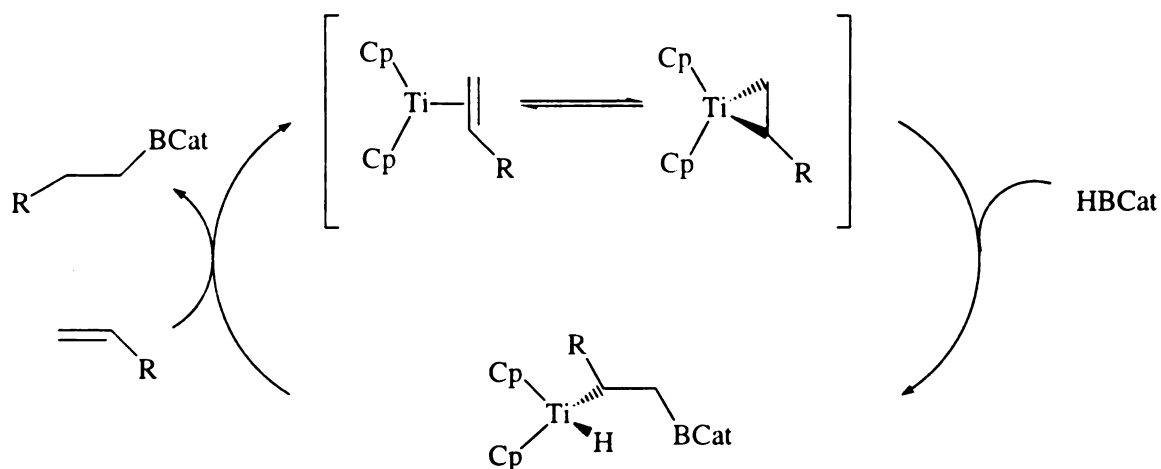
Figure 10. Titanium catalyzed addition of HBCat to alkenes.

The deactivated form of the catalyst was isolated and subjected to single crystal X–ray diffraction studies. Depending on the amount of catalyst loading during the hydroboration reaction, two forms of deactivated catalyst could be isolated. Under 'high' catalyst loading environments, a borohydride type complex can be isolated (Figure 11).[37] The second form of the deactivated catalyst can be isolated under a more 'typical'
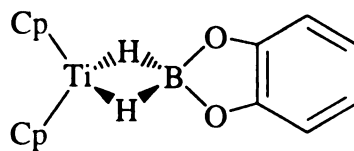
Figure 11. Deactivated catalyst resulting from 'high' catalyst loadings.

catalyst loading. A single crystal X–ray diffraction study of this compound indicated a titanium(III) borate structure (Figure 12).[37] The two deactivated forms of the catalyst were tested for their viability of hydroborating olefins. Each was able to catalyze the transformation; however, the rate of the reaction was considerably slower than for the original complex.

10
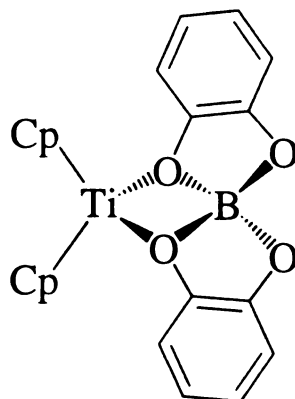
Figure 12. Deactivated catalyst resulting from 'typical' catalyst loadings.

Dehydrogenative boration of alkenes can also proceed through a ring–opening σ–bond metathesis pathway with use of a different titanium catalyst, $Cp*_2Ti(\eta^2\text{-}CH_2=CH_2)$. Reaction of excess ethylene with various boranes led to formation of vinyl borane products and ethane with regeneration of the original olefin complex.[39-41] Figure 13 depicts the mechanism for this catalytic transformation.

$Cp*$

Ti—CH_2

CH_2

$Cp*$

$HBE_2C_6H_4$

$Cp*$

Ti—

$Cp*$ $BE_2C_6H_4$

$Cp*$

Ti—$BE_2C_6H_4$

$Cp*$ H

$E = O, NH$

C_2H_6
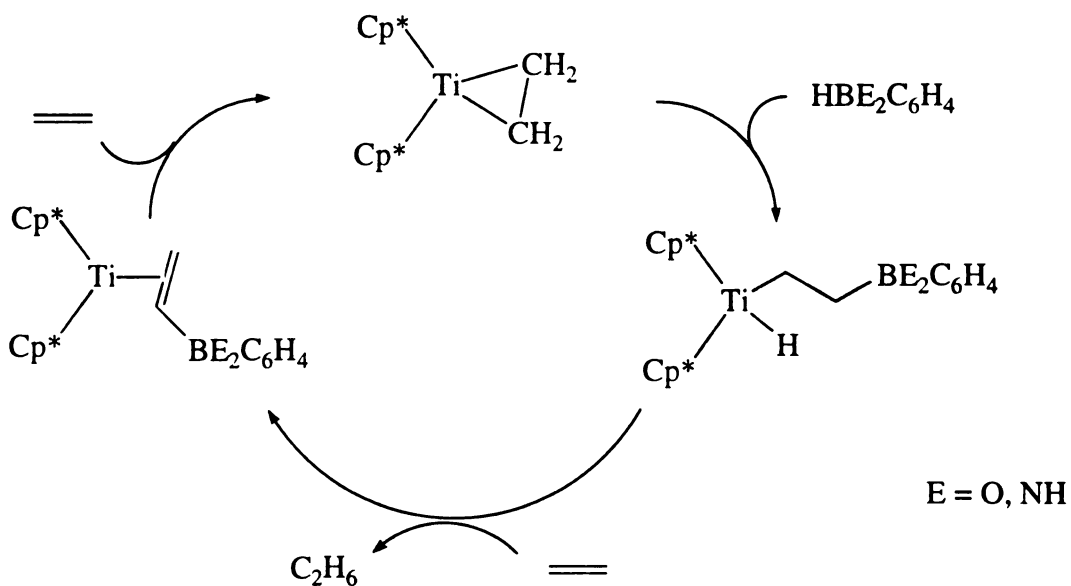
Figure 13. Catalytic dehydrogenative boration with $Cp*_2Ti(\eta^2\text{-}CH_2=CH_2)$.

CHAPTER 2

SYNTHESIS

Reaction of $Cp_2TaH_2^-$ with chlorocatecholborane

Cp_2TaH_3 can be deprotonated with n–BuLi to form a bright yellow–orange solid, $\{Cp_2TaH_2Li\}_x$,[42] which has been shown to be a reactive source of $Cp_2TaH_2^-$. In a reaction comparable to the addition of chlorocatecholborane to Cp_2WH^-,[20] one equivalent of chlorocatecholborane, dissolved in toluene, was added to a $Cp_2TaH_2^-$ slurry in toluene at -78 °C. Upon warming to room temperature, the suspension gradually lightened in color from bright yellow–orange to pale yellow with formation of an off–white precipitate. The reaction mixture was filtered, and a nearly colorless microcrystalline precipitate was collected after solvent removal. ^1H and ^{11}B NMR spectra of the crude solid strongly indicated that two products were formed. The ^1H NMR spectrum displayed two major cyclopentadienyl resonances, two pairs of catecholate regions as well as several upfield hydride signals. The ^{11}B NMR spectrum also exhibited two resonances, δ 65 and δ 70. Through fractional crystallization in toluene at -78 °C, two products, exo and $endo$–$Cp_2TaH_2(BCat)$[43] (exo and $endo$–$\mathbf{1}$) could be separated from the crude reaction mixture. Formation of regioisomeric products for group 5 metallocene products is rare, but precedent for formation of endo and exo isomers exists as the addition of silanes to Cp_2TaH_3 gives a mixture of endo and exo isomers observed by ^1H NMR spectroscopy.[44]

12
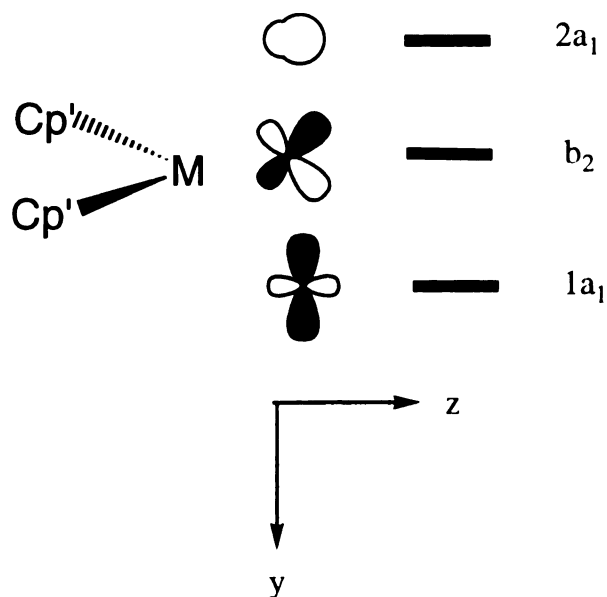
Figure 14. Frontier molecular orbitals of the bent metallocene fragment.

Regioselective reactivity has been observed in zirconium metallocene chemistry. CO adds preferentially to the central lobe of the $1a_1$ LUMO[45] (Figure 14) of $Cp*_2ZrH_2$ to generate a product with chemically equivalent hydride ligands.[46] In the analogous reaction between CO and Cp_2ZrMe_2,[47] the kinetic product is an exo acyl isomer, which argues strongly for initial attack of the carbon monoxide molecule to the exo lobe of the $1a_1$ orbital (Figure 15). Formation of the boryl complexes can be viewed in terms of nucleophilic addition of the Ta anion to the boron electrophile. Since the filled Ta $1a_1$ orbital has electron density distributed along the y and z axis (Figure 14), attack at distinct lobes can give either endo or exo products. (Figure 16).[41]
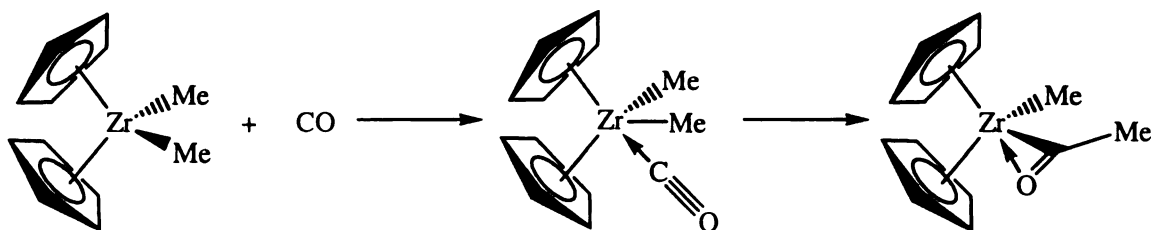
Figure 15. Reaction of Cp_2ZrMe_2 with CO.

13
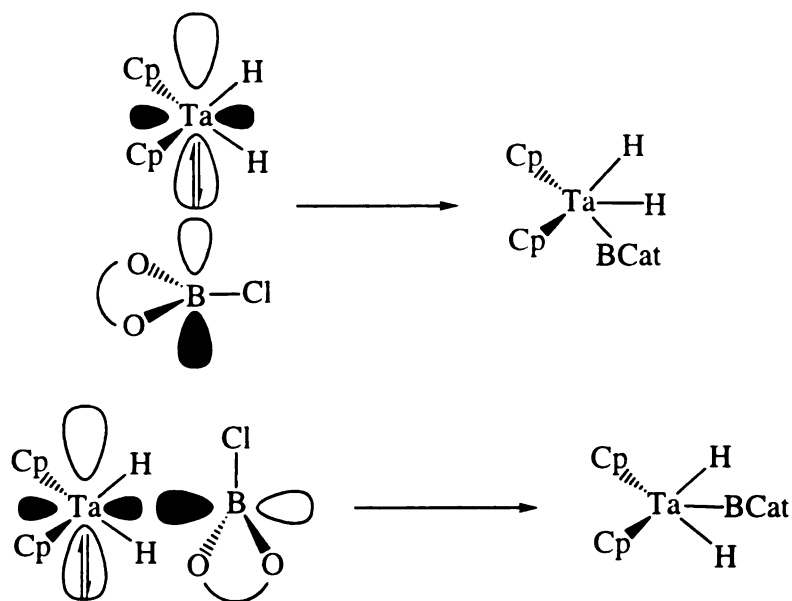
Figure 16. LUMO of metallocene fragment oriented with chlorocatecholborane to form an exo isomer (top) and an endo isomer (bottom).

For the less soluble isomer, the hydride ligands resonated as a singlet at δ –4.24, which integrated as two protons versus the cyclopentadienyl resonance. Assuming that both the hydrides and the boron ligand are attached to tantalum, the chemical equivalence of the hydrides requires that the hydrogen atoms bind to the metal in flanking positions (or exo positions) of the metallocene wedge. This relegates the boryl ligand to the central position (or endo position) of the metallocene wedge.

The high field region of the more soluble isomer exhibited two resonances that each integrated as one proton with respect to the cyclopentadienyl resonance with a doublet at δ –4.20 ($|J_{HH}|$ = 5.6 Hz) and a very broad "singlet" at δ –5.15. Selective decoupling of the resonance at –5.15 ppm resulted in the collapse of the doublet at –4.20 ppm indicating that the two hydrides are coupled to each other. The chemically inequivalent hydrides should ideally appear as two doublets; however, the broad nature of the hydride resonance at –5.15 ppm can be attributed to coupling to the quadrapolar ^{11}B and ^{10}B nuclei. The $^{1}H\{^{11}B\}$ NMR spectrum (Figure 17) exhibited a well–resolved

doublet at −5.15 ppm, which clearly shows that boron coupling is responsible for the observed line broadening. The only model consistent with the above NMR data requires that hydride ligands occupy exo and endo positions and the boryl fragment occupies the other exo position in the metallocene wedge.
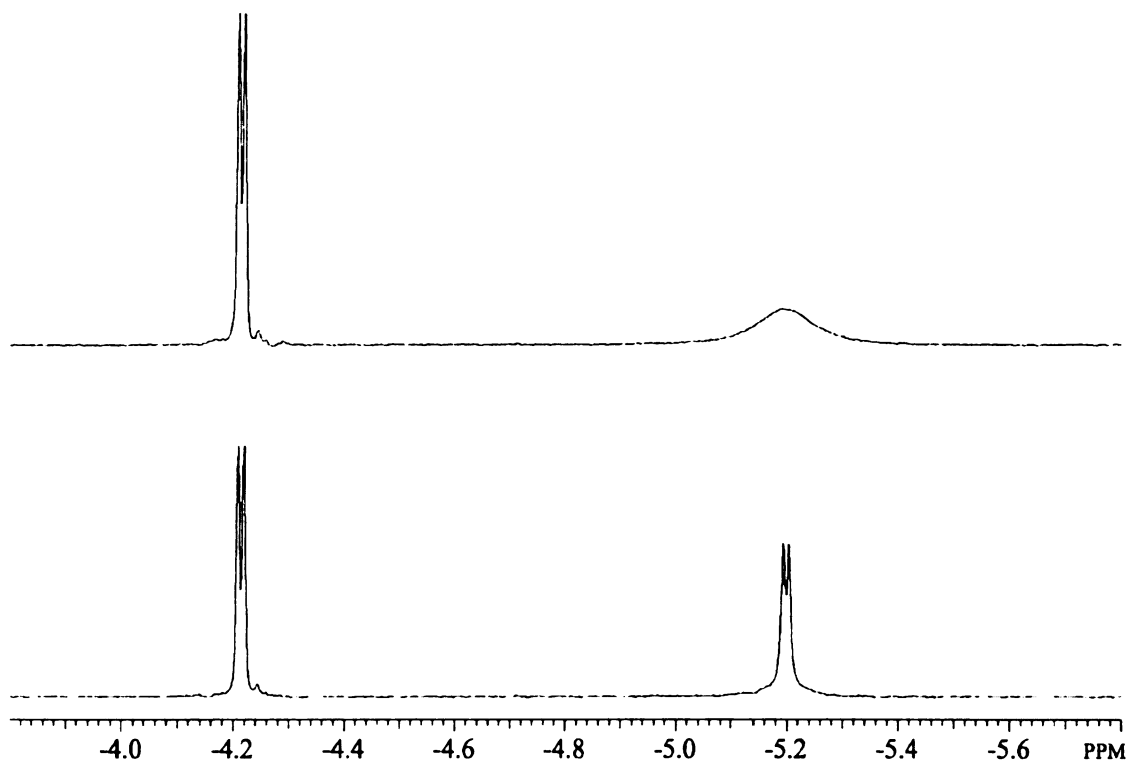
Figure 17. ^1H (top) and $^1H\{^{11}B\}$ (bottom) NMR spectra of *exo*–1 in C_6D_6 (500 MHz, 22 °C).

The two isomers were also crystallographically characterized, and the proposed binding modes for the boryl fragments in each isomer was confirmed. In spite of bonding to heavy tantalum nuclei, the hydride positions were located in difference Fourier maps.

Locating hydrogen atom position proximal to heavy atoms (metals) is inherently complicated. Ghost peaks, resulting from the thermal motion of heavier atoms, can arise in positions that are structurally reasonable for hydride ligands. This situation is exacerbated by including high angle data since the decrease in scattering factor with

15

increasing θ is most pronounced for hydrogen as compared to heavier elements.[48] Should the peak in question be an artifact of a nearby heavy atom, the peak will often vanish at lower thresholds of (sin θ)/λ (Figure 18). The way to circumvent this problem is to use
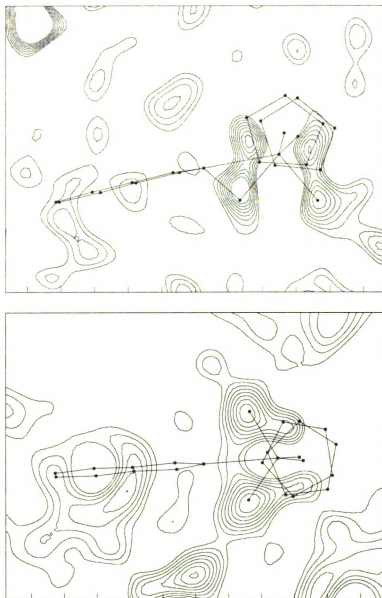
Figure 18. Electron contour mapping diagram for *exo*–**1** (top) and *endo*–**1** (bottom). Data with $2\theta < 30°$ were used.

low angle data where contributions from hydrogen are enhanced. Refinement of the lower angle data resulted in hydride peaks that were, within experimental error, identical

to the refined hydride positions. Thus, the hydride positions in Figure 18 almost certainly represent "true" positions, despite the fact that the esd's for their positions are moderately large.

The two areas of unaccounted electron density in each contour diagram can be ruled out as reasonable hydride locations for two reasons. The first is the short Ta–H bond length required as a result of hydrogen occupation in those positions. The second reason deals with the actual position of the regions of electron density: each unaccounted region of electron density is located on the bent metallocene "side" of the wedge.

The solid state structure of the endo isomer (Figure 19) adopts a configuration in which the plane defined by the O(1)–B–O(2) atoms and the plane defined by the Cp centroids and Ta are coplanar when viewed down the Ta–B vector. At first glance, there are two possible valence bond descriptions that fit the crystallographic data: (i) a Ta^{III}–borohydride complex with bridging hydrides between Ta and B nuclei, or (ii) a Ta^{V}–dihydrido boryl complex. The formal bonding scheme of this isomer can be determined by examining certain aspects of the structure: the tantalum–boron distance, the boron–hydrogen distances and the H–Ta–H angle. The Ta–B distance of 2.263(6) Å is shorter than the Nb–B distance of 2.411(5) Å in $Cp_2Nb(H_2BC_8H_{14})$, which adopts a borohydride structure.[20] Due to the lanthanide contraction, tantalum and niobium atoms and ions are nearly identical in size, and thus any differences in bond lengths can be directly compared. Also, the B···H distances (1.75(5) Å and 2.11(6) Å) are substantially longer than those typically found in borohydride complexes (B–H = 1.10–1.20 Å) and significantly longer than B···H distances in the related niobium compound *endo–* $Cp_2NbH_2(BCat)$ (**2**) (1.69(4) Å and 1.62(5) Å), which has been described as a d^0 dihydride boryl compound.[20] Lastly, the H–Ta–H angle of the endo isomer (113(3)°) is closer to H_{exo}–Ta–H_{exo} bond angle found in Cp_2TaH_3 (125.8(5)°) than the corresponding angles found in $Cp_2Nb(H_2BC_8H_{14})$ (70(3)°) and **2** (92(2)°).[20] Thus, the crystallographic

data favor that of a Ta^V–boryl complex. This bonding description is further corroborated by spectroscopic data and chemical behavior of *endo*–1.
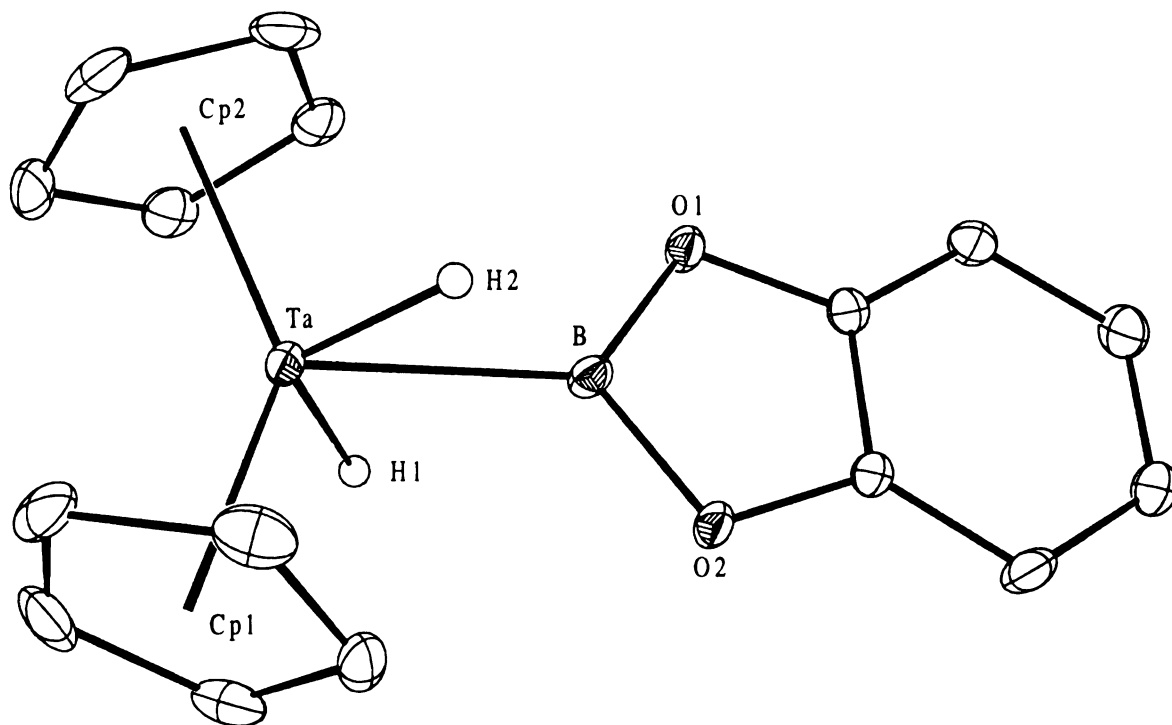
Figure 19. ORTEP diagram of *endo*–1. Ellipsoids represent 25% probability for electron density.

The exo isomer (Figure 20) adopts a configuration similar in which the plane defined by the O(1)–B–O(2) atoms is perpendicular to the plane defined by the H(1), H(2), B and Ta atoms. Fourier maps using data from $2\theta < 30°$ reveal two peaks at chemically reasonable positions for the exo (H(1)) and endo (H(2)) hydride atoms. Again, two structures can be considered. The first is an authentic Ta^V–dihydrido boryl compound, and the second is a Ta^{III} agostic borane complex. Although the esd's are larger for the exo structure, the chemical position of H(1) seems reasonable when comparing the H(1)–Ta–B angle (120(4)°) and the Ta–H(1) distance of 1.76(12) Å to the neutron data for Cp_2TaH_3 (H_{exo}–Ta–H_{exo} = 125.8(5)°, Ta–H_{exo} = 1.769(8) and 1.777(9) Å).[49]
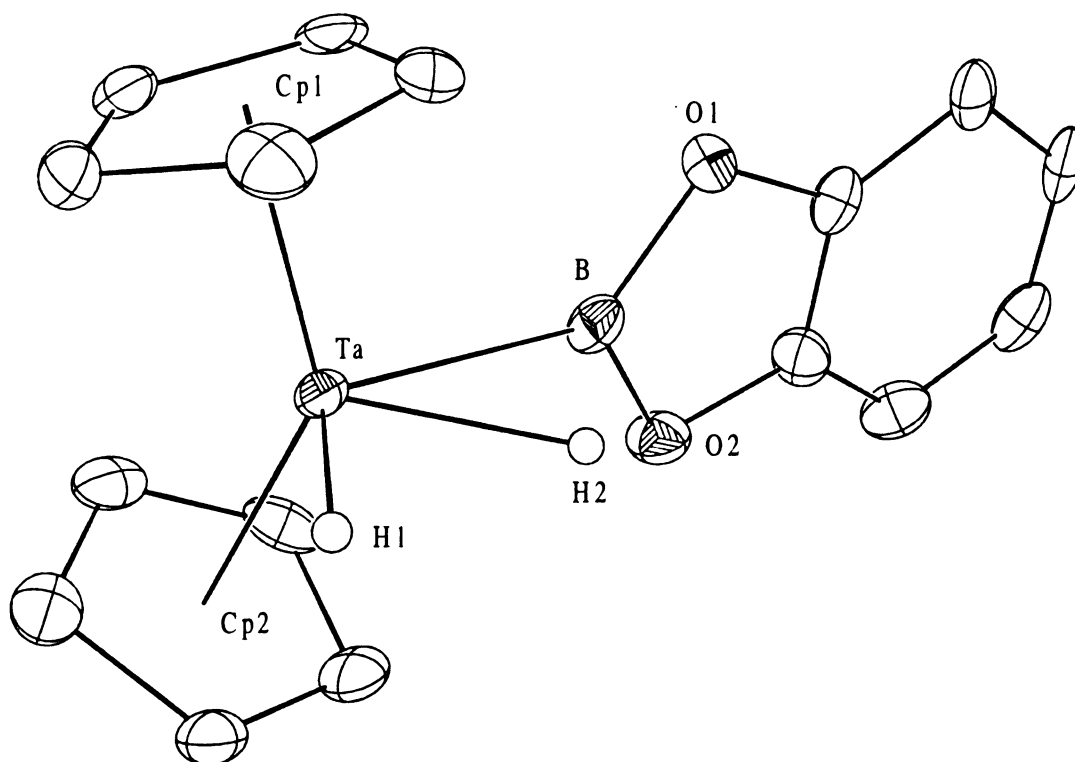
Figure 20. ORTEP diagram of *exo*–1. Ellipsoids represent 25% probability of electron density.

The position of H(2) can be viewed as unusual both with regard to its position in the metallocene wedge and to the boryl ligand. The H(1)–Ta–H(2) and H(2)–Ta–B angles, 81(6)° and 39(3)°, respectively, and the relatively short B–H(2) distance (1.45(10) Å) indicates unsymmetric coordination of H(2). The Ta–B distance of 2.30(1) Å is only slightly longer than the endo compound discussed above. Although the sum of the angles about the boron atom is 360.0(22)°, it has been demonstrated that this value is not significantly affected by hydrogen interactions.[50] The B–H coupling, and other spectroscopic data, also support the interaction between H(2) and B. Based on spectroscopic differences between *exo*–1 and a congeneric Nb borane adduct (see below), *exo*–1 is best described as a Ta^V complex where the boron atom interacts with the adjacent hydride ligand.

Factors leading to the observed orientation of the boryl fragment in the solid state structures are not obvious. If all electronic contributions are ignored, steric based calculations (SPARTAN) predict that the preferred geometry of *endo*–1 would not be the observed eclipsed geometry present in the solid state structure. However, the barriers for rotation about the Ta–B bond appear to be small so the observed eclipsed geometry can be accessed fairly easily. The observed boryl geometry of the two isomers could be explained by interactions between boron and the hydrogen ligands essentially "locking" the boryl ligand in place. In both cases, filled metal–hydride bonding orbitals with the proper symmetry could back–bond to the *p* orbital of boron, forcing a geometry where the boryl oxygen atoms are eclipsed with the cyclopentadienyl ligands. However, this explanation appears to be of minor importance for the endo isomer as there is no evidence of interaction between the hydride ligands and the boron atom of *endo*–1.

To determine whether a rigid, eclipsed structure is maintained in solution, the C_2 symmetry about the Ta–B bond must be broken. With this intent, analogs were synthesized utilizing β–chloro–5–methyl catecholborane. Broadening of the cyclopentadienyl resonances was observed upon cooling; however, the low temperature limit for rotation was not observed. Even though the slow exchange limit was not reached, some rotational information about the Ta–B bond can be deduced. Examination of the ^{1}H NMR spectra revealed the cyclopentadienyl resonances of *exo*–1 broadened to a greater degree than the corresponding resonances of the endo isomer, denoting a higher temperature for coalescence of the exo isomer relative to the endo isomer. This observation can be rationalized by considering the interaction of boron with the hydride ligands. Based on bond lengths, a greater interaction of the endo H with the boron atom (1.45(10) Å) would be expected in *exo*–1 than for either of the two hydride ligands with the boron atom in *endo*–1 (1.75(5) Å and 2.11(6) Å). The higher coalescence temperature for the exo isomer is consistent with a larger rotational barrier resulting from a higher degree of B–H interaction for *exo*–1 compared to *endo*–1.

Isotopic Perturbation of Equilibria

Isotopic perturbation of equilibrium resulting from deuterium substitution has been extensively applied in NMR studies of equilibria involving hydrogen transfer.[51-53] For two rapidly equilibrating species, isotopic substitution shifts the equilibrium as a result of the difference between H and D zero–point energies.[54] Since the observed chemical shift is the average of limiting shifts for the equilibrating structures, perturbation in equilibrium results in variations of observed chemical shifts for different isotopomers. It is crucial to recognize that large chemical shift differences have been attributed exclusively to intrinsic isotope effects.[55] Thus, a large chemical shift difference is not rigorously diagnostic for structural equilibration. If the chemical shift of a resonance in question is temperature independent, exclusive contributions from intrinsic isotope effects could account for the observed shift. Hence, temperature dependent chemical shifts provide stronger evidence for equilibrium origins when large isotopic shifts are observed.

There are two other possible explanations producing temperature dependent NMR resonance shifts.[56] The first possibility is chemical exchange between atoms in magnetically different environments. In this scenario, a barrier to rotation that equates the chemical environments must be overcome to produce magnetically equivalent environments on the NMR time scale. In the fast exchange limit, the resulting chemical shift will be the average of the two limiting chemical shifts (when the two chemically distinct sites are equally populated) or a weighted average of the two limiting chemical shifts when the two chemically distinct sites are unequally populated.

The second possible explanation is the interaction of a molecule with a paramagnetic impurity in the sample. Temperature dependence can be explained by the degree of interaction of the molecule with any unpaired electron(s) found in the paramagnetic impurity. The large magnetic moment of an unpaired electron ($-1836 \times$ the

nuclear magneton for an electron with g = 2.00)[57] can alter the localized magnetic field thereby inducing a shift in the resonance.

The isotopic perturbation of equilibrium that results from deuterium substitution has been applied by Hartwig and coworkers to probe B–H interactions in $2-d_{0-2}$.[20] Equilibrium between boryl and borohydride structures was invoked to account for consecutive upfield shifts of hydride and deuteride resonances upon deuterium substitution. Temperature dependence for the chemical shift perturbation was not demonstrated in this study. Thus, chemical shift differences arising from intrinsic isotope effects cannot be excluded. A related example involving equilibrium between $Ir(H_2)H/IrH_3$ species has been recently reported by Heinekey and co–workers.[58] In this study, the evidence for chemical shift differences arising from isotopic perturbation of equilibrium is more convincing. In addition to the temperature dependent shifts for the H_3, H_2D, and HD_2 isotopomers, temperature dependent J_{H-D} values for tritiated compounds correlate with equilibrium constants extracted from the chemical shift data.

For group 5 metallocene complexes with H and BCat ligands in the coordination sphere, large chemical shift differences from isotopic substitutions arise when B–H interactions are inferred from X–ray crystal structures.[20,59,60] Spectroscopic data for structurally characterized compounds show no obvious correlation between binding mode (boryl–hydride vs. borane adduct) and magnitude or direction of the isotopic shift, which limits interpretations based on isotopic probes. Although it is not clear whether the observed shifts arise from perturbation of equilibrium or intrinsic isotope effects in group 5 metallocene complexes, isotopic labeling experiments provide data that can be directly compared to spectroscopic data of closely related compounds which have been structurally characterized.

Deuterium isotopomers were synthesized for both *exo*–1 and *endo*–1. Figure 21 displays the hydride region of the ^1H NMR spectrum. A significant perturbation of the

resonance noted for the endo hydride of *exo*–1 and with little perturbation of the resonances for the other hydride ligands of the two isomers.
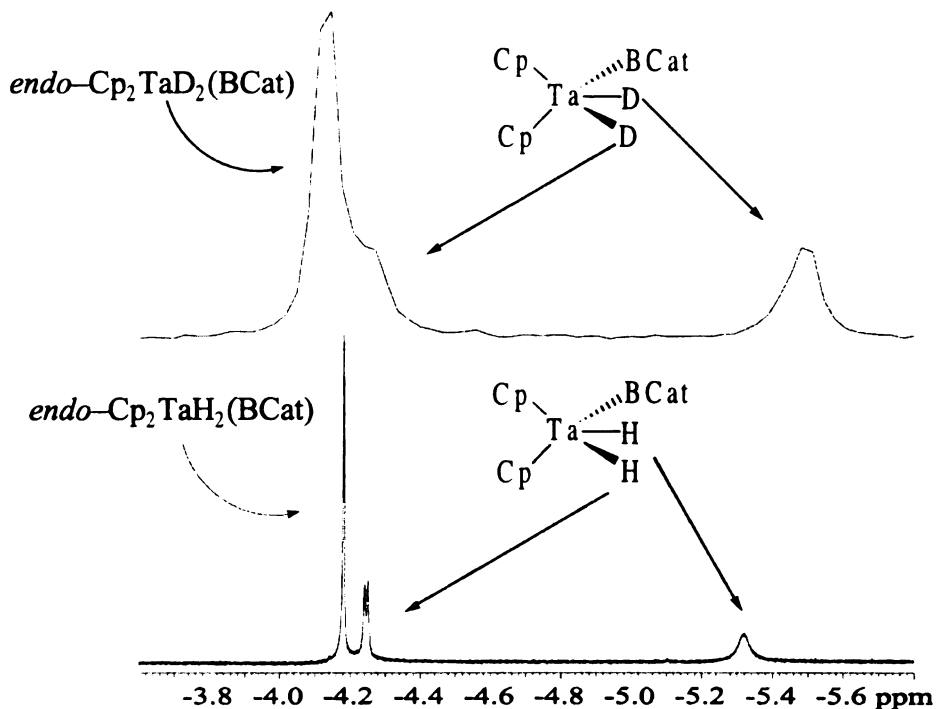
Figure 21. ^{2}H spectrum (top, 46 MHz, toluene, –40 °C) and ^{1}H spectrum (bottom, 500 MHz, tol–d_8, –40 °C) of the hydride region of *exo* and *endo*–1–$d_{0.2}$.

The temperature dependence on the chemical shift for the hydride ligands of *exo*–1 and *endo*–1, was investigated over a broad temperature range. The ^{1}H NMR data for the hydride ligands of *exo*–1 and *endo*–1 is found in Table 1 and Table 2, respectively. Significantly, the chemical shift for the highest field resonance (the endo hydride ligand of *exo*–1) was nearly temperature independent (Figure 22). The resonances of the exo hydride of *exo*–1 and the hydrides of *endo*–1 demonstrated a large temperature dependence (Figure 23). The only resonance that exhibited a larger isotopic perturbation of the chemical shift is also the only resonance that exhibited very little temperature dependence.
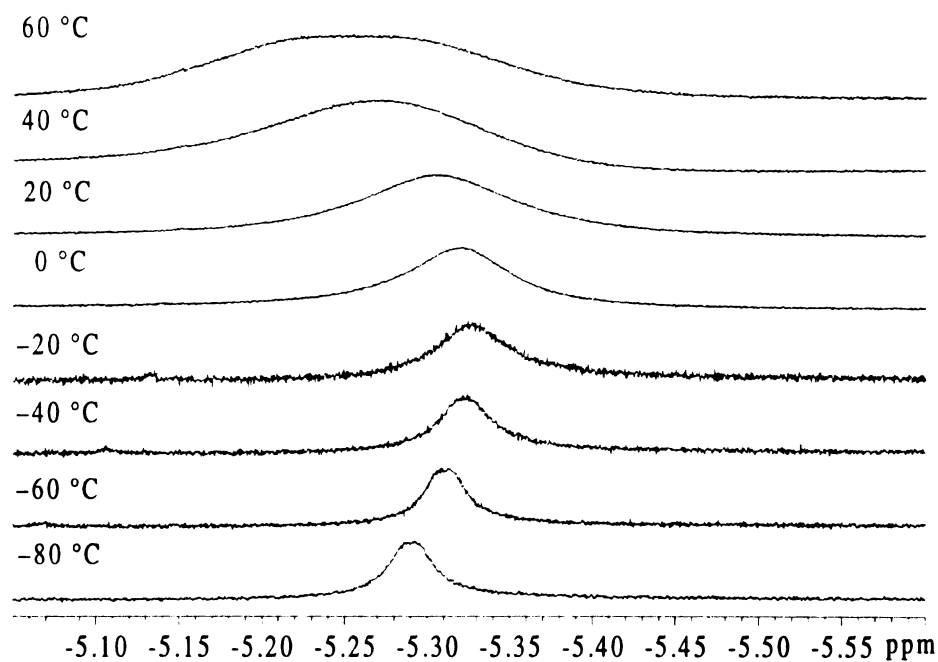
Figure 22. ^{1}H NMR spectra for the endo hydrogen ligand of *exo*–1 (toluene–d_8, 500 MHz).
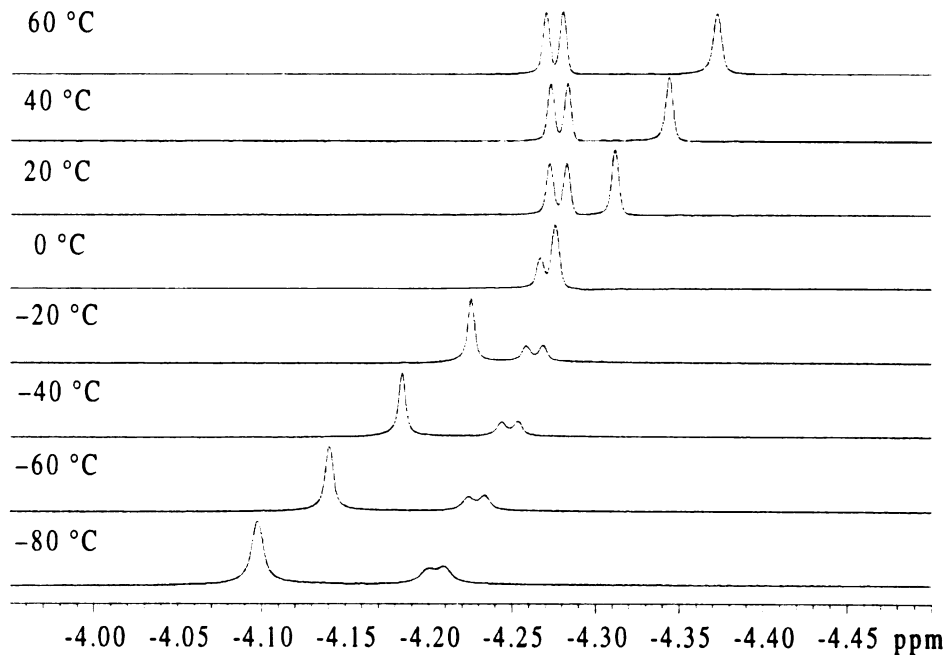
Figure 23. ^{1}H NMR spectra for the hydride ligands of *endo*–1 (initially downfield) and the exo hydrogen ligand of *exo*–1 (initially upfield) taken in toluene–d_8 (500 MHz).

Temperature dependence for the coupling constant for the exo hydride of *exo–*1 was investigated over the same temperature range. There was a –18.2% change in the coupling constant, from the highest coupling constant value to the lowest value, over the investigated 140 °C temperature range, but only a –8.0% change from the two temperature extremes. A coupling constant change of 8.0% over 65 °C was observed for [TpIr(PMe$_3$)(H$_2$)H]BF$_4$–d_2 and a coupling constant change of –1.1% over the same temperature range for [TpIr(PMe$_3$)(H$_2$)H]BF$_4$–d_1 by Heinekey.[58,61] These two experiments, taken together, suggest that the observed perturbation and temperature dependencies result from intrinsic isotope effects rather than a perturbation of equilibria between limiting structures.

Table 1. ^{1}H NMR data for the hydride ligands of *exo–*1 in toluene–d_8.

Hydride position	Temperature (°C)	Chemical shift (ppm)	Coupling constant (Hz)
Exo	60	–4.28	5.50
	40	–4.28	5.50
	20	–4.28	5.00
	0	–4.27	4.50
	–20	–4.26	5.06
	–40	–4.25	4.96
	–60	–4.23	4.90
	–80	–4.20	4.88
Endo	60	–5.28	
	40	–5.29	
	20	–5.31	
	0	–5.32	
	–20	–5.33	
	–40	–5.32	
	–60	–5.31	
	–80	–5.29	
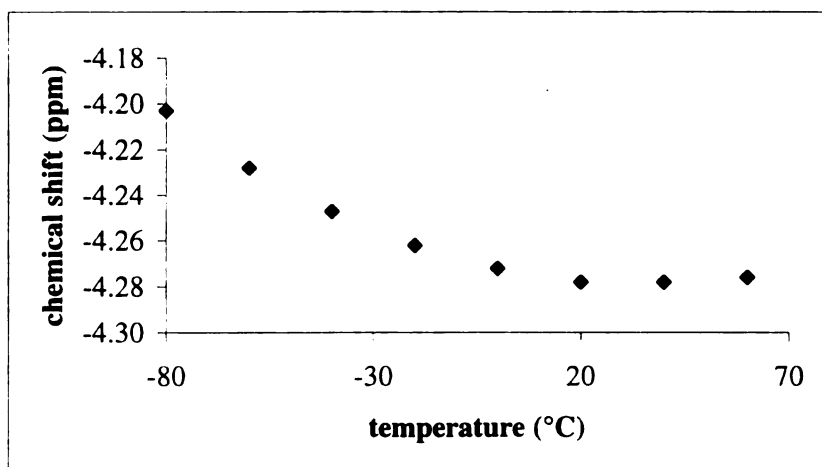
Figure 24. Chemical shift temperature dependence for the exo hydride of *exo*–**1**.
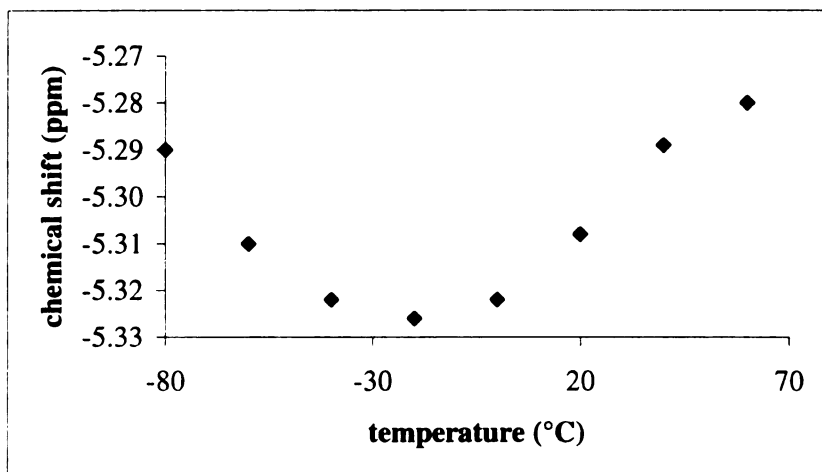
Figure 25. Chemical shift temperature dependence for the endo hydride of *exo*–**1**.
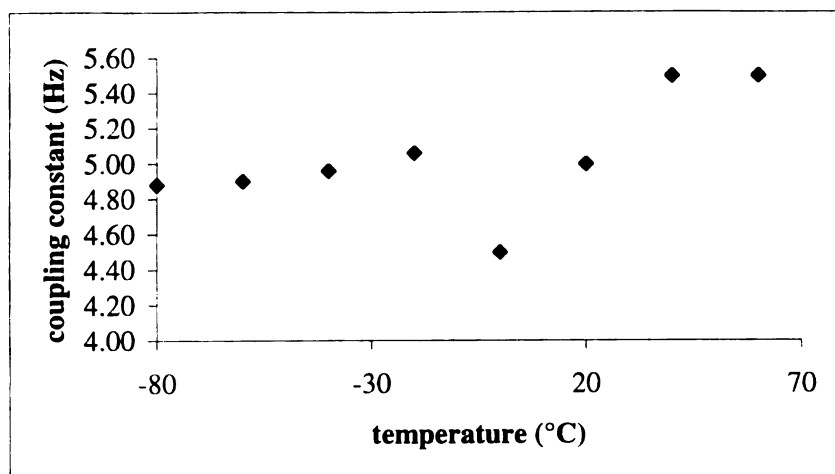
Figure 26. Coupling constant temperature dependence for the hydride ligands of *exo–1*.

Table 2. ^1H NMR data for the hydride ligands of *endo–1* in toluene–d_8.

Temperature (°C)	Chemical shift (ppm)
60	–4.37
40	–4.34
20	–4.31
0	–4.28
–20	–4.22
–40	–4.18
–60	–4.14
–80	–4.10
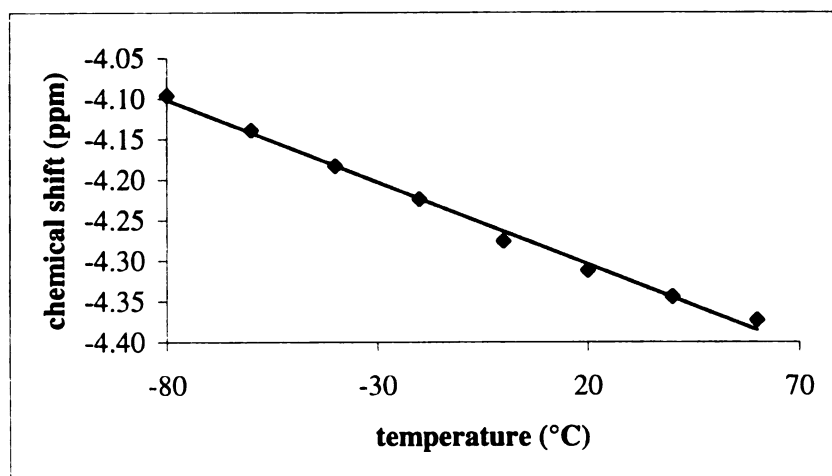
Figure 27. Chemical shift temperature dependence for the hydride chemical shift of *endo–1*.

The temperature dependence of the chemical shift and the coupling constants for [TpIr(PMe₃)(H₂)H]BF₄–d_2 and [TpIr(PMe₃)(H₂)H]BF₄–d_1 were successfully fit to a model consisting of two equilibrating species in solution.[58] The data for the temperature dependent nature of the hydride resonance of endo–1 can be successfully modeled as two rapidly equilibrating species in solution, a Ta^V dihydridoboryl (Cp₂TaH₂(BCat), A) and a Ta^{III} borohydride complex (Cp₂Ta(H₂BCat), B) in the low temperature extreme. While the model (see Appendix A for complete derivation of the model) does successfully explain the temperature dependence of the hydride chemical shift, the limiting hydride resonance for the borohydride structure (Table 3) is not typical for this type of complex and is therefore not considered to be an accurate representation for this compound in solution.[62] An isotopic perturbation of equilibria explanation does not appear likely for the observed temperature dependence for exo and endo–1. Intrinsic isotope effects can also be used to explain the observed temperature dependent nature of the chemical shift. Contributions to the temperature dependence of the chemical shielding (and therefore the chemical shift) arise from anharmonic vibrations and rotational distortions have been shown to be prevalent in gaseous systems.[63,64] Other possible explanations are conceivable but do not appear to be likely.[65]

Table 3. Modeling results for endo–1.

Temp. (°C)	exp. (H₂, δ)	A (H₂, δ)	B (H₂, δ)	calc. (H₂, δ)	% A	% B
–20	–4.22	–4.19	–4.24	–4.22	44	56
–40	–4.18	–4.15	–4.20	–4.18	44	56
–60	–4.14	–4.12	–4.16	–4.14	43	57
–80	–4.10	–4.08	–4.11	–4.10	42	58

Cp*₂NbH(olefin) Chemistry

Our inability to cleanly synthesize metal anions of pentamethylcyclopentadienyl (Cp*) analogs required an alternate synthesis for the Cp* derivatives. In broad terms, the chemistry of molecules containing the Cp* ligand is similar to those containing a Cp

ligand, but there are some important differences that can potentially make the reactivity of Cp and Cp* compounds distinct. First, the Cp* ligand is bulkier than the Cp ligand which can affect the sterics of the coordination sphere. Secondly, the electron donating ability of Cp* is greater than that of the Cp ligand thereby altering the electronic structure of the metal.[66] For these reasons, we developed synthetic routes to Cp*$_2$MH$_2$BX$_2$ compounds from Cp*$_2$MH(olefin) and borane reagents.

Cp*$_2$NbH(η^2–CH$_2$=CH(Me)) (3) and two molar equivalents of HBCat´ (HBO$_2$C$_6$H$_3$–4–^{t}Bu) react to give Cp*$_2$NbH$_2$BCat´ (4) and the alkylboronate ester, ^{n}PrBCat´. Compound 4 could be crystallized from cold pentane solutions giving analytically pure material. The compound was formulated as the endo form based on a single upfield hydride resonance that was observed in the ^{1}H NMR spectrum (–8.19 ppm $\Delta v_{1/2}$ = 64 Hz in C$_6$D$_6$) which integrated as two protons versus the methyl protons of the Cp* ring.

Analysis of the ^{1}H NMR spectrum of the isolated compound is straightforward. A sharp singlet at 1.85 ppm and was assigned to be the Cp* methyl protons. Another sharp singlet at 1.30 ppm integrated as nine protons versus the Cp* methyl protons and was attributed to the *tert*–butyl methyl protons of the catecholate ring. Three resonances in the aromatic region each integrated as one proton versus the Cp* methyl protons corresponding to the hydrogen atoms of the catecholate ring. A single peak was also found in the ^{11}B NMR located at 60 ppm with $\Delta v_{1/2}$ = 300 Hz.

Some potential mechanisms that could account for the observed products from the reaction of 3 with HBCat´ are shown in Figure 28. Pathway A incorporates reactivity through a propyl intermediate, (5). In this route, HBCat´ oxidatively adds to 5 generating 6. Reductive elimination of the organoborane from 6 generates a monohydride intermediate, (7), which is common to all three mechanisms. The metal–borane adduct, 4, forms when 7 is trapped with HBCat´. Alternatively, σ–bond metathesis between 5 and HBCat´ could generate 7 directly, circumventing 6 entirely. Pathway B invokes ring–

opening of the metallacyclopropane ring similar to that proposed in reactions of Ti olefin complexes.[37,39,40] Reductive elimination of [n]PrBCat from **8** generates **7**. In pathway C, metathesis between metal–hydride and B–H bonds generates **9** with loss of H_2.[20] Olefin insertion into the metal–boron bond produces **10**, which reacts with H_2 to yield **11** that can reductively eliminate alkylborane to yield **7**.
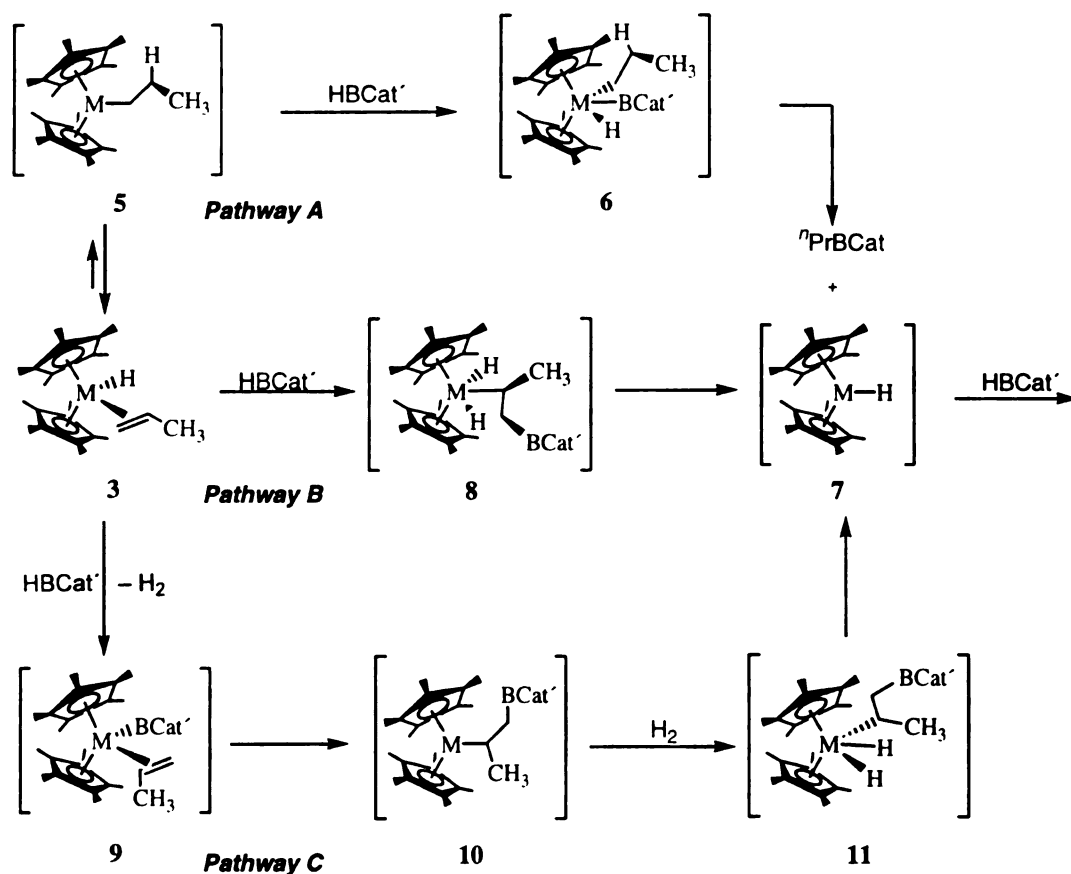
Figure 28. Formation of **7** leading to the synthesis of **4**.

These mechanisms all assume that B–C bond formation occurs at the metal. A common problem that plagues hydroboration mechanisms in early metal systems is the tendency for the metal to effect disproportionation of HBCat to BH_3 and $B_2(Cat)_3$.[35,36] Hence, hydroboration by transient BH_3 can masquerade as hydroboration where B–C bond formation occurs at the metal center. This seems unlikely because B[n]Pr$_3$ was not

30

observed in the reaction mixture. Nevertheless, participation of BH_3 can be definitively addressed by labeling experiments.

Efforts to probe this transformation by a rigorous kinetic analysis were complicated by irreproducible rate constants. Therefore, our mechanistic hypotheses were tested by isotopic labeling and trapping experiments. The reaction of the propylene hydride compound with catecholborane-d (DBCat) provided considerable information with regard to the pathways in Figure 28. When the reactions were monitored by NMR, scrambling of the deuterated borane into the hydride or olefin sites of the olefin complexes was not observed. Thus, reversible B–H/M–H exchange by interaction between catecholborane and olefin complex does not occur. Furthermore, some important conclusions can be drawn from the following observation: the nascent alkylborane products show no deuterium incorporation. Since hydroboration of olefins by DBCat or BD_3, generated from disproportionation of DBCat, would lead to deuterium incorporation in the borane, scenarios where the organoborane products arise from hydroboration of free olefins can be excluded. The isotopic labeling experiment also has significant consequences regarding the mechanistic possibilities in Figure 28. For pathways B and C, deuterated borane products would be expected, given that eliminations from dihydride-d_1 intermediates are common to both mechanisms.[67] Therefore, pathways B and C can be eliminated.

The fate of the deuterium label is revealed by ^2H and ^1H NMR spectra. For the Nb complex, **4**, deuterium is incorporated at niobium–deuteride and Cp* methyl positions in a 90:10 ratio (^2H NMR). This is also confirmed by integrating the resolvable Cp* methyl resonances of the d_0, d_1 and d_2 isotopomers in the ^1H NMR spectra. Label scrambling in the Nb compound is not surprising as deuterium incorporation at the Cp* methyl positions has been observed when $Cp*_2NbH_3$ is treated with D_2.[68] This scrambling was attributed to reversible C–H activation of the Cp* methyl group in **7**.[68] Similar participation of **7** in Figure 28 would account for scrambling of the isotopic label in the

borane adduct complex. When crystalline samples of labeled **4**–d_2 were stored at room temperature for extended periods, the isotopic label at the hydride position gradually diminished and incorporation at the cyclopentadienyl methyl positions was enhanced (^{1}H and ^{2}H NMR). The experimental results from the labeling experiment are most consistent with the mechanism in pathway A.
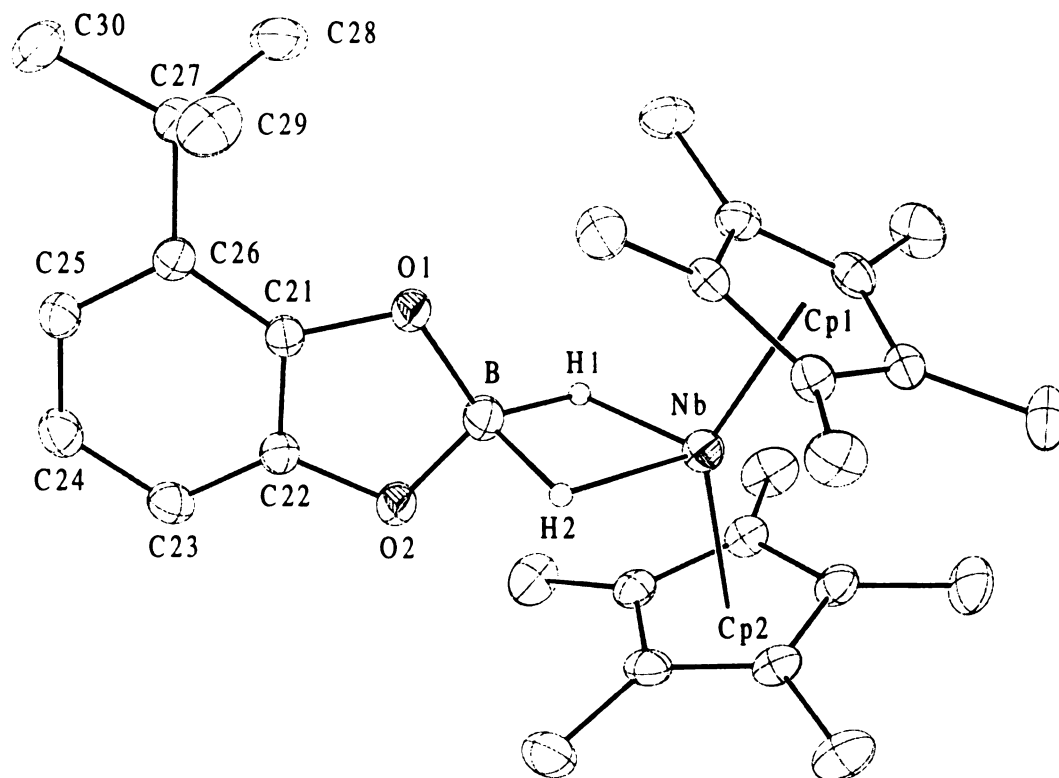
Figure 29. ORTEP diagram of **12**. Thermal ellipsoids are shown at 50% probability.

Suitable crystals of *endo*–Cp*$_2$Nb(H$_2$BO$_2$C$_6$H$_3$–3–^{t}Bu) (**12**), prepared from **3** and HBO$_2$C$_6$H$_3$–3–^{t}Bu, were obtained and the molecular structure was determined (Figure 29). Electron density contour maps were generated to see if the isotropically refined hydride ligands are located in regions of high electron density, and therefore reside in chemically reasonable positions in the crystal structure. Figure 30 shows the electron density contour map for **12** corresponding to the low angle data from the collected data set ($2\theta < 30°$). This clearly shows that the hydride atoms are in the center of high electron

density regions and at structurally reasonable positions. Isotropic refinement of the hydrogen atoms resulted in minimal shifts of their positions.
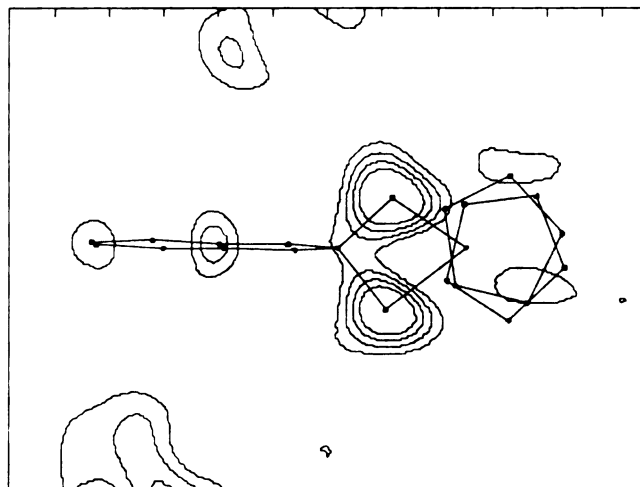
Figure 30. Electron density contour map for **12**.
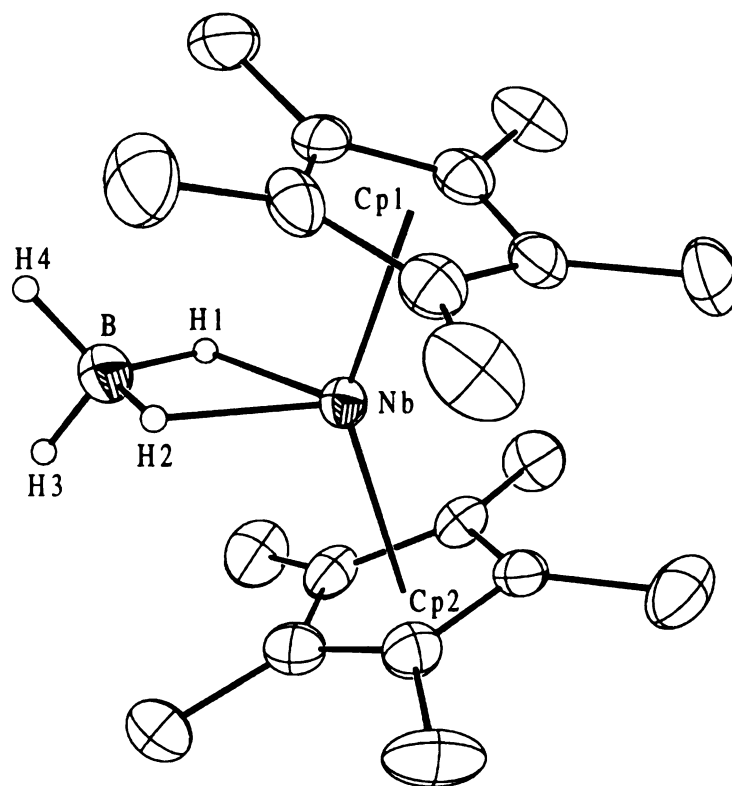
Figure 31. ORTEP diagram of **13**. Thermal ellipsoids are shown at 50% probability.

Since Cp*$_2$NbBH$_4$ (**13**) is a known and readily synthesized compound, its structure provides a benchmark for a bona fide borohydride complex. Suitable single crystals of **13** were grown and the X–ray molecular structure is shown in Figure 31. The Nb–B length in **12** (2.348(4) Å) is identical to the corresponding Nb–B length in **13** and is significantly longer than M–B distances **17** (Table 4). The metal–hydrogen distances for **12** (1.63(4) and 1.86(4) Å) are marginally shorter than those found in **13** (1.79(8) and 1.88(7) Å). The B–H$_{bridging}$ distances for **13** (1.17(7) and 1.16(8) Å) lie in the expected range for B–H$_{bridging}$ bond distances for niobium borohydrides.[69,70] The corresponding distances for **12** are significantly longer (1.36(4) and 1.46(4) Å) but not as long as the corresponding distances for **2** (1.69(4) and 1.62(5) Å)[20] and *endo*–**1** (1.75(5) and 2.11(6) Å).[60] The B–H bond distances of **12** are in good agreement with B–H bond distances of structurally characterized borane heteroatom–dimers.[71-74] Also, the H–Nb–H angle for **12** (73(2)°) is about 15° greater than that found in **13** (58(3)°) and about 20° less than the corresponding angle in **2** (92(2)°)[20] and significantly less than the H–Ta–H angle for *endo*–**1** (113(3)°).[60] After comparing the metrical data for compound **12** to structurally characterized borane adduct, boryl and borohydride complexes, **12** is better formulated as a Nb^{III} endo borane adduct.

Table 4. Selected bond distances and angles.

Compound	M–B distance (Å)	M–H distance (Å)	B–H distance (Å)	H–M–H angle (°)
Cp*$_2$TaH$_2$(BO$_2$ C$_6$H$_3$–4–^{t}Bu)	2.28(1)	1.69(6) 1.68(6)	2.06(6) 1.84(6)	113(3)
Cp*$_2$Nb(H$_2$BO$_2$ C$_6$H$_3$–3–^{t}Bu)	2.348(4)	1.86(4) 1.63(4)	1.46(4) 1.36(4)	73(2)
Cp*$_2$NbBH$_4$	2.346(10)	1.88(7) 1.79(8)	1.17(7) 1.16(8)	58(3)

Isotopic Perturbation of Equilibria

There is also a significant perturbation of resonance in the hydride resonance of **4** when deuteria are introduced in the hydride positions. The hydride/deuterium resonance shifts to higher field with consecutive substitution of deuteria for hydrogen and the magnitude of the perturbation is similar to that seen in the perturbation in **2**.[20] The NMR data for the temperature dependence of the hydride resonances for **4**–d_{0-2} are listed in Table 5. Figure 32 gives a graphical representation of the data displaying that the resonances vary with temperature from –60 °C to 40 °C. The fact that the hydride/deuteride resonances shift to higher field with each deuterium substitution excludes any equilibrium between degenerate structures.

Table 5. NMR data for the hydride resonances of **4**–d_{0-2}.

	^{1}H NMR data		^{2}H NMR data	
Temp (°C)	H_2 resonance (ppm)	HD resonance (ppm)	HD resonance (ppm)	D_2 resonance (ppm)
40	–8.20	–8.56	–8.77	–9.17
20	–8.36	–8.77	–8.96	–9.39
0	–8.48	–8.93	–9.13	–9.58
–20	–8.62	–9.10	–9.31	–9.79
–40	–8.76	–9.26	–9.49	–9.99
–60	–8.89	–9.43	–9.66	–10.16
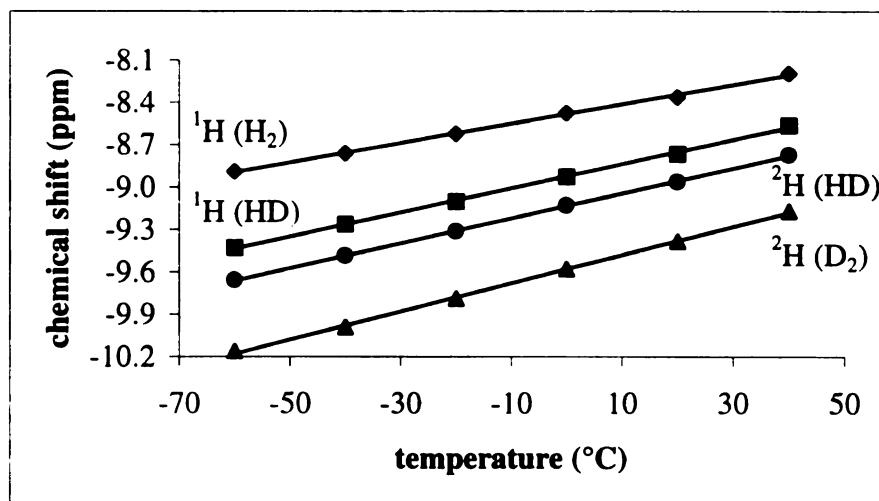
Figure 32. NMR chemical shift data for **4**–d_{0-2}.

An equilibrium between a borylhydride structure and a hydridoborate structure may explain the isotopic perturbation; however, other nondegenerate equilibria could also account for the observed spectroscopic features. Figure 33 displays the possible equilibria that are viable.
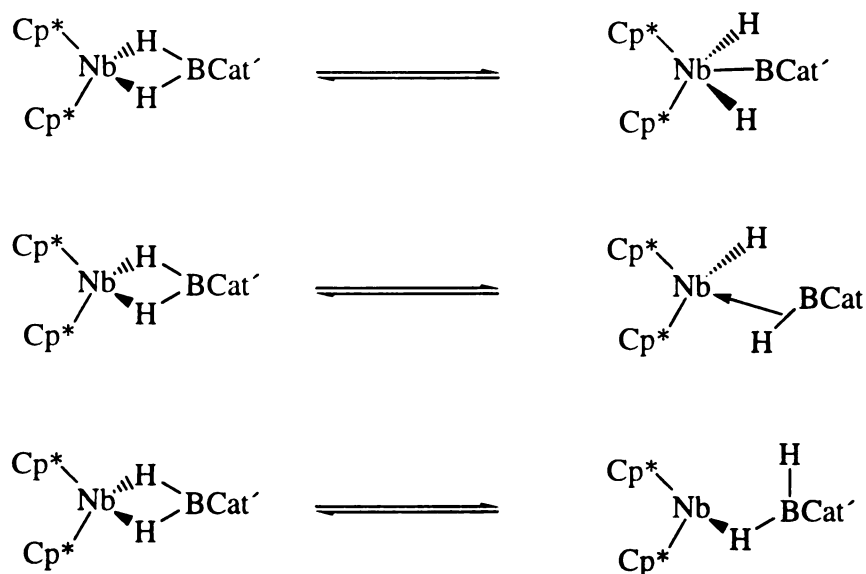
Figure 33. Possible equilibria that can account for the isotopic perturbation of resonance.

Synthesis of a Weakly Bound Borane Adduct Complex: Cp*₂Nb(H₂BPin)

The reaction of **3** with HBPin was investigated to determine if there was a substantial influence on the nature of the metal–boron interaction based on substitution of the boryl fragment. The reaction was carried out in an identical fashion to the reaction of **3** with HBCat'. A ^{1}H NMR spectrum of the deep red crude material revealed a singlet attributed to the Cp* methyl protons, a singlet corresponding to the methyl protons of pinacol fragment and an upfield hydride resonance. The integrated intensities were consistent with the formula Cp*₂Nb(H₂BPin), **(14)**. The ^{1}H NMR spectrum of the recrystallized material differed significantly from that of the crude product. There were two completely new Cp* methyl resonances, which integrated in a 1:1 ratio (Figure 34). The resonance attributed to the methyl groups of the pinacol fragment was absent and the

hydride resonance shifted approximately 7 ppm downfield. Additionally, the ^{11}B NMR spectrum for this compound was silent. Elemental analysis of this compound was consistent with the formula $(Cp*_2NbHN)_x$.
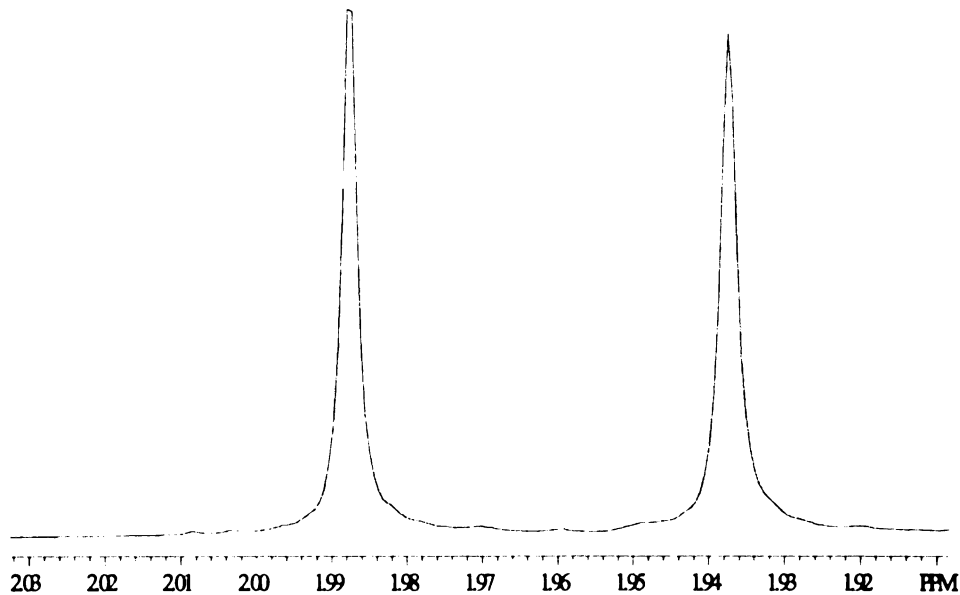
Figure 34. ^{1}H NMR spectrum of the Cp* region of the isolated compound after recrystallization.

The ^{1}H NMR spectrum can be readily explained by invoking a bridging dinitrogen dimer of $Cp*_2NbH$, $(Cp*_2NbH)_2-\mu-N_2$, (**15**). While not immediately obvious, two distinct Cp* resonances should be observed for this compound. From Figure 35, diastereotopic Cp* ligands are labeled either "A" or "B." The inequivalency arises from the relative orientation of the Cp* and hydride ligands. The Cp* ligands labeled "A" are syn to the hydride ligand on the adjacent metal center while the Cp* ligands labeled "B" are anti to the hydride ligand on the adjacent metal center. Thus, two distinct Cp* resonances should be observed in the ^{1}H NMR spectrum.

A

Cp*

H

A

Cp*

H

Nb

N

N

Cp*

Nb

B

Cp*

B
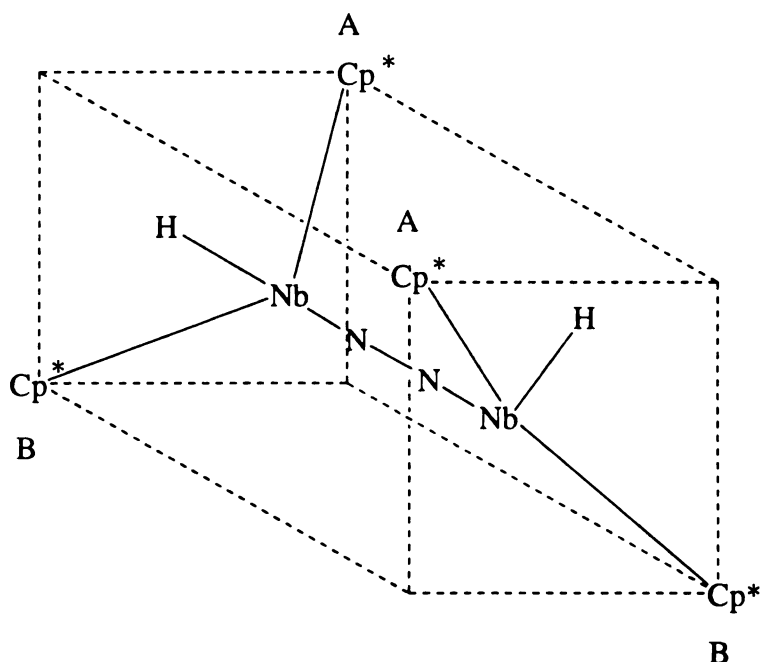
Figure 35. Stick figure diagram displaying the different chemical environments of the Cp* ligands.

In hopes of resolving the N_2 binding environment, an attempt to determine the molecular structure from single crystal X–ray diffraction data was undertaken. A crystal was selected and a data set was collected. A ball and stick diagram of the compound can be seen in Figure 36. Unfortunately, the quality of the data did not allow for a full determination of the crystal structure; however, some comparisons can be made to other bridging dinitrogen compounds. The N1–N2 distance (1.184(7) Å), is longer than the N–N bond distance in molecular N_2 (1.0976 Å)[75], and is similar to the N–N distances for μ–N_2 ligands in $\{Cp*_2ZrN_2\}_2$–μ–N_2 (μ–N_2 distance of 1.182(5) Å),[76] $\{Cp*_2Ti\}_2$–μ–N_2 (1.16(1) and 1.16(1) Å for the two independent molecules)[77] and $\{Cp_2Ti(PMe_3)\}_2$–μ–N_2 (1.191(8) Å).[78] Other group 5 metal compounds with bridging N_2 fragments have been structurally characterized that have significantly longer nitrogen–nitrogen bond lengths corresponding to N=N[79-87] and N–N[88-90] complexes. The Nb1–N1–N2 angle (177.6(5)°) and Nb2–N2–N1 angle (177.4(5)°) are nearly linear and the Cp* rings are arranged in a

38

staggered configuration about the two metal centers, also in agreement with the structurally characterized complexes mentioned above.
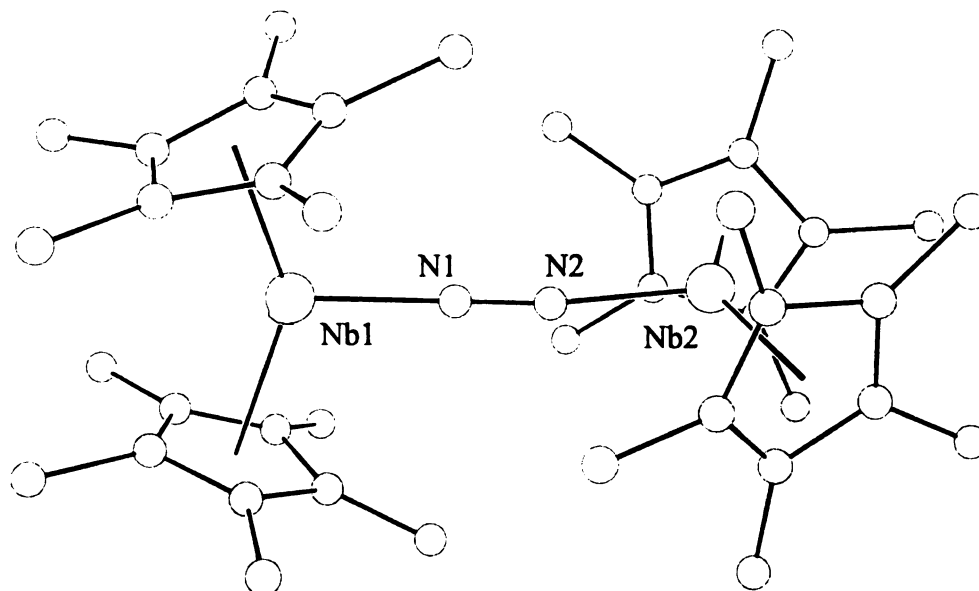
Figure 36. Ball and stick diagram of **15** after recrystallization of **14**.

Cp*₂TaH(olefin) Chemistry

A toluene solution of Cp*$_2$TaH(η^2–CH$_2$=CH(Me)) **(16)** reacted cleanly with HBCat′ to generate a single metal containing product and the alkylborane product n–PrBCat. The isolated metal–containing compound was formulated as *endo*–Cp*$_2$TaH$_2$BO$_2$C$_6$H$_3$–4–^{t}Bu **(17)** based on ^{1}H and ^{11}B NMR data that were similar to the niobium derivative. The only noteworthy differences in the ^{1}H NMR spectra are the lower field (–2.05 ppm) and the narrower line width ($\Delta v_{1/2}$ = 3 Hz) displayed by the hydride resonance. The ^{11}B resonance shifts to lower field in the Ta complex and is similar to that in *endo*–**1** (73 ppm, $\Delta v_{1/2}$ = 610 Hz). Deuterium labeling studies resulted in exclusive incorporation of the label in the hydride positions of the complex. Scrambling from the hydride positions into the methyl resonances of the Cp* ring was not observed in this compound in contrast to the niobium analog. The isotopic labeling results were similar to those for the niobium derivative and are consistent with pathway A in Figure

39

28. Unlike the Nb analog, a temperature dependence for the hydride resonance was not observed over the temperature range investigated (–40 °C to 40 °C).

Table 6. ^{1}H NMR data for the hydride ligands of **17**.

Temp (°C)	Chemical shift (ppm)
–40	–2.16
–20	–2.17
0	–2.17
20	–2.17
40	–2.16

The structural assignment of the decamethylniobocene derivative raises the question as to whether the binding of the H_2BCat' fragment resembles that in *endo*–1 or **12**. Single crystals were grown and isolated from a concentrated toluene solution cooled to –35 °C. The structure was solved and an ORTEP diagram of the molecule is shown in Figure 37. In the solid state, the boryl fragment is no longer eclipsed with the pentamethylcyclopentadienyl ligands, in contrast to *endo*–1 mentioned above (Figure 19). The tantalum–boron distance in this structure (2.28 (1) Å) is similar to the Ta–B distance (2.263(3) Å) in *endo*–1. The boron–hydrogen distances (2.06(6) Å and 1.84(6) Å) are substantially longer than those found in the Cp niobium compound (1.69(4) Å and 1.62(5) Å)[20] and more closely resemble those found in *endo*–1 (1.75(5) Å and 2.11(6) Å),[60] consistent with little boron–hydrogen interaction. The H(1)–Ta–H(2) angle (113(3)°) is identical within experimental error to the corresponding angle in *endo*–1 (113(3)°) and is much larger than the angle for **2** (92(2)°).[20] The metrical parameters for **17** are consistent with a Ta^V boryl formulation.
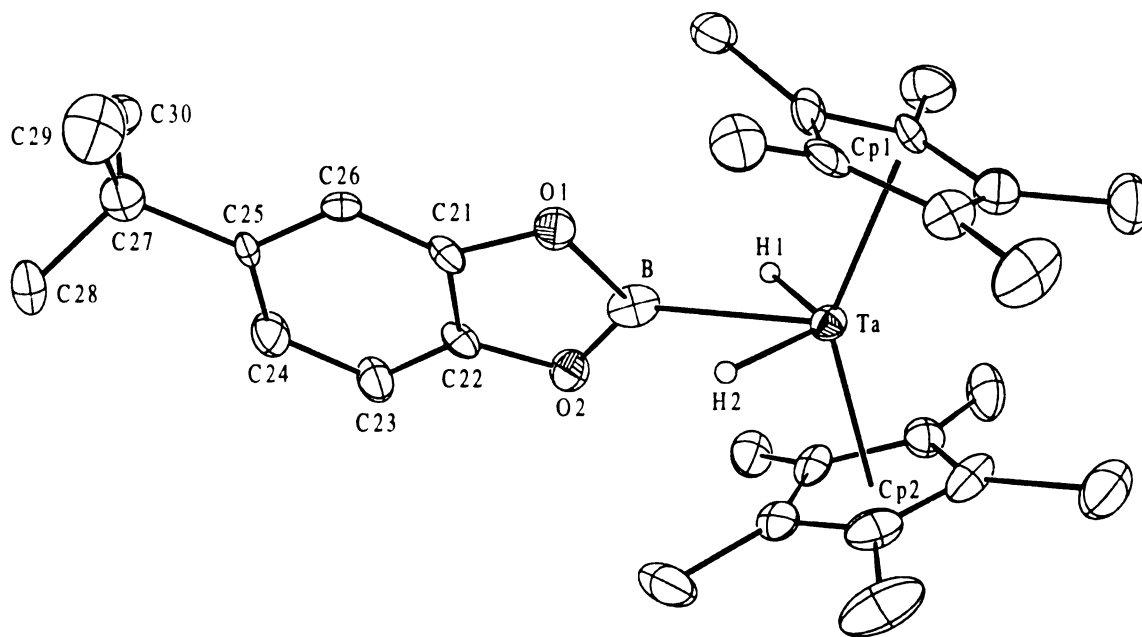
Figure 37. ORTEP diagram of **17**. Thermal ellipsoids are shown at 50% probability.

The indication that there are significant B–H interactions in the niobium compound which are absent in the corresponding tantalum boryl compound is reinforced by the orientation of the BCat fragment in the metallocene wedge. To maximize orbital overlap between the boron p orbital and the hydride ligands a dihedral angle $(Cp^*_{cent}$–Ta–B–O) of nearly 0° is required. Figure 38 displays a view down the metal–boron vector of the two compounds, with the Cp* methyl carbons and the catecholate carbon atoms removed for clarity. As seen in Figure 38, the dihedral angle for the niobium compound is nearly 0° (2.4°) while the same dihedral angle in the tantalum compound is substantially larger, 18.8°. Thus, the orientations of the BCat′ fragment are consistent with the conclusions based on B–H distances. Namely, B–H interactions are present in the niobium compound and absent in the tantalum analog. Since the geometric parameters for the Cp^*_2M fragments are virtually identical, these derivatives differ primarily in the ligation of the $H_2BCat′$ fragment. Valence bond descriptions for the niobium and tantalum redox isomers reflect tantalum's relative preference for a d^0 configuration.

Cp*₂NB(H₂BCat')   Cp*₂TaH₂(BCat')
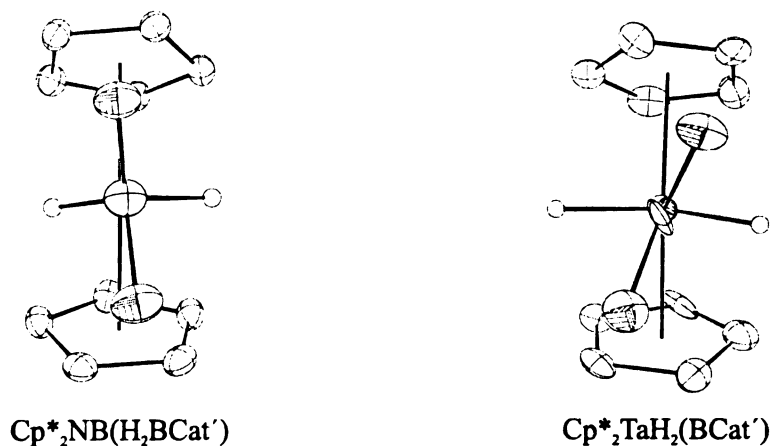
Figure 38. Dihedral angle comparison between **12** and **17**.

Cp₂NbH(olefin) Chemistry

Addition of HBCat to a stirred pale yellow toluene solution of $Cp_2NbH(\eta^2-CH_2=CH_2)$ at room temperature led to the formation of an orange–red solution. During the course of the 18 h reaction, a bright yellow microcrystalline solid precipitated from solution. The bright yellow solid was dried after the filtrate was removed by cannula filtration. The ^1H NMR spectrum contained a single cyclopentadienyl resonance along with an upfield resonance typical of a metal–hydride bond. Two pairs of catecholate resonances could be identified in the ^1H NMR spectrum and the ^{11}B NMR spectrum contained two distinct resonances. The isolated solid was tentatively assigned as a diboryl compound, $Cp_2NbH(Cat)_2$ (**18**). The ^1H and ^{11}B NMR spectra of the red solid isolated from toluene evaporation of the mother liquor were identical to those the previously reported compound, **2**.[20]
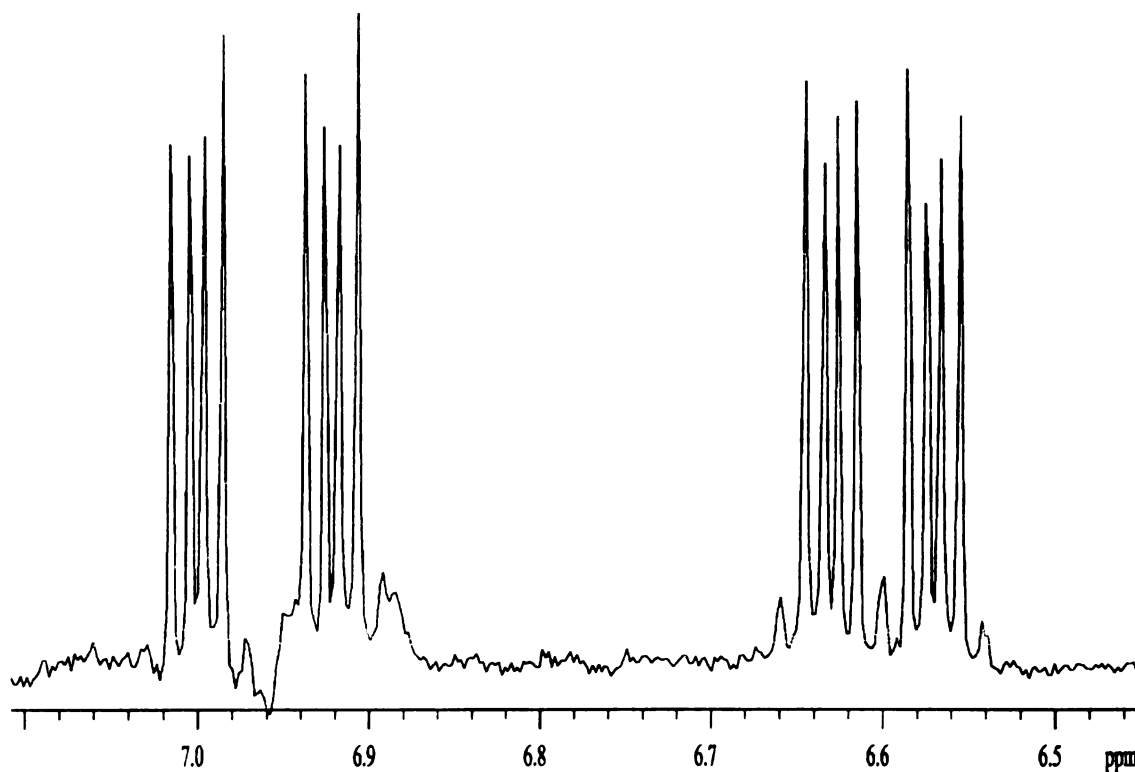
Figure 39. ^{1}H spectrum of the catecholate region for **18** in C_6D_6 (300 MHz, 22 °C).

The hydride resonance in the ^{1}H NMR (C_6D_6) spectrum of **18** appeared as a very broad singlet at δ -7.71 that integrated as one proton versus the cyclopentadienyl resonance. Four equal intensity multiplets at δ 7.00, 6.93, 6.63 and 6.57 (Figure 39) suggest that the two BCat fragments are bound to the metal in a non-symmetric fashion. Coordination of the hydride ligand in an exo position with the boryl fragments bound at endo and exo positions of the metallocene wedge provides a structural model that is consistent with the spectroscopic data. A ^{11}B NMR spectrum also revealed two resonances at δ 64 ($\Delta v_{1/2}$ = 800 Hz) and δ 60 ($\Delta v_{1/2}$ = 310 Hz). ^{1}H{^{11}B} NMR experiments were undertaken in order to assign each of the ^{11}B resonances. The hydride resonance was monitored as the boron resonances were selectively decoupled (Figure 40). The broader resonance (δ 64) was initially thought to be the result of the endo boryl fragment since an interaction with hydrogen was thought to broaden the resonance. However, the hydride peak shape was unchanged when the resonance at 64 ppm was

selectively decoupled. The hydride peak did sharpen moderately when the boron resonance at δ 60 was selectively decoupled. The line width of the boron resonance at δ 60 also decreased when the ^{2}H isotopomer was synthesized. This is consistent with the relative gyromagnetic ratios of ^{1}H and ^{2}H and confirms the interaction between the boryl fragment, whose resonance is located at δ 60, and the hydride. As was observed in *exo*–1, the ^{11}B resonance coupled to the hydride ligand shifts to higher field as compared to the ^{11}B resonance for *endo*–1. The shift of the resonance coupled to the hydride ligand can potentially be rationalized by increased shielding of the boron nucleus by the hydride ligand.
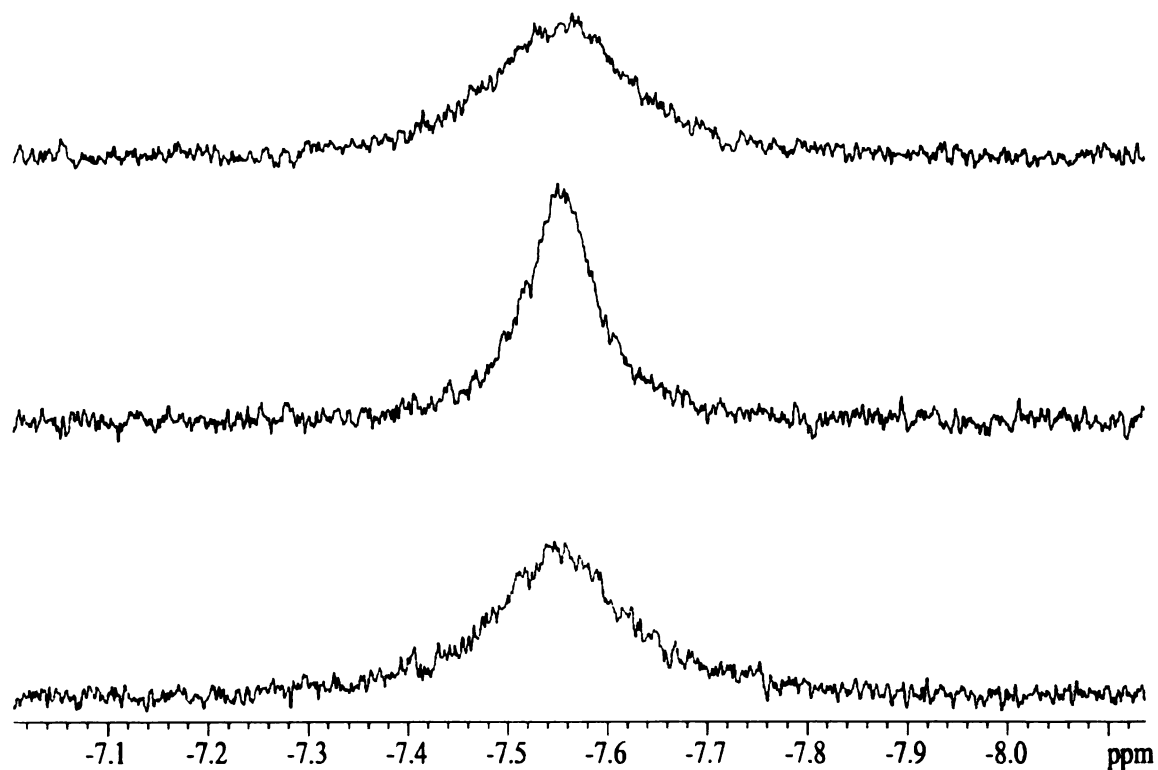
Figure 40. ^{1}H{^{11}B} spectrum selectively decoupled at 64 ppm (top), ^{1}H{^{11}B} spectrum selectively decoupled at 60 ppm (middle) and ^{1}H NMR spectrum (bottom) of **18** taken in C_6D_6 (500 MHz, 60 °C).

44

When the reaction of $Cp_2NbH(\eta^2-CH_2=CH(Me))$ (**19**) and one equivalent of HBCat in toluene-d_8 was monitored by ^1H NMR spectroscopy, propylene gas and traces of propane were observed at early reaction times. In addition to Cp resonances for **2** and **18**, new Cp (δ 4.88) and hydride resonances (δ –4.40, s, $\Delta\nu_{1/2}$ = 6 Hz and δ –6.00, $\Delta\nu_{1/2}$ = 64 Hz) were detected in a 10:1:1 ratio. A NOESY spectrum revealed a cross–peak between the new hydride resonances, and the $^1H\{^{11}B\}$ spectrum showed the resonance at δ –6.00 was coupled to boron. Two new catecholate resonances were also detected at δ 7.08 and δ 6.83. The spectroscopic data are consistent with the catecholate, Cp, and hydride resonances belonging to a single intermediate (**20**) formulated as Cp_2NbH_2BCat The ^{11}B NMR spectrum indicated a resonance at δ 59 ($\Delta\nu_{1/2}$ = 490 Hz). While this may be due to the boron nucleus of **20**, the shift is coincident with that of **2**. It has been shown that chemical shifts in Cp'_2NbH_2BCat (Cp' = Cp or Cp*) complexes can be insensitive to changes in the boron environment.[20,59] Hence, ^{11}B chemical shifts for **20** and **2** could be indistinguishable.

At lower temperatures (–20 °C), a 1:1 molar ratio of HBCat and **19** generates **20** as the major Cp containing product (50% of integrated Cp intensity). Significant quantities of *endo*–**19** (27%), *exo*–**19** (12%), and **2** (11%) were also present, but the intensities of the resonances corresponding to **18** were insignificant. In addition to propylene, small quantities of propane were detected in the initial spectrum. The ratio between the sum of the integrations for the Cp resonances of **20** and **2**, and the integration for the propylene methyl resonance is approximately 10:3. The intensities of the Cp resonances for *exo*–**19** were substantially diminished from its equilibrium value, indicating preferential propylene loss from this isomer.[91] At longer reaction times, the intensity of the propane resonance increases, and resonances for the diboryl compound appear. At 90% conversion, the Cp resonance for **18** and the propane methyl resonance integrate in a 10:7.5 ratio, and the ratio between **2** and **18** was determined to be 1.5:1. Reliable integration could not be made at higher conversion due to precipitation of **18**.

The reaction between **19** and one equivalent of DBCat gave **20** with exclusive deuterium incorporation at δ −6.21 (^{2}H NMR), which corresponds to the hydride resonance at δ − 6.00 in the ^{1}H NMR spectrum (Figure 41). Gradually, a statistical distribution between the positions corresponding to resonances at δ −4.40 and δ −6.21 was reached.
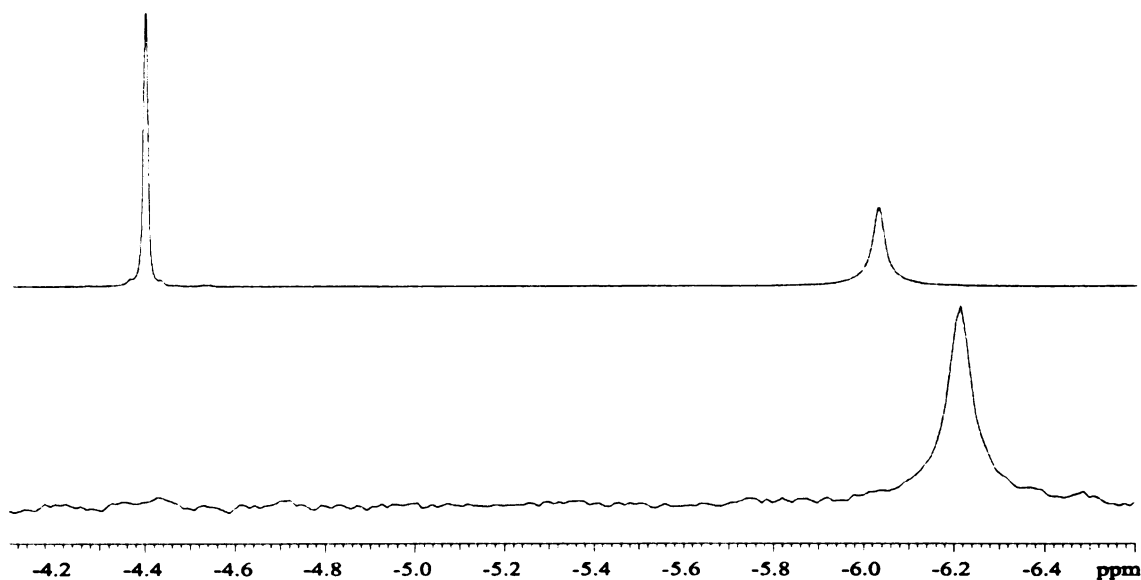
Figure 41. ^{1}H (top) and ^{2}H (bottom) NMR spectra of **20** taken in toluene-d_8 (500 MHz and −20 °C).

The products from the reaction of *exo* and *endo*–**19** with HBCat are distinct from those in the decamethylmetallocene Nb systems and the Ta chemistry described above. Extensive isotopic scrambling in the reaction between *exo* and *endo*–**19** with DBCat limits the application of labeling experiments to probe the mechanism. Nevertheless, Figure 42 provides rationalization for the observed products.[92] As in the decamethylmetallocene mechanism in Figure 28, an alkyl intermediate that arises from olefin insertion into the metal–hydride bond of *endo*–**19** is invoked; however, a key difference between Figure 28 and Figure 42 is the orientation of the borane in the transition state corresponding to B–H activation. Endo and exo orientations of the BCat fragment in the transition state give rise to intermediates with the boryl group in endo and exo positions of the metallocene wedge. In pathway A of Figure 42, B–H activation gives

46

a single intermediate where the boryl ligand is in the endo position. The loss of regioselectivity for B–H activation for Cp relative to Cp* derivatives parallels that observed for olefin binding in Cp (endo or exo) versus Cp* (endo) systems.
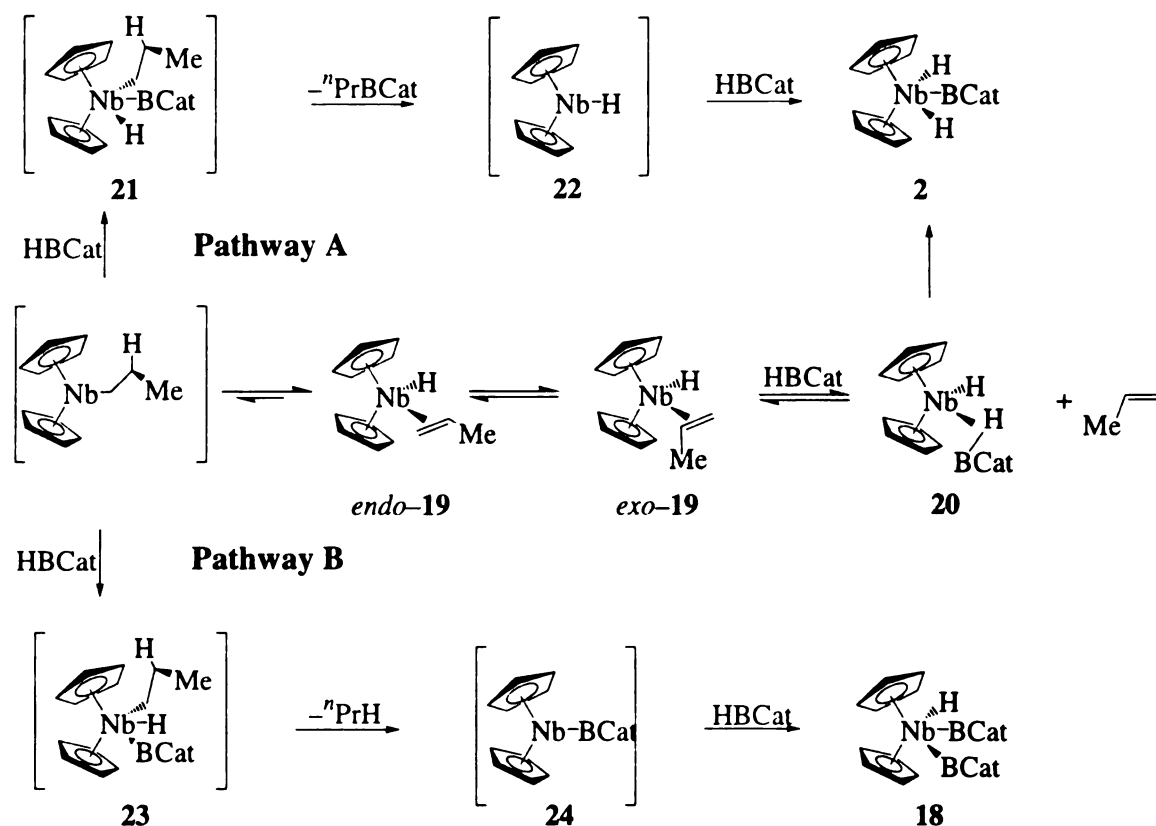
Figure 42. Reaction of **19** with HBCat.

In a sequence analogous to the mechanism in Figure 28, alkylborane elimination from **21** generates **22**, which is trapped by HBCat to generate **2**. This accounts for the formation of n–PrBCat in the reaction mixture. This event is clearly metal–mediated because the uncatalyzed addition of HBCat to propylene is prohibitively slow at ambient temperature. Direct conversion of **20** to **2** provides an alternative to the hydroboration route and accounts for the mass balance between **2** and the sum of propylene and n–PrBCat concentrations.

B–H activation along pathway B generates **23**. Propane elimination from this isomer produces **24** which is trapped by HBCat to form **18**. The 10:7.5 ratio for the

integration of the Cp protons in **18** to the methyl protons of propane is slightly higher than predicted from Figure 42. Two potential complications could account for the deviation from the expected 10:6 ratio. First, small quantities of propane were generated before **18** was detected. Second, the low solubility of **18** resulted in some precipitation at later reaction times. Since the solutions were cooled to ensure dissolution of the propane, it is possible that precipitation of **18** was responsible for the lower ratio of **18** to propane. Significantly, the potential formation of **18** from **2** and HBCat can be excluded since **18** cannot be independently prepared from **2** and HBCat under similar reaction conditions.

Isotopic Perturbation of Equilibria

^{1}H NMR data revealed that the *exo*–**19** reacts preferentially with HBCat to form **20** and propylene. This is consistent with the previous observation that *exo*–**19** reacts with CO to generate Cp$_2$NbH(CO), (**25**), and propylene, while *endo*–**19** reacts with CO to give the olefin insertion product, Cp$_2$Nb(n–C$_3$H$_7$)CO;[93] however, this empirical evidence does not prove that the mechanisms by which propylene is eliminated in reactions of **19** with CO and HBCat are necessarily similar.

Compound **20** reacted with CO (100 psi at 25 °C) to yield compound **25**.[94] When the reaction was complete, the ratio between **25** and **2** was 10:2.2, and residual *endo*–**19** was converted to the propyl carbonyl complex, Cp$_2$Nb(n–Pr)(CO).[93] Independent reactions of **2** and **18** with CO did not generate **25** under similar reaction conditions.

The 200 ppb upfield shift of the boron–coupled deuteride resonance in **20** raises the possibility of equilibrium between a d^0 *exo*–borylhydride structure and a d^2 *exo*–borane adduct structure (Figure 43). Variable temperature NMR experiments indicate small variations in the chemical shifts for the hydride resonances. If contributions from the *exo*–borylhydride isomer to the spectrum of **20** are significant, two–bond coupling between the hydride ligands should be observed. Since $|^2J_{HH}|$ cannot be resolved in spectra of **20** at any temperature, the temperature dependent shifts for the hydride

resonances cannot be conclusively attributed to an equilibrium between an *exo*–borylhydride and an *exo*–borane adduct.
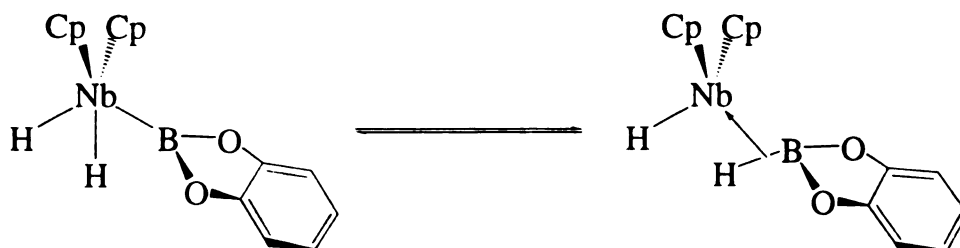
Figure 43. Equilibrium between a d^0 *exo*–borylhydride and a d^2 *exo*–borane adduct.

Compound **18**–*d* was synthesized and the isotopic shift for the hydride resonance (180 ppb) is consistent with significant B–H interactions in **18**. The magnitude is similar to isotopic shifts in compounds **2** and *exo*–**1**, where B–H interactions are present, and substantially larger than isotopic shifts in *endo*–**1**. The chemical shift for the hydride resonance was temperature independent between –80 °C and 25 °C (^{1}H NMR: 300 MHz, thf–d_8).[95]

Two limiting valence bond descriptions that are consistent with B–H interactions inferred from the spectroscopic data are shown in Figure 44. The first is a borane adduct of Nb^{III} where the borane coordination is similar to that observed in Cp$_2$Ti(HBCat)$_2$.[50] The second is a diboryl hydride structure that is similar in ligand displacement to *exo* and *endo*–**1**. The spectroscopic data clearly illustrate limitations of inferences based solely on crystallographic data. Specifically, ^{1}H and ^{11}B NMR spectra clearly show that the boron environments are chemically distinct, which contrasts the crystallographic symmetry (discussed below) that requires equivalent boron positions.

Figure 44. Limiting valence bond descriptions for **18**.

Structure of 20

Although we could not isolate **20**, sufficient concentrations of this species could be generated to collect relevant spectroscopic data. Since $^1H\{^{11}B\}$ spectra prove that the resonance at −6.00 ppm is coupled to boron, formulations for **20** require two chemically inequivalent hydride resonances, one of which is boron coupled. Potential structures that satisfy this requirement are shown in Figure 45. Structures **A** and **B** are borane adducts of Cp_2NbH, structure **C** is the Nb^V analog of the Ta compound, *exo*–**1**, and structure **D** is an O–bound borane adduct of Cp_2NbH.

A   **B**   **C**   **D**
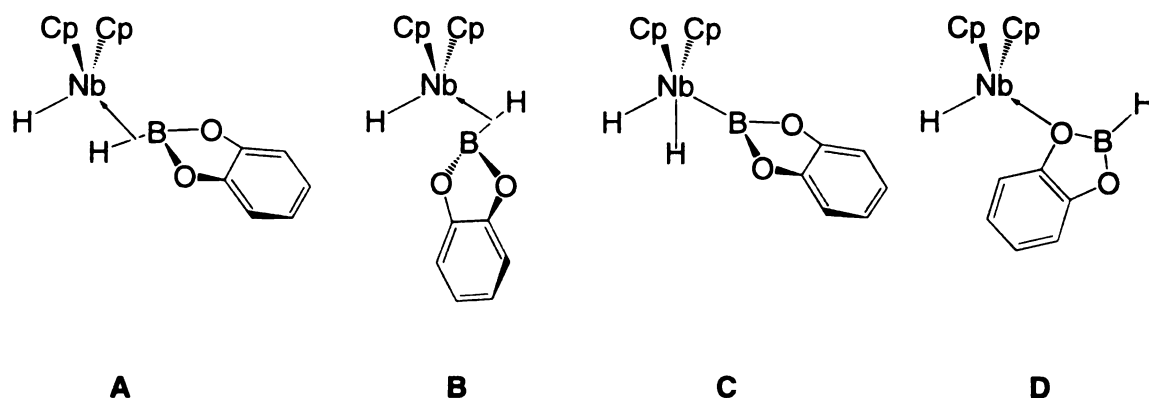
Figure 45. Possible structures for **20**.

Isomer **D** can be excluded for the following reasons. First, two resonances are assigned to the catecholate protons in **20**. Four chemically inequivalent resonances would be expected for the aromatic protons in **D**.[96] Second, $|J_{HB}|$ should be similar to that in HBCat; however, the coupling in **20** is not resolved. Lastly, the high–field shift for the proton coupled to boron is typical for a compound with a metal hydride interaction, and atypical for a three–coordinate dialkoxyborane.

Distinguishing between the remaining possibilities is more difficult. The ease with which borane is eliminated from **20** compares favorably with borane eliminations from borane adducts, and contrasts the reactivity of group 5 boryl complexes. This

circumstantial evidence suggests formulation as a borane adduct (**A** or **B**). A closer examination of the spectroscopic data provides a more rigorous determination.

Since **C** is analogous to the structurally characterized Ta compound, *exo*–1, it should exhibit spectroscopic similarities if it adopted an identical structure.[60] Figure 46 shows ^{1}H and ^{1}H{^{11}B} spectra for **20** and *exo*–1. The chemical shifts for the hydride ligands, and the magnitude of the isotopic perturbation for the upfield resonance, parallel those in *exo*–1. The only disparity between the spectroscopic data for **20** and *exo*–1 is that $|^2J_{HH}|$, which is clearly resolved in *exo*–1 ($|^2J_{HH}|$ = 5.6 Hz), is unresolved for **20**. This difference is significant since similar $|^2J_{HH}|$ values for Cp_2MH_3 (M = Nb, 9–11 Hz;[97,98] M = Ta, 10 Hz[99]) predict that $|^2J_{HH}|$ should be resolved for structure **C**. In Cp_2NbH_3, normal magnetic coupling is masked by exchange coupling, which has equal magnitude and opposite sign at certain temperatures.[98] The fact that $|^2J_{HH}|$ was not resolved in spectra from –60 °C to 20 °C ensures that $|^2J_{HH}|$ is not similarly obscured for **20**. Based on these observations, isomer **C** can be discounted.
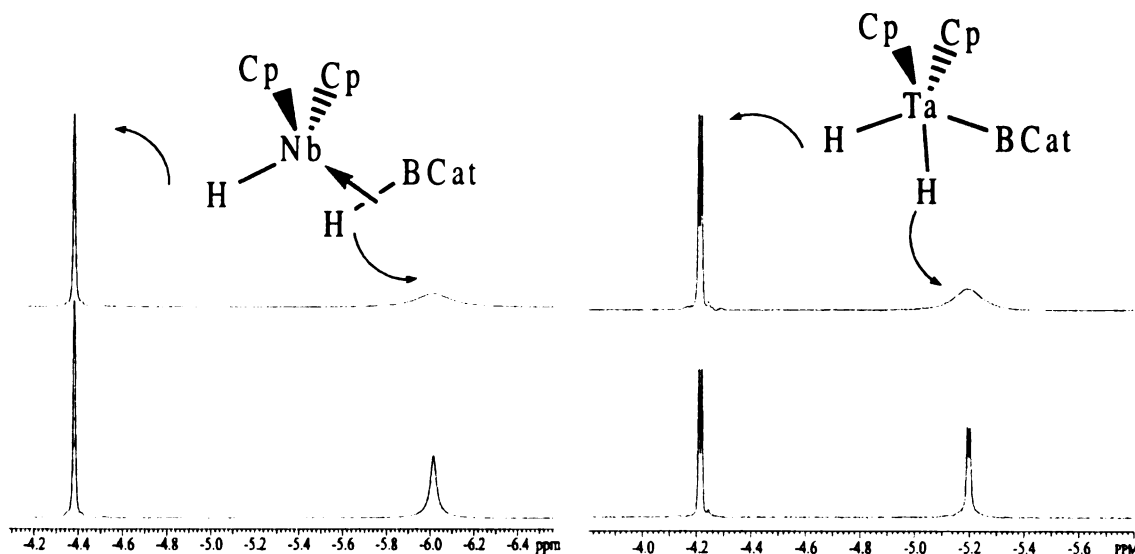
Figure 46. ^{1}H (top) and ^{1}H{^{11}B} (bottom) NMR spectra for **20** and *exo*–1.

Having eliminated isomers **C** and **D**, the formulations that are most consistent with the spectroscopic data are **A** and **B**. The cross peak between the hydride resonances

that is observed in the NOESY spectrum of **20** could arise from nuclear Overhauser effects or chemical exchange. The latter possibility can be rigorously eliminated since exclusive deuterium incorporation at δ –6.21 in the ^{2}H NMR spectrum of **20**–*d* proves that exchange is slow on the NMR time–scale. The NOESY data are consistent with some contribution from **A**, but a cross peak between the hydride resonances would also be expected if equilibrium between **A** and **B** were rapid on the NMR time–scale.

Given that there is no evidence for an equilibrium between isomers **A** and **B**, and the NOESY data support an interaction between the hydride ligands, we favor the exo structure, **A**, for **20**. The irreversible conversion of **20** to **2** suggests a mechanism involving isomerization of **A** to **B**, followed by B–H oxidative addition. It is not clear whether the rate–limiting step should be isomerization or oxidative addition. This could be difficult to probe experimentally; however, evaluation of putative reaction coordinates by computational methods could provide some mechanistic insight.

Compound **20** persisted in solution and gradually converted to **2**. When **2** was prepared from Cp_2NbH_3 and HBCat at room temperature, resonances for **20** were not detected. However, when **2** was heated to 50 °C for 1 h, small quantities of **20** formed. The equilibrium constant calculated for the equilibrium shown in Figure 47 is $K_{eq} =$ 0.120.[100]
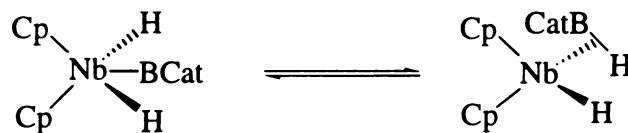
Figure 47. Equilibrium between **2** and **20**.

Single Crystal X–ray Structure of 18

Single crystals were obtained from a concentrated acetone solution cooled to –78 °C as an acetone solvate, and the unique quadrant of the full reflection sphere was collected. Systematic absences were consistent with space groups *Cc* and *C2/c* with

parallel refinements in both space groups converging to similar values of wR2. However, abnormal deviations in the thermal parameters for a majority of the atoms of the Cc refinement suggested the correct space group is C2/c. An ORTEP diagram of the structure is shown in Figure 48. In this setting, the boryl ligands are symmetrically related and the hydride is disordered since the niobium center lies on a C_2 axis.
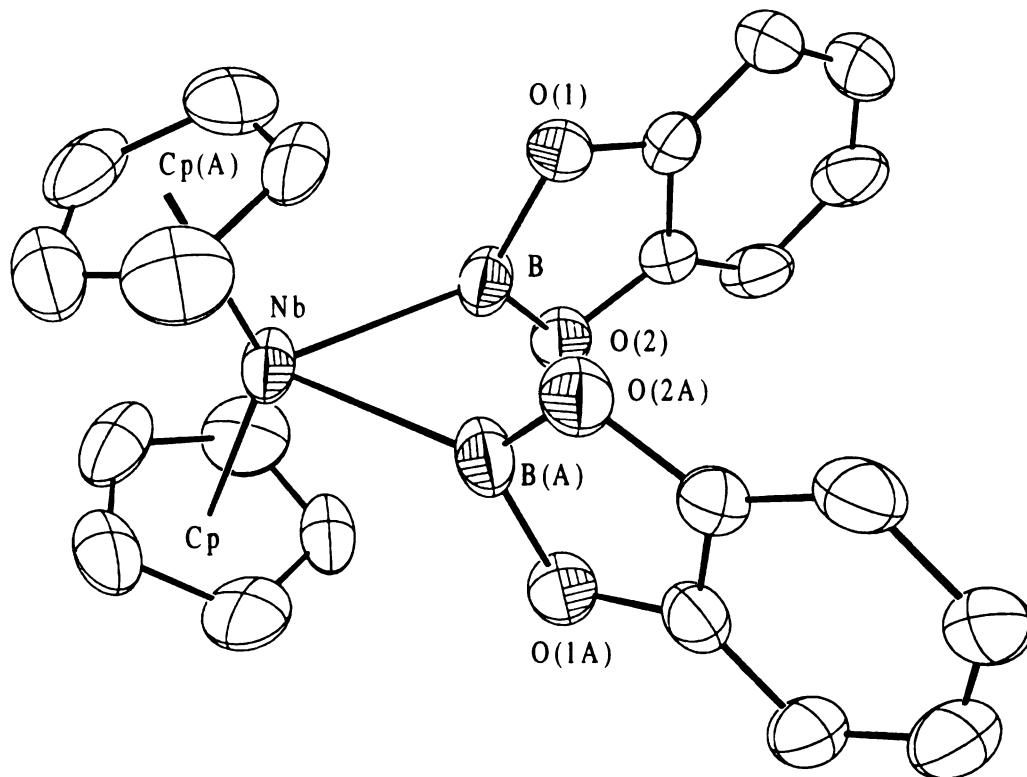
Figure 48. ORTEP diagram of **18** with the hydride omitted. Ellipsoids represent 30% probability for electron density.

The quality of the diffraction data for **18** was marginal. After the final least-squares cycle, the most intense peak in the difference map was located 1.06 Å from B and 1.51 Å from Nb. The peak is oriented exo to the B and B(A) positions, and lies near the plane defined by Nb, B and B(A).[101] The location of this peak is not a reliable indication of the true hydride position since the marginal quality of the data set is further exacerbated by the C_2 crystallographic symmetry at Nb that reduces the hydride intensity

53

to half its normal value. The heavy atom positions are more precisely determined. Hence, the Nb–B distance and the B–Nb–B(A) angle in compound **18** merit comparison to values in related structures.

The Nb–B distance (2.29(1) Å) compares to M–B distances in **2** (Nb–B = 2.292(5)Å) and *exo* and *endo*–**1** (*exo*–**1**, Ta–B = 2.30(1); *endo*–**1**, Ta–B 2.263(6) Å).[20,60] The Nb–B distance is shorter than M–B distances in the borane adducts, **12** (Nb–B = 2.348(4) Å)[59] and $Cp_2Ti(HBCat)_2$ (Ti–B = 2.335(5) Å).[50] The B–Nb–B(A) angle (61°) in **18** is considerably smaller than the B–W–B angle (78°) in $Cp_2W(BO_2C_6H_3$–3,5–*t*–$Bu)_2$,[102] and approaches the value for B–Ti–B angle (54°) in the Ti borane adduct, $Cp_2Ti(HBCat)_2$. The B–Ti–B angle in $Cp_2Ti(HBCat)_2$ is more acute than those typically found in d^2 Cp_2MX_2 species; however, the authors noted that the angle formed by the midpoints of the B–H vectors and the Ti center (81°) falls within the range of those measured for d^2 Cp_2MX_2 compounds.[103] Since the hydride location in **18** is poorly defined, an analogous argument cannot be reliably applied to **18**.[104] The O(1)–B–O(2) plane is rotated by 9.8(7)° from the orthogonal wedge plane.

Compound **18** joins a relatively small family of structurally characterized diboryl complexes.[32,105-111] The fact that the spectroscopic data for **18** indicate chemically distinct boryl units initially suggested the three ligands in the metallocene wedge would adopt a typical geometry for a Cp_2MX_3 compound, such as that found for Cp_2NbH_3.[49] The chemically distinct boryl environments are accounted for if one boryl ligand occupies the endo position of the wedge with the remaining boryl and hydride ligand constrained to exo positions in the metallocene wedge. This situation contrasts the bonding in niobocene and tantalocene disilylhydride complexes, where the silyl ligands are chemically equivalent and occupy exo positions in the metallocene wedge.[112,113] Despite the fact that the hydride position is not resolved in the crystal structure for **18**, the possibility that the hydride bridges the boron atoms can be excluded since resonances corresponding to a single BCat environment would be expected in ^1H and ^{11}B NMR

spectra. The crystallographic equivalence of the boryl ligands in **18** was not anticipated, and it is somewhat surprising that the presence of an adjacent hydride ligand apparently has no structural consequences.

Two limiting valence bond descriptions that are consistent with B–H interactions inferred from the spectroscopic data are in Figure 49. Isomer **E** is a borane adduct of Nb^{III}, where borane coordination is similar to that observed in $Cp_2Ti(HBCat)_2$[50] and $Cp*_2Nb(H_2BCat)$. Isomer **F** is a borylhydride structure that compares to *exo*–**1** and **2**.
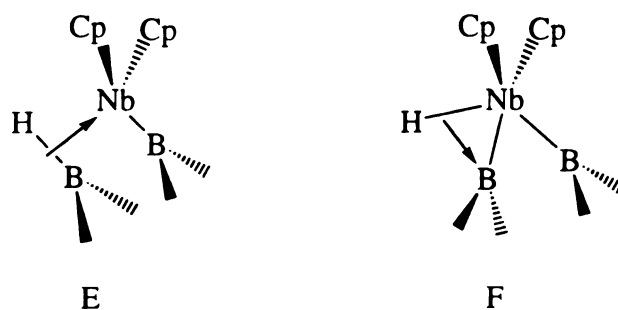
Figure 49. Isomers with possible B–H interactions.

We examined the chemical reactivity of **18** to determine whether its behavior was more consistent with formulation as a Nb^{III} borane adduct or as a Nb^V diborylhydride. The borane adducts, $Cp_2Ti(HBCat)_2$ and **4**, eliminate borane readily to generate the trapping products $Cp_2Ti(CO)_2$ and $Cp*_2NbH(CO)$[114] (**26**) when CO is present. Under similar conditions, HBCat elimination from *exo* and *endo*–**1** and **2** is prohibitively slow. When the reaction between **18** and CO (100 psi, 50 °C, 12 h) was examined, **25** and HBCat were not detected.

Additional information regarding potential elimination reactions is provided by ^1H and ^{11}B NMR data. There is no evidence for boron site exchange via a symmetrical intermediate arising from B–H reductive elimination/oxidative addition since coalescence of BCat resonances is not observed (Figure 50). Rapid HBCat reductive elimination and
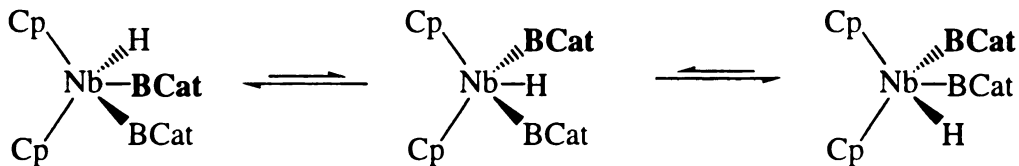
Figure 50. Boryl site exchange through a symmetrical intermediate.

stereospecific B–H oxidative addition, shown in Figure 51, would not lead to coalescence; however, this possibility can be eliminated by the fact that chemical shifts for the BCat resonances are not perturbed when HBCat is added to solutions of **18**.
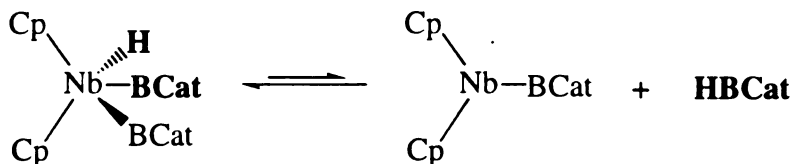
Figure 51. Boryl site exchange through reductive elimination and oxidative addition of HBCat.

The valence bond description for the Nb^V diborylhydride structure is favored for two reasons. First, the Nb–B bond distance is similar to M–B bond distances in other group 5 boryl complexes, and shorter than M–B distances in borane adducts of Nb and Ti. For the borane adduct structure, we would anticipate that the Nb–B distance in **18** would be similar to those for d^2 Nb and Ti complexes. Second, we do not observe borane elimination chemistry that would be expected for this isomer. Although correlations between structure and reactivity of complexes with the generic formulae $Cp'_2MH_x(BCat)_{3-x}$ (x = 1, 2) can be rationalized in valence–bond terms, there are obvious limitations to applying valence–bond models in systems with three–center/two–electron interactions.

Cp₂TaH(olefin) Chemistry

Due to the unexpected reactivity of *exo* and *endo*–**19** seen above, the analogous tantalum complex was also investigated. For the niobium olefin complex, rotation around

the niobium–olefin bond must be rapid relative to boration of $Cp_2Nb(^iPr)$ since secondary alkyl products are not observed. For the tantalum analog, the barrier for rotation is considerably higher. Because of this, secondary boration products might be observed for the tantalum system if olefin rotation is slower than rates of boration of the secondary alkyl intermediate. In contrast to the niobium analog, only $endo$–$Cp_2TaH(\eta^2$–$CH_2=CH(Me))$ (**27**) is produced upon reaction of Cp_2TaCl_2 and n–propylmagnesium chloride, and not the exo/endo mixture. Instead, an isomeric mixture (41% exo, 59% endo) can be generated by irradiating a toluene solution of pure $endo$–**27** under an atmosphere of propylene gas for 4 h using a Rayonet reactor equipped with 300 nm lamps.

An isomeric mixture of exo and $endo$–**27** reacted with HBCat to yield $endo$–**1** and n–PrBCat as the major products. Although traces of the other possible regioisomer, exo–**1** were present in the reaction mixture, $endo$–**1** could be isolated in 78% yield. When the reaction was monitored by ^1H NMR, the intensity of resonances assigned to $endo$–**27** diminished leaving exo–**27** as the predominant isomer. When the reaction was complete, exo–**27** was also consumed. The only organic hydroboration product observed was the anti–Markovnikov product, n–PrBCat. Presumably the exo isomer isomerizes to the endo form which then reacts with HBCat, accounting for the single hydroboration product.

The analogous reaction employing DBCat gave $endo$–**1**–d_{0-2} and n–PrBCat. Integration of a ^2H NMR spectrum gave a 40:60 ratio for deuterium incorporation into the alkylborane and the deuteride resonances of $endo$–**1**–d_{1-2}, respectively. For the alkylborane product, the deuterium label is almost exclusively incorporated at the α–position. When the reaction was monitored by ^2H NMR, exchange into the hydride positions of exo and $endo$–**27** was not detected.

Clearly, H/D exchange occurs by some mechanism in the Ta system. Three potential mechanisms could account for the exchange, and by examining the experimental data the likelihood for these possibilities can be assessed. First, potential

hydroboration of free propylene by DBCat or transient B_2D_6 must be addressed (Figure 52). Either possibility should give alkylborane products with deuterium incorporation at the β-positions. Therefore, α-deuteration cannot be reconciled by uncatalyzed additions. Clearly, the experimental data are inconsistent with hydroboration of uncoordinated olefin.
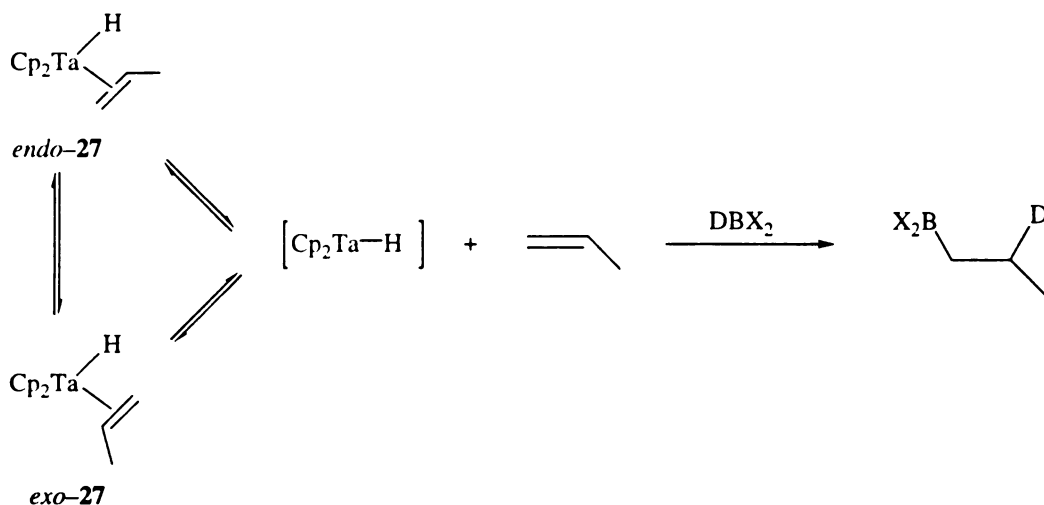
Figure 52. Hydroboration of free propylene.

In the second scenario (Figure 53), scrambling between B–D and Ta–H positions in **27** could occur prior to propylene insertion into the Ta–H/D bond. Incorporation at the α position could be accounted for by B–D/Ta–H scrambling in *exo*–**27**. Insertion of coordinated propylene into a Ta–D bond gives an isopropyl intermediate with deuterium at a methyl position. If rotation about the Ta–C bond is sufficiently rapid, β–H elimination from this intermediate will give *exo*–**27**–d_1 with deuterium incorporation at α and γ positions.[115] For *endo*–**27**, propylene insertion into a Ta–D bond generates an *n*–propyl intermediate with deuterium at the β position. Subsequent β–D elimination from the propyl intermediate will generate the starting isotopomer with a Ta–D bond, while β–H elimination generates the Ta–H isotopomer with deuterium at the propylene β site.[115,116]
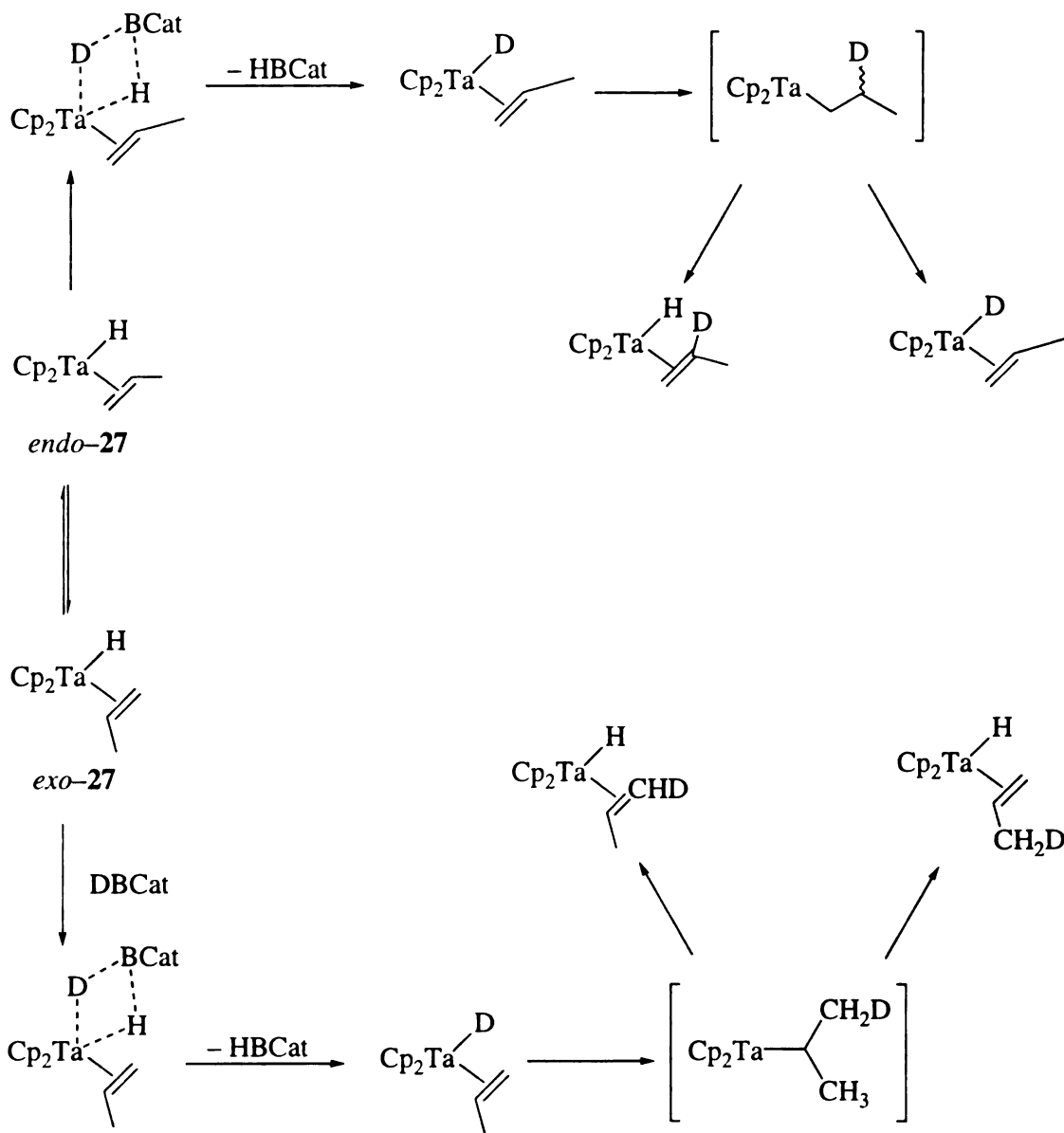
Figure 53. Deuterium label scrambling prior to propylene insertion in the metal hydride bond.

The previous pathway can be excluded as a significant contributor in the deuterium scrambling process. Although the small quantity of β–deuterium incorporation in n–PrBCat–d could result from Ta–H/B–D exchange, this mechanism does not account for predominant incorporation at the α site since a nearly statistical distribution of the label between α and γ sites of coordinated propylene would be anticipated. Furthermore,

exchange between Ta–H and B–D positions in the propylene hydride complexes should result in significant deuterium incorporation at the hydride positions in *exo* and *endo–27*. This possibility was readily tested by using ^{2}H NMR to monitor the reaction as the deuteride shifts for *exo* and *endo–27* and the boryl products *exo* and *endo–1* are clearly resolved. Deuterium exchange into the hydride or propylene sites of *exo* and *endo–27* was not detected. Since selective deuterium incorporation at the α-position and an absence of deuterium incorporation into the *exo* and *endo–27* hydride positions cannot be reconciled by Ta–H/B–D scrambling between *exo* and *endo–27* and DBCat, this mechanism can be excluded.
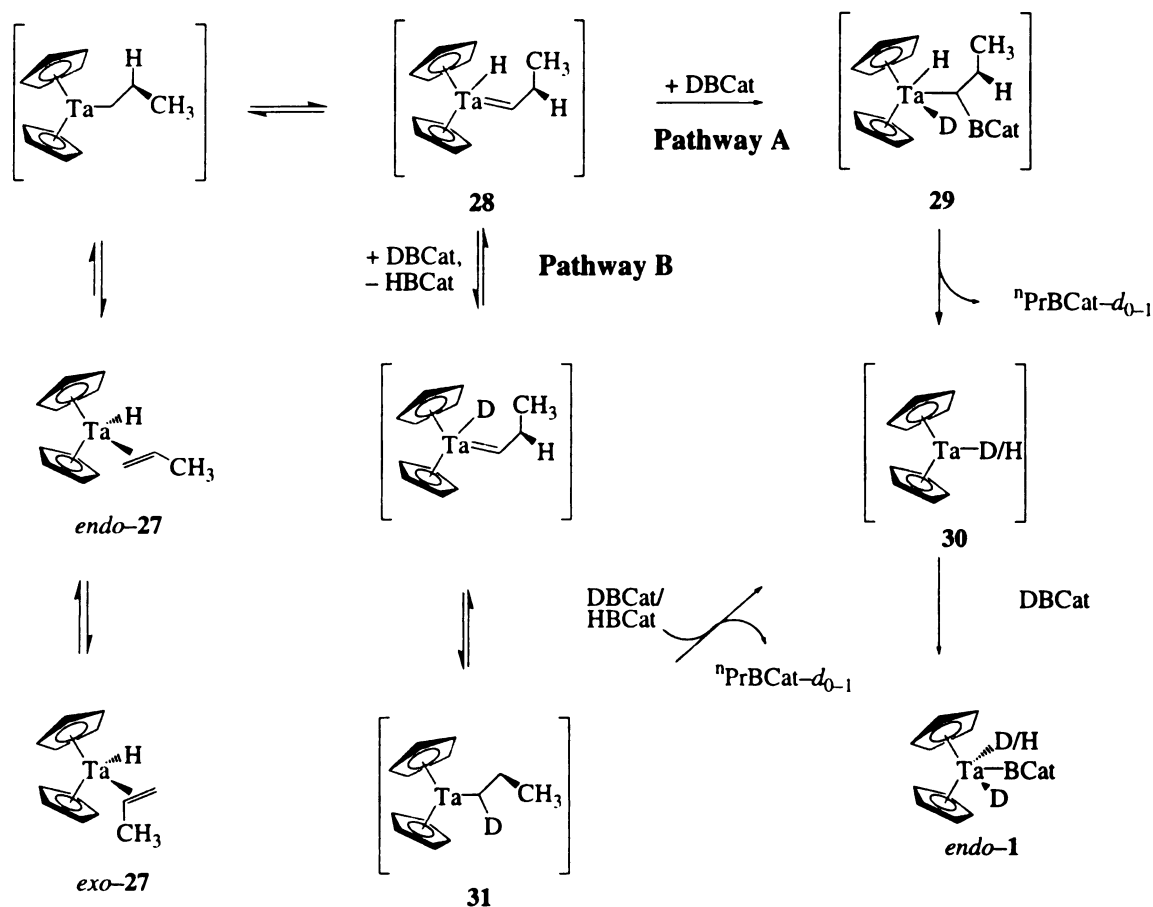
Figure 54. Mechanism for *endo–1* formation.

60

The exclusive incorporation at the α-position of the borane can be reconciled by considering mechanisms that involve an alkylidene intermediate (**28**) in Figure 54. The fact that alkylidene complexes $Cp_2Ta(=CH_2)(CH_3)$[117] and $Cp*_2TaH(=CH_2)$[118] have been isolated supports the accessibility of **28**. Two pathways that involve this intermediate could account for deuterium incorporation at the α position of n-PrBCat. In pathway A, B–C bond formation proceeds via σ-bond metathesis between DBCat and the Ta=C bond in **28** to generate an alkylborane intermediate, **29**. Reductive elimination from **29** generates n-PrBCat-d_{0-1} and Cp_2TaH-d_{0-1}, (**30**), which is then trapped by DBCat to give *endo*–**1**.

Pathway B invokes scrambling between B–D and Ta–H sites in **28**. Reversible α-migration generates **31** with deuterium incorporation in the α-position. Alkylborane formation via B–H oxidative addition and subsequent B–C reductive elimination generates **30**, which is trapped by catecholborane-d_{0-1} to yield *endo*–**1**-d_{0-2}. For pathway B, deuterium scrambling should be reflected by diminished relative intensities for the α-proton resonances of the coordinated propylene ligand in *endo*–**27**, and it should be possible to detect HBCat by ^{11}B NMR due to the fact that $|J_{HB}|$ is clearly resolved.

When the reaction between DBCat and *endo*–**27** was monitored by ^{1}H NMR, the ratio between the integration of the α-proton resonances of the olefin and the Cp resonance remained constant through two half–lives. In addition, formation of HBCat could not be detected by ^{11}B NMR. These observations are inconsistent with scrambling via pathway B. Thus, the most reasonable mechanism that accounts for the isotopic incorporation is pathway A. Integration of ^{2}H NMR spectra gave a 40:60 ratio between the α-methylene resonance in n-PrBCat and the Ta–D resonances. However, deuterium incorporation is more accurately determined by comparing α-methylene and methyl resonances in ^{1}H NMR spectra of n-PrBCat.[119] Since ^{2}H NMR spectra did not indicate deuterium incorporation at the methyl position of the alkylborane, the methyl resonance provides a reliable internal standard. The ratio between α-methylene and methyl

resonances (1.5:3) implies that the effect of k_H/k_D for reductive elimination from the alkylborane intermediate is negligible.

CHAPTER 3

ELIMINATION CHEMISTRY FROM BENT METALLOCENE SYSTEMS

Reactions of Cp*$_2$Nb(H$_2$BCat´)

The niobium–boron linkage of **4** is reactive with various small molecules. The reactions shown in Figure 55 proceed at room temperature generating HBCat´ as one of the products. Compound **4** reacts with CO, discussed in detail below, to form **26**. Compound **4** also reacts with BH$_3$ (B$_2$H$_6$) and H$_2$ forming **13** and Cp*$_2$NbH$_3$, respectively.[114] The reaction with H$_2$ gas is interesting because **4** can be synthesized from addition of catecholborane to Cp*$_2$NbH$_3$.

Another interesting reaction occurs upon addition of olefins. Compound **4** reacts with CH$_2$=CH(R) (R = H, Me) to form free catecholborane and Cp*$_2$NbH(η^2– CH$_2$=CH(R)) (^{1}H and ^{11}B NMR spectra). The formation of Cp*$_2$NbH(η^2–CH$_2$=CH(R)) is significant since the original niobium boryl complex is synthesized from the olefin complex with HBCat. The reaction of **4** with propylene was monitored in a sealed NMR tube. ^{1}H and ^{11}B NMR spectra revealed a gradual decrease in [HBCat´] and a corresponding increase in alkylborane concentration. Upon consumption of all the HBCat´, the metal containing products were **3** and **13**.
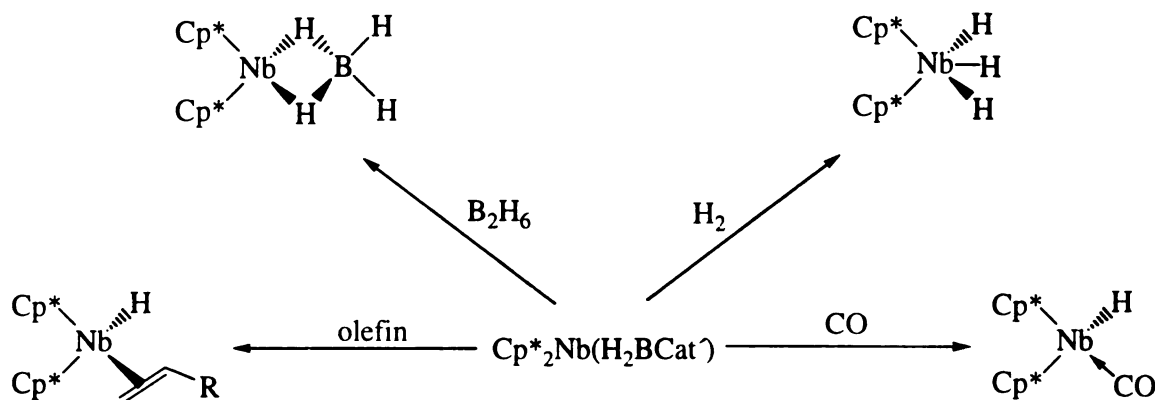
Figure 55. Reactivity of **4**.

The presence of significant quantities of **13** prompted the question whether olefin hydroboration was occurring at the metal center or was accomplished by some other pathway that utilizing BH_3. To address this concern, the reaction of **3** with HBCat´ was performed in the presence of excess cyclooctene and propylene. Cyclooctene is used because it coordinates poorly to the Cp^*_2NbH intermediate due to steric factors.[120] The uncatalyzed hydroboration rates for propylene and cyclooctene are competitive (the ratio for uncatalyzed hydroboration products of propylene:cyclooctene = 0.93:1).[121] Thus, any B–C forming pathway that does not involve the metal should give appreciable quantities of cyclooctene hydroboration products. In this case, **3** is converted to **4** and $^nPrBCat´$ is the primary alkylborane product observed (the ratio for catalyzed hydroboration products of propylene:cyclooctene = 4.53:1).

Two aspects for an effective catalytic hydroboration cycle must be addressed. The first is the rate for B–C bond formation and the second is the rate for B–H elimination to regenerate the olefin complex. Boron–carbon bond formation is rapid for the reaction of **3** with any $HB(OR)_2$ functionalized borane $((OR)_2 \equiv Cat$ or Pin). For this aspect of catalytic hydroboration, the choice of borane is not important under the investigated conditions.

In contrast, the borane utilized greatly affects the rate for B–H elimination and therefore plays a major role in the effectiveness of catalytic hydroboration in these systems. In order for the catalytic cycle to be viable, the coordinated borane adduct must be easily replaced by an olefin. As will be discussed below in quantitative terms, borane adduct coordination to the niobium metal center is dependent on the borane used. Qualitatively, this is evident by the formation of **15** by placing **14** under an atmosphere of N_2. The HBCat family of boranes does not yield **15** even when placed under high pressures of N_2 (up to 200 psi N_2). This simple experiment clearly demonstrates the weaker borane adduct binding of HBPin compared to the catecholate family of boranes. This parallels the tendency for borane coordination of Lewis bases where HBCat derivatives form stable Lewis acid–base adducts with amines, whereas HBPin does not.

Niobium Rate Law Determination for the Reaction of 4 plus CO

The reaction of **4** with CO proceeded cleanly with formation of **26** and free HBCat′. The clean reactivity witnessed for this reaction makes these compounds ideally suited for mechanistic investigation. The lack of decomposition products or competing side reactions allows rate dependencies to be definitively established. It was evident from initial experiments that the reaction was inhibited by excess borane since plots of ln[4] versus time were non–linear at lower CO pressures. This suggested a mechanism were preequilibrium dissociation of HBCat′ generates the sixteen electron hydride complex, Cp*$_2$NbH, which is subsequently trapped by CO. Application of the steady–state approximation yields the rate law shown in Figure 56.
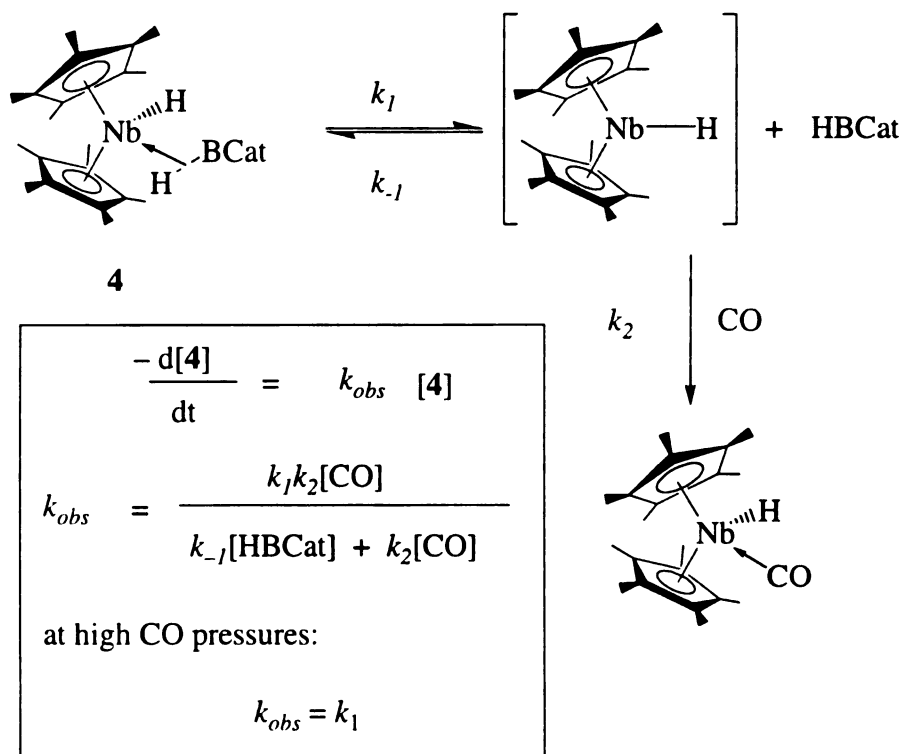
Figure 56. Mechanism and rate law of **4** plus CO.

Rearrangement of the rate law from Figure 56 yields equation **8**. From this equation, plots of $1/k_{obs}$ versus [HBCat′] and 1/[CO] should be linear. Figure 57 and Figure 58 show this to be the case. Also, the y–intercept in Figure 57 yields a value for k_1

when [HBCat'] = 0 that is very close to those measured in independent runs with no added borane.

$$k_{obs} = \frac{k_1 k_2 [CO]}{k_{-1}[HBCat'] + k_2[CO]} \tag{6}$$

$$\frac{1}{k_{obs}} = \frac{k_{-1}[HBCat']}{k_1 k_2 [CO]} + \frac{k_2[CO]}{k_1 k_2 [CO]} \tag{7}$$

$$\frac{1}{k_{obs}} = \frac{k_{-1}[HBCat']}{k_1 k_2 [CO]} + \frac{1}{k_1} \tag{8}$$
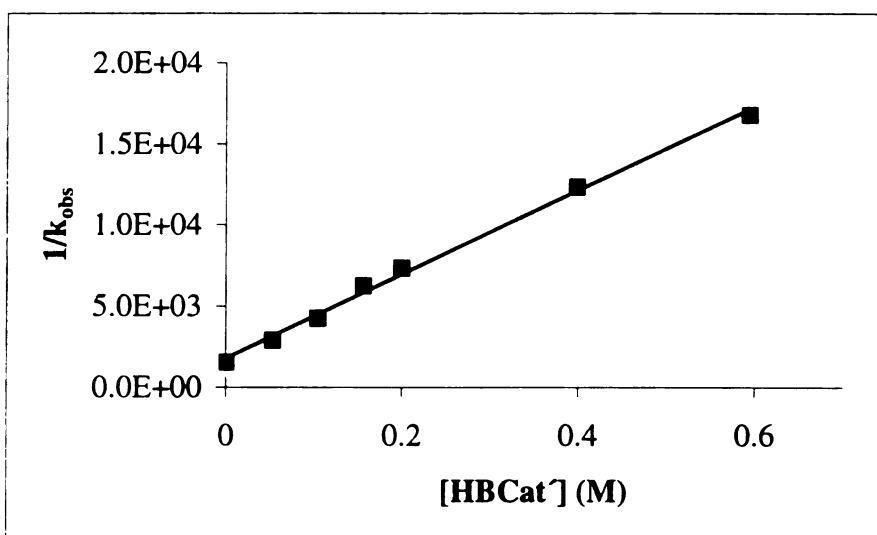
Figure 57. Plot of $1/k_{obs}$ versus [HBCat'].
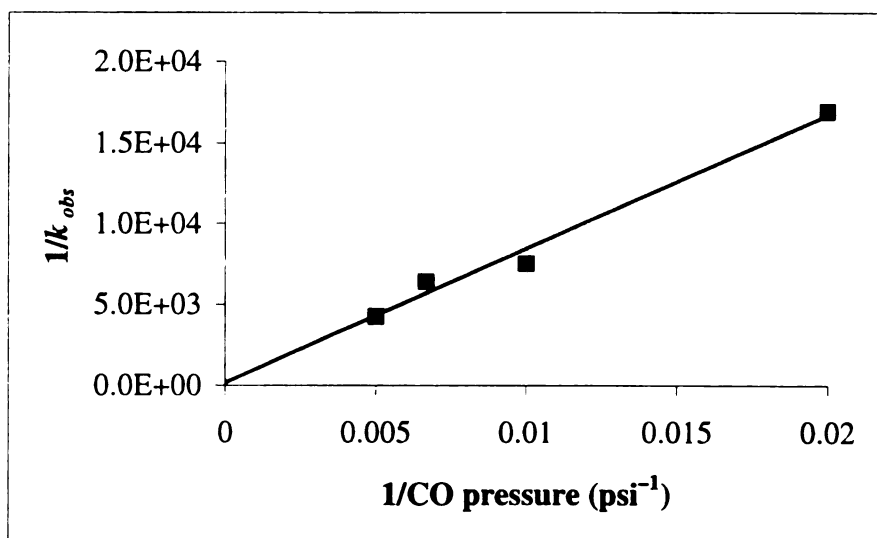
Figure 58. Plot of $1/k_{obs}$ versus 1/CO pressure.

66

Based on the rate law in Figure 56, under sufficiently high CO pressures, k_{obs} should approach a limiting value of k_1 if k_{-1}[HBCat'] « k_2[CO]. This was confirmed when running the reactions at CO pressures > 50 psi. Competitive reversible coordination of HBCat' results in non–linear first order decay plots when running the reaction under lower CO pressures.

Since measurement of k_{obs} at high CO pressures gives k_1, which relates to borane adduct dissociation, the temperature dependence of the rate was examined in order to extract activation parameters. The Eyring plot in Figure 59 yielded activation parameters of $\Delta H^{\ddagger}$ = 23(1) kcal/mol and $\Delta S^{\ddagger}$ = 12(4) e.u. for the elimination reaction. These values are consistent with a dissociative step; however, k_1 was not determined over a substantially large temperature range due to rapid reaction rates above 25 °C and prohibitively slow reaction rates at temperatures below –20 °C which may contribute to the relatively large errors associated with $\Delta H^{\ddagger}$ and $\Delta S^{\ddagger}$.
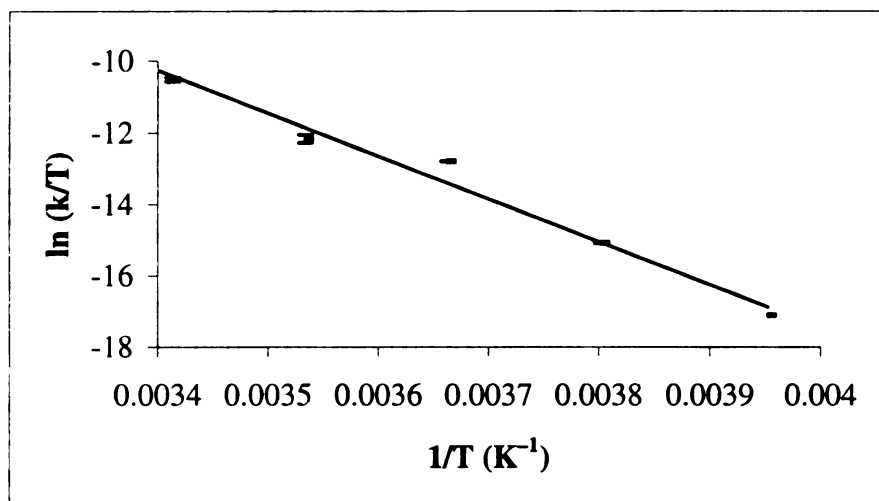
Figure 59. Eyring plot for the reaction of **4** plus CO.

The thermodynamics of borane binding were examined in the Nb system by measuring equilibria between alkyl substituted catecholborane derivatives. $\Delta\Delta G$ values relative to Cp*₂Nb(H₂BCat) are given in Table 7. If the assumption is made that substitution on the catechol backbone has negligible effects on B–H bond energies, $\Delta\Delta G$

reflects the relative ground state energies of the borane adducts, Cp*$_2$Nb(H$_2$BCat$'$). The observed trend is consistent with an increase in steric interactions between the borane adduct and the pentamethylcyclopentadienyl groups following the order HBO$_2$C$_6$H$_4$ < HBO$_2$C$_6$H$_3$–4–^{t}Bu < HBO$_2$C$_6$H$_3$–3–^{t}Bu. The equilibrium between HBPin and **4** could not be measured, indicating that borane adduct association in **14** is much weaker than in the catecholate based systems.

Table 7. $\Delta\Delta$G values for the equilibria:

Cp*$_2$Nb(H$_2$BCat) + HBCat$'$ $\rightleftharpoons$ Cp*$_2$Nb(H$_2$BCat$'$) + HBCat   (25 °C, C$_6$D$_6$).

HBCat$'$	$\Delta\Delta$G (kcal/mol)
HBO$_2$C$_6$H$_3$–4–^{t}Bu	0.26(2)
HBO$_2$C$_6$H$_3$–3–^{t}Bu	0.96(2)
HBPin	> 5.8

Deuterium Isotope Eeffect

The labeled compound, **4**–d_2, was synthesized using the same method used for the unlabelled compound using DBCat$'$ in place of HBCat$'$. Obtaining an isotopically pure compound was not trivial due to scrambling between the Nb–D and methyl hydrogen positions of the Cp* ring system.[68] Deuterium incorporation was enhanced by recrystallizing **4**–d_2 in the presence of excess DBCat$'$ (~ 84% of all Nb–X bonds were Nb–D bonds). Over the course of several weeks, even in the solid state, slight incorporation of deuterium into the methyl positions of the Cp* ring could be detected in ^{2}H NMR spectra.

Kinetic reactions were performed on freshly prepared deuterium labeled compound under identical conditions as those of the unlabeled compound. An inverse isotope effect was noted for the reaction with CO (k_H/k_D = 0.68(3)), Figure 60. It should be noted that the observed inverse isotope effect is the result of both primary and secondary isotope effects. Since the mixed hydride species **4**–d_1 could be
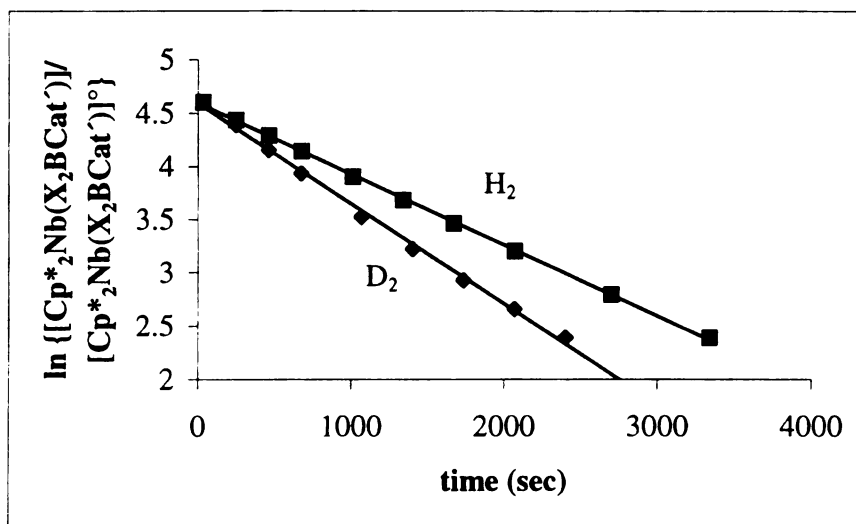
Figure 60. Plot of $4-d_{0.2}$ plus CO.

synthesized by mixing equal quantities of **4** and **4**–d_2 resulting in rapid scrambling in the hydride positions generating a nearly statistical mixture of **4**, **4**–d_1 and **4**–d_2 (all three isomers are readily discernable by their Cp* resonances), there is a possibility the two effects can be separated. Within experimental error, the reaction rates for **4**–d_1 and **4**–d_2 with CO are identical. The reaction was not monitored by ^{11}B NMR spectroscopy which would potentially give the relative rate of HBCat′ elimination to DBCat′ elimination from **4**–d_1. The relative reaction rate could be used to calculate a secondary isotope effect should one be present. Secondary isotope effects usually occur when deuterium is substituted on an atom that changes hybridization. In this case, the secondary isotope effect would appear to be negligible since the boron and niobium atoms do not rehybridize from reactants to products and the identical reaction rates for **4**–d_1 and **4**–d_2. In addition, the zero–point energy of DBCat′ is lower than HBCat′ shifting a preequilibrium favoring [Cp*$_2$NbD] and free borane when deuteria are bound to the metal center which explains why **4**–d_2 reacts faster than **4**. Transition metal catalyzed olefin hydrogenation reactions may also be explained in terms of a preequilibrium isotope effect.[122-130]

69

Tantalum Rate Law Determination for the Reaction of 17 plus CO

The reaction of **17** with CO resulted in clean formation of HBCat′ and Cp*$_2$TaH(CO),[68] (**32**). An investigation of the reaction mechanism was conducted since the ground states energies for **4** and **17** may differ leading to distinct pathways.

Though chemically analogous to the reaction between CO and **4**, the kinetic behavior of **17** differs considerably. When **17** was reacted with excess CO, disappearance of the Ta complex was first–order. The reaction was monitored under various concentrations of free HBCat′ with surprisingly no observed dependence of [HBCat′] upon the reaction rate. The effect of CO pressure on the reaction rate was also investigated, and no [CO] dependence was observed. Based on reaction rate independence on [CO] and [HBCat′], the rate determining step for the mechanism in Figure 61 is presumed to be B–H reductive elimination leading to a [Cp*$_2$TaH] transition state. The mechanistic details are discussed in more detail below.

$$\frac{-d[17]}{dt} = k_{obs} [17]$$

$$k_{obs} = k_1$$
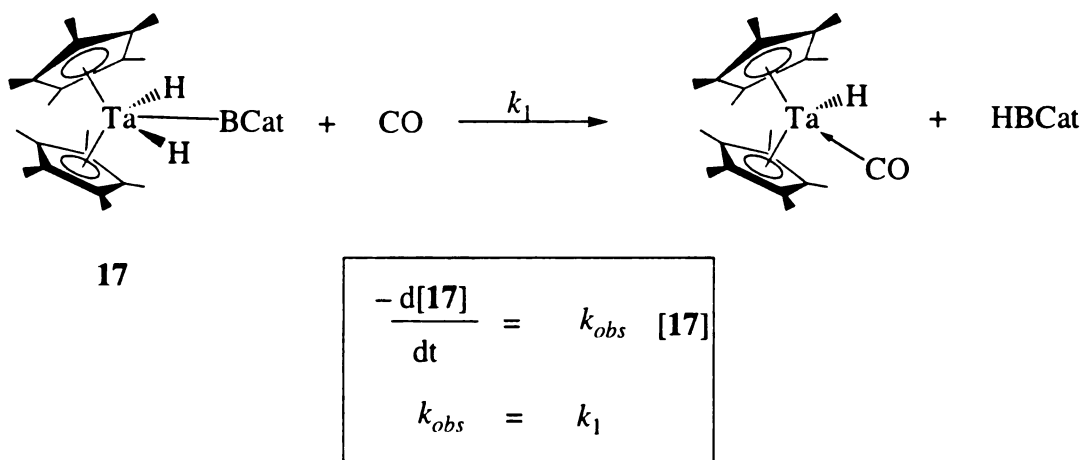
Figure 61. Mechanism and rate law of **17** plus CO.

For the reaction of **17** with CO, k_1 is k_{obs} (Figure 61). The reaction was monitored over a range of temperatures to determine the activation parameters, $\Delta H^{\ddagger}$ and $\Delta S^{\ddagger}$. The Eyring plot in Figure 62 resulted in $\Delta H^{\ddagger} = 23.7(5)$ kcal/mol and $\Delta S^{\ddagger} = -10(1)$ e.u. for the

70

reductive elimination reaction. The value for $\Delta S^{\ddagger}$ does not support a dissociative step, and is typical for reductive elimination via a three–centered transition state.[131,132]
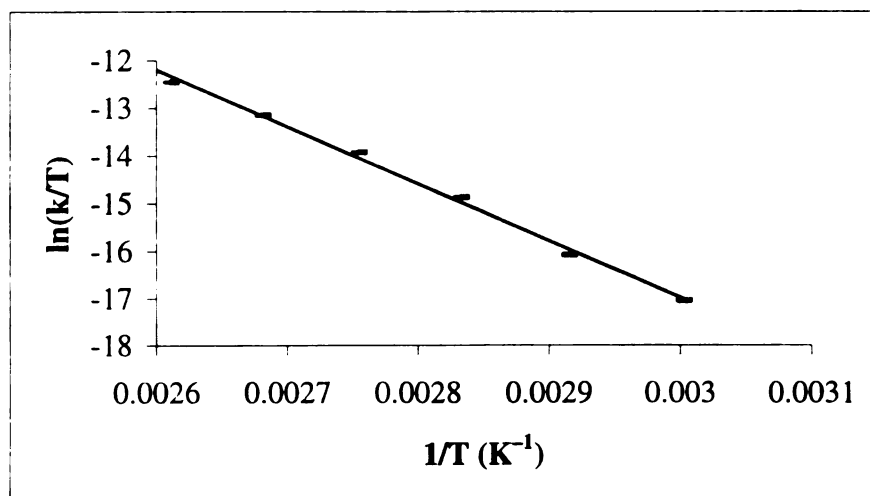
Figure 62. Eyring plot for the reaction of **17** plus CO.
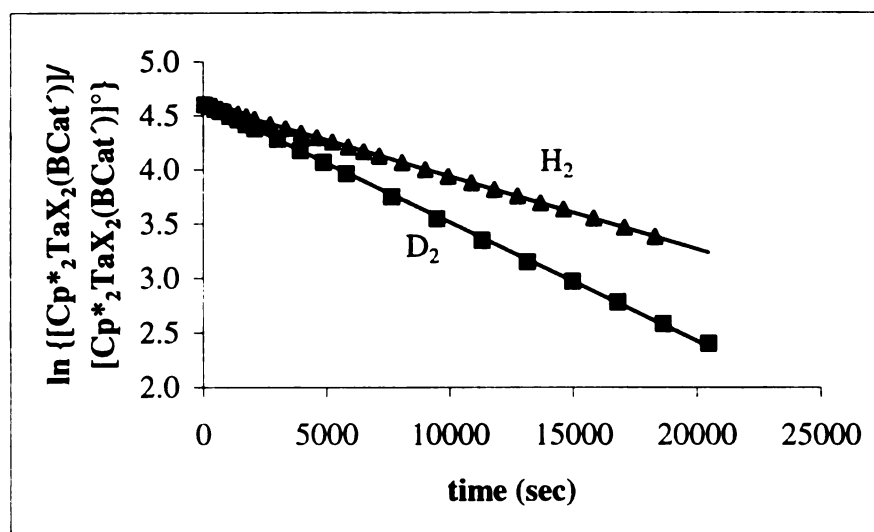
Figure 63. Plot of **17**–$d_{0.2}$ plus CO.

Deuterium Isotope Effect

The failure to observe borane or CO dependence was surprising; however, rate–limiting, irreversible borane elimination could account for the observed kinetic behavior. To determine whether B–H elimination follows the rate limiting step, the isotope effect in

71

the reaction between **17**–d_2 and CO was examined. Isotopically pure **17** can be synthesized by the reaction of **16** with DBCat′ yielding **17**–d_2 with deuterium incorporation only in the hydride positions. Observation of an isotope effect could lend support to a mechanism where B–H bond formation occurs during (or prior to) the rate–limiting step.

Figure 63 clearly shows rate acceleration upon deuterium substitution in the hydride positions. In fact, k_H/k_D = 0.44(9) for **17** is substantially smaller than that observed for **4** (see above). Unlike the results seen for deuterium incorporation in **4**, there are only normal isotopic perturbations of resonance for partially deuterated **17** which argue against a rapid preequilibration dissociation.

Mechanism Determination

The simplest mechanism that is consistent with the kinetic data is shown in pathway A of Figure 64. This mechanism describes simple B–H reductive elimination from the tantalum metal center forming a Ta^{III} intermediate that is subsequently trapped by CO. Figure 64 also offers alternate pathways that can account for the observed kinetic data. Pathway B incorporates a preequilibrium step between **17** and a borane adduct similar to the niobium compound. The rate limiting step could be either the formation of the σ–complex, or borane elimination from the σ–complex to generate borane and the intermediate hydride, $Cp*_2TaH$. It is attractive to hypothesize that the forward step in the equilibrium between **17** and the σ–complex is rate limiting, as elimination from $Cp*_2M^{III}(H_2BCat′)$ σ–complexes should proceed at similar rates. It is worth mentioning that k_H/k_D = 0.44(9) is slightly smaller than values measured for related methane eliminations from $Cp′_2WH(CH_3)$ species.[133,134] While the magnitude of k_H/k_D is small for a kinetic isotope effect, it is similar to equilibrium isotope effects observed by Bercaw for preequilibrium between $Cp*_2TaH(\eta^2\text{–}CH_2O)$ and $Cp*_2TaOCH_3$,[118] and by Feher and Jones in benzene reductive elimination from $Cp*Rh(PMe_3)(H)(Ph)$.[135] Pathway C invokes $\eta^5\rightarrow\eta^3$ ring–slip and subsequent CO coordination, followed by irreversible

borane elimination and $\eta^3 \rightarrow \eta^5$ coordination.[136-139] In pathway D, hydride migration to a Cp* ring carbon precedes CO coordination. Irreversible borane elimination is then followed by hydride migration to Ta. Observation of a primary kinetic isotope effect almost certainly would require borane elimination as rate limiting. For this mechanism, primary isotope effects might be expected for the hydride to pentamethylcyclopentadienyl migration and/or the B–H reductive elimination. If CO coordination precedes the rate limiting step, CO dependence would be expected; however, the absence of an inverse dependence on borane could prevent entering a regime that is first order in [CO].
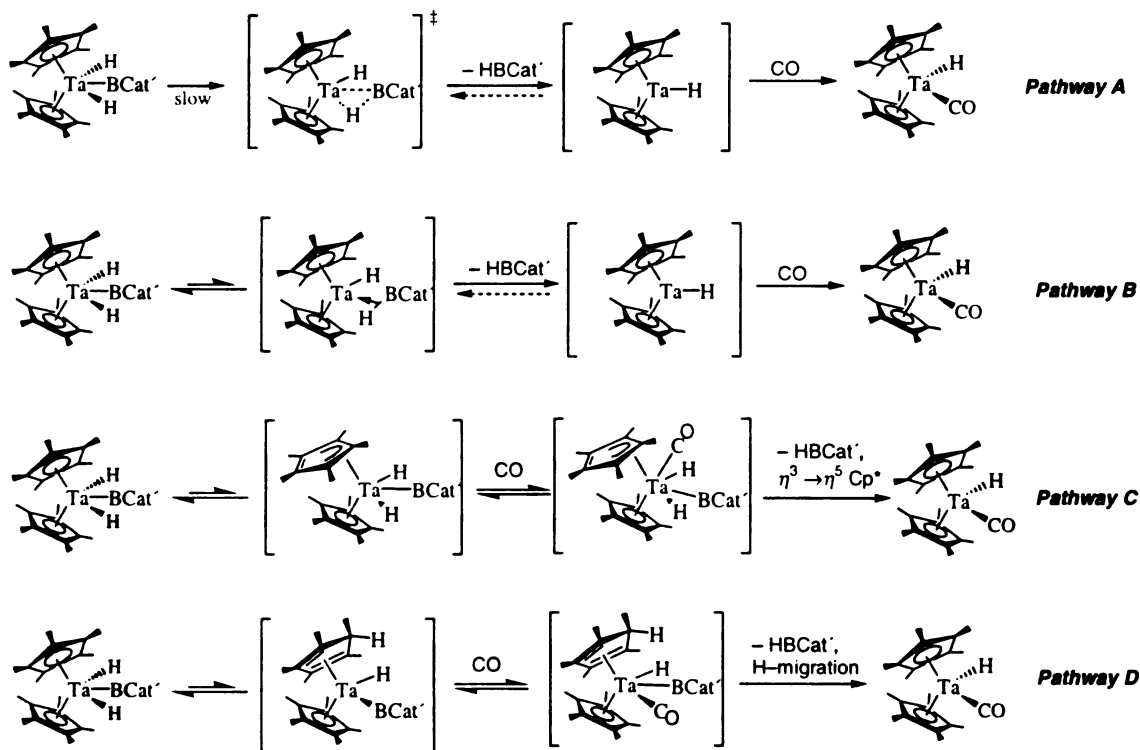
Figure 64. Possible pathways for compound **32** formation.

Distinction between pathways A and B cannot be made definitively from the experimental data. The activation parameters support pathway A as the value for $\Delta S^{\ddagger}$ is consistent with an ordered transition state. This would appear to argue against pathway B since $\Delta S^{\ddagger} = 8(2)$ e.u. for the related dissociative reactions for **4**; however, ordering from

the preequilibrium between **17** and a σ–borane complex could mask dissociative contributions to $\Delta S^{\ddagger}$. In pathway B, the equilibrium between **17** and the borane adduct complex would be rate limiting if borane elimination from $Cp^*_2M^{III}(H_2BCat')$ adduct complexes proceed at similar rates.

For Pathways C and D, application of the steady–state approximation to the concentrations for the intermediates gives identical rate laws that predict saturation behavior in [CO].[140] At low CO pressure, there is no indication of a dependence on [CO] as predicted for these mechanisms. It is conceivable that if CO coordination is sufficiently rapid that there is no regime where a [CO] dependence can be observed. Hence, these mechanisms cannot be rigorously excluded; however, the comparison to H_2 elimination from $Cp^*_2TaH_3$ (**33**) make these pathways unlikely (deuterium should have a similar inverse isotope effect, see below).

Comparison Between B–H and H₂ Eliminations

Compound **33** was synthesized in order to investigate the differences in B–H and H–H elimination from **17** and **33**, respectively. This compound was chosen as direct structural analog to the tantalum boryl complex in terms of placement of the ligands within the metallocene wedge and oxidation state of the metal. In both instances, the metal must undergo a formal reduction from Ta^V to Ta^{III}. In terms of oxidation states, these reactions can be directly compared unlike the reaction of **4** with CO since the niobium metal formally does not undergo a reduction in oxidation state. The effect of the boron fragment bound directly to the metal can therefore be addressed for the tantalum compounds.

The reaction of **33** with CO proceeds cleanly yielding **32** and hydrogen gas. The reaction was monitored over a range of temperatures to determine activation parameters. An Eyring plot was constructed (Figure 65) from the rate constants of individual kinetic experiments yielding $\Delta H^{\ddagger} = 27.2(9)$ kcal/mol and $\Delta S^{\ddagger} = -11(2)$ e.u. The value for $\Delta S^{\ddagger}$ obtained for this reaction is identical, within experimental error, to the value of $\Delta S^{\ddagger}$

74

obtained for the reaction of **17** plus CO that could indicate a similar reductive elimination

pathway.
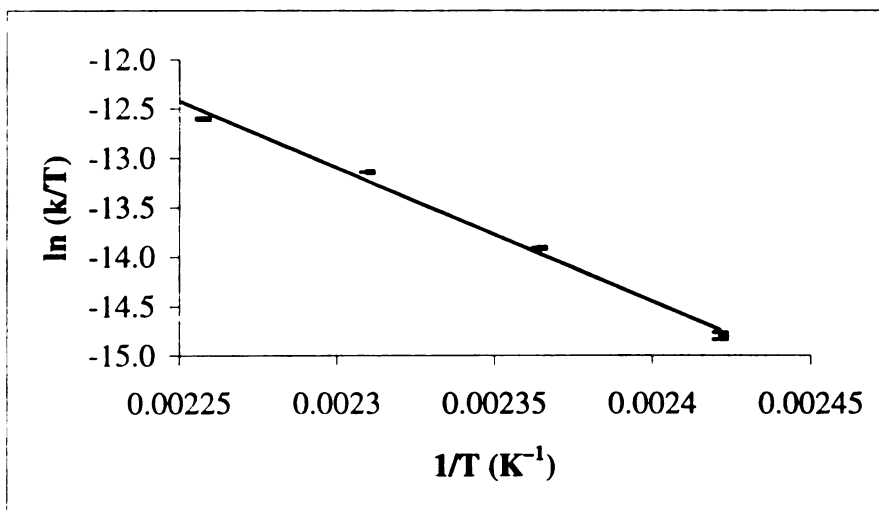
Figure 65. Eyring plot for the reaction of **33** plus CO.
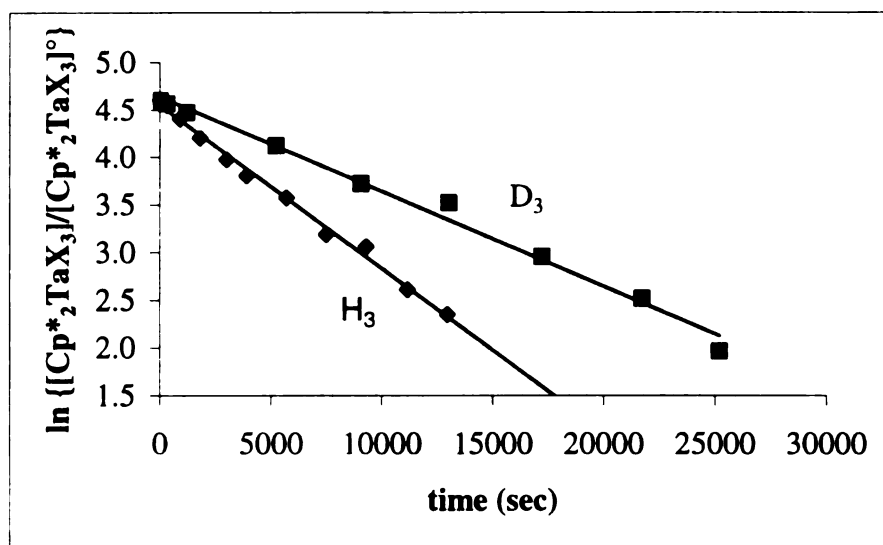
Figure 66. Plot of **33**–$d_{0,3}$ plus CO.

In contrast to the reaction of **17** plus CO, an inverse isotope effect was not observed for the reaction of **33** plus CO. The reaction clearly proceeds at a faster rate with **33** than with **33**–d_3 (Figure 66) with a calculated k_H/k_D = 1.67(6) for this reaction. Although the end product for the metal is identical as the reaction with **17**, the normal

isotope effect witnessed for **33** precludes preequilibrium formation of [Cp*$_2$TaD] and D$_2$. Calculations might provide useful insight concerning intermediates involved in the eliminations of B–H and H–H from **17** and **33**, respectively.

Thermodynamic and Kinetic Data

The kinetic data allow for construction of partial energy level diagrams in Figure 67, Figure 68 and Figure 69. For niobium, neither the relative barriers for H$_2$ and HBCat′ activation by a common intermediate, nor the barrier for H$_2$ elimination from Cp*$_2$NbH$_3$ has been determined. The equilibria measurements between **4** + H$_2$ and Cp*$_2$NbH$_3$ + HBCat′, which will allow determination of the relative free energy difference between **4** and Cp*$_2$NbH$_3$, are currently under investigation.
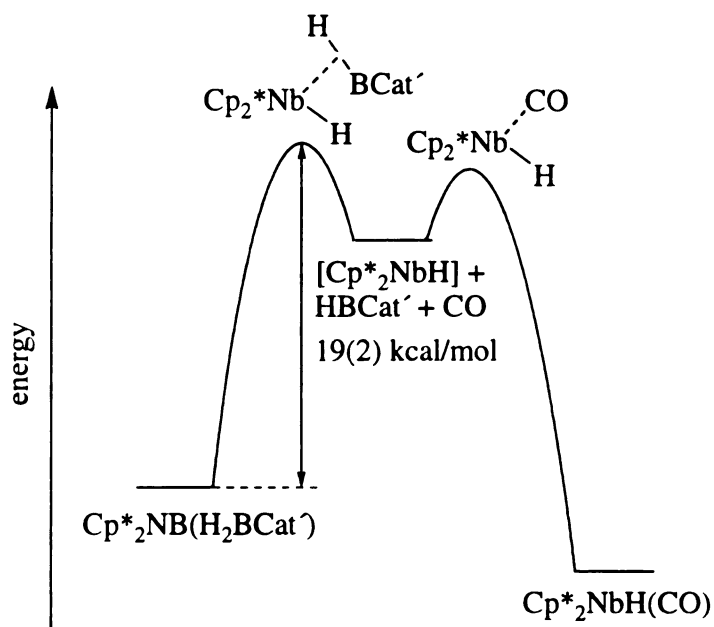
Figure 67. Free energy diagram for **4** plus CO at 20 °C.

The reactive intermediate, [Cp*$_2$TaH], for the reactions of **17** with CO (Figure 68) and **33** with CO (Figure 69) is identical, which allows for calculation of BDE values for reactions up to the common intermediate by using the bond dissociation energy (BDE) for H$_2$ (104.2 kcal/mol)[141] and a calculated BDE for HBCat (111.3 kcal/mol)[142]. For the reaction depicted in Figure 69, an H–H bond is formed while two Ta–H bonds are

76

broken. $\Delta H^{\ddagger}$ is the energy of the bonds formed subtracted from the energy of the bonds broken. In this case, $\Delta H^{\ddagger} \geq 2$ BDE(Ta–H) – BDE(H–H). The maximum value for the BDE(Ta–H) is calculated to be 65.7 kcal/mol from using the appropriate values since the value for $\Delta H^{\ddagger}$ is to the barrier of the energy level diagram not to the intermediates energy position.

For the reaction depicted in Figure 68, an B–H bond is formed while a Ta–H and a Ta–B bond are broken. For this reaction, $\Delta H^{\ddagger} \leq$ BDE(Ta–B) + BDE(Ta–H) – BDE(B–H) for the maximum value of the BDE(Ta–H). From the appropriate BDE values listed above along with the newly calculated BDE(Ta–H), the minimum value for the BDE(Ta–B) is calculate to be 69.3 kcal/mol. The BDE's for Ta–B and Ta–H bonds are related as follows: BDE(Ta–B) $\geq$ BDE(Ta–H) + 3.6 kcal/mol. Also from this relationship, the BDE(Ta–B) can be bracketed by 69.3 kcal/mol $\leq$ BDE(Ta–B) $\leq$ 135.0 kcal/mol should the BDE(Ta–H) value be 0 kcal/mol. The equilibria measurements between **17** + H_2 and **33** + HBCat´, which will allow determination of the relative free energy difference between **17** and **33**, are currently under investigation.
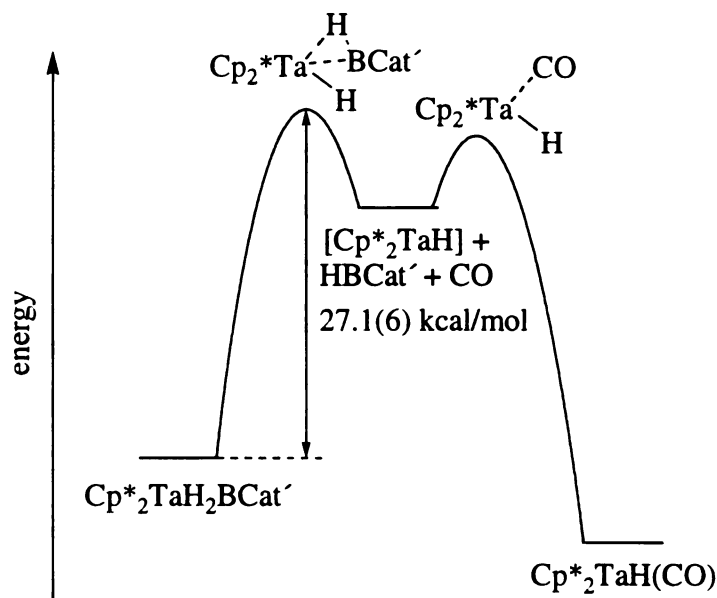
Figure 68. Free energy diagram for **17** plus CO at 70 °C.
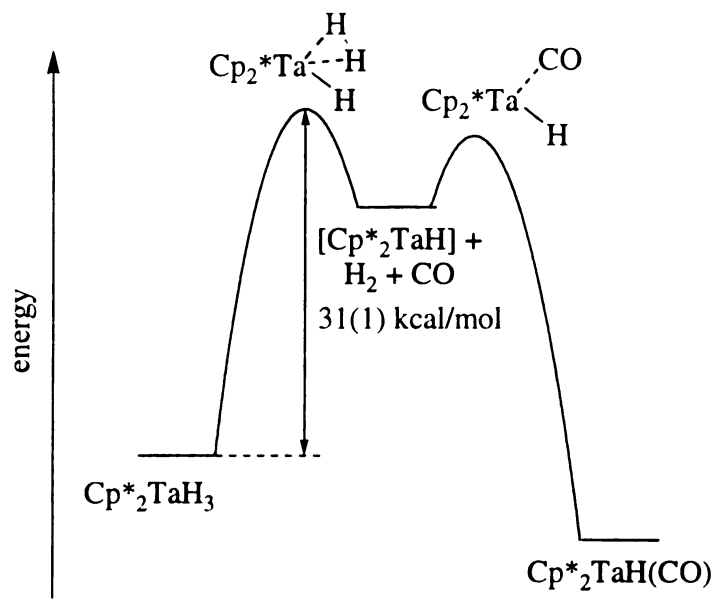
Figure 69. Free energy diagram for **33** plus CO at 70 °C.

CHAPTER 4

EXPERIMENTAL

General Considerations

All manipulations were performed using glove box, Schlenk and vacuum–line techniques. Pentane, heptane, THF, hexanes and toluene were predried over sodium. Toluene was distilled from NaK/benzophenone ketyl. All other solvents were distilled from sodium/benzophenone ketyl. Acetone was dried over activated 3 Å molecular sieves and distilled prior to use. Benzene–d_6 and toluene–d_8 were dried over activated 3 Å molecular sieves and then vacuum transferred into a sodium mirrored container. THF–d_8 was dried over activated 3 Å molecular sieves and vacuum transferred prior to use. Argon and nitrogen gases were purified by passage over MnO on silica.

Ethylene (Matheson) and propylene (Matheson) were subjected to several freeze–pump–thaw cycles and then transferred in vacuo to reaction vessels. Carbon monoxide (Matheson) and dihydrogen (AGA Gas Inc.) were used as received. Diborane gas was synthesized by the following method: $NaBH_4$ (Aldrich) was placed in an air free container, slurried with distilled dimethoxyethane (DME, Aldrich) and frozen with liquid N_2. Distilled $BF_3 \cdot Et_2O$ (Mallinckrodt) was then added to the frozen slurry. The contents of the air free container were then evacuated. The system was allowed to slowly warm to room temperature in the process generating B_2H_6.

Catecholborane (Aldrich) was vacuum transferred prior to use. Preparation of DBCat was accomplished by reaction $NaBD_4$ (Aldrich) and $BF_3 \cdot Et_2O$ (Mallinckrodt) to produce BD_3 which was then bubbled through a THF solution of catechol (Aldrich). The THF was then distilled from the solution at atmospheric pressure and the remaining solution was vacuum distilled to give the borane as a clear, viscous liquid. $\{Cp_2TaH_2Li\}_x,$[42] **27**,[143] $Cp_2NbH(\eta^2-CH_2=CH_2),$[144] **19**,[93] **3**,[120] **13**[114] and **16**[68] were all

prepared by literature methods. *Exo* and *endo*–**27** were prepared by irradiating pure *endo*–**27** with 300 nm light for 4 h under an atmosphere of propylene gas generating 41% *exo*–**27** and 59% *endo*–**27**.

^{1}H NMR spectra were recorded on Varian Gemini–300 (300.0 MHz), Varian VXR–300 (299.9 MHz), and Varian VXR–500 (499.9 MHz) spectrometers and referenced to residual proton solvent signals. ^{2}H NMR spectra were recorded on a Varian VXR–300 spectrometer operating at 46 MHz or on a Varian VXR–500 MHz spectrometer operating at 77 MHz; and spectra were referenced to residual deuterium signals of the solvent. ^{11}B NMR spectra were recorded using a Varian VXR–300 spectrometer operating at 96 MHz or on a Varian VXR–500 MHz spectrometer operating at 160 MHz; and spectra were referenced to a $BF_3 \cdot Et_2O$ external standard. Infrared spectra were recorded as Nujol mulls in KBr plates using a Nicolet IR/42 spectrometer. GC samples were run on a Hewlett Packard 5890A gas chromatograph equipped with a Hewlett Packard 3392 integrator and a Foxboro GB–1 capillary column (25 m x 0.25 mm I.D. with a 0.25 μm film). Elemental Analyses were performed by Desert Analytics, Tucson, Arizona or in house on the MSU department of chemistry elemental analyzer.

Synthesis

exo and *endo*–$Cp_2TaH_2(BO_2C_6H_4)$ (*exo* and *endo*–**1**). A 10 mL toluene solution of β–chloro–catecholborane (418 mg, 1.31 mmol) was added dropwise to a vigorously stirred toluene suspension (25 mL) of $\{Cp_2TaH_2Li\}_x$ (202 mg, 1.31 mmol) at –78 °C. The mixture was gradually warmed and stirred for 30 min at room temperature during which time the orange solids were replaced with an off–white precipitate (LiCl) accompanied by the formation of a pale amber solution. The solvent from the filtrate was stripped and the crude product (321 mg, 57%) was analyzed by ^{1}H NMR where integration revealed a 32:68 mixture of isomers. The isomers were separated by fractional crystallization from toluene. *endo*–$Cp_2TaH_2(BCat)$ was isolated as pale yellow microcrystals (80 mg, 19%) as the less soluble isomer. Concentration of the mother liquor and further cooling afforded

80

exo–Cp$_2$TaH$_2$(BCat) as pale microcrystals (132 mg, 23%). *endo*–Cp$_2$TaH$_2$(BCat): ^{1}H

NMR (C$_6$D$_6$) δ 7.14 (m, 2 H, O$_2$C$_6$*H$_4$*), 6.82 (m, 2 H, O$_2$C$_6$*H$_4$*), 4.85 (s, 10 H, C$_5$*H$_5$*), –

4.24 (s, 2 H, Ta*H$_2$*); ^{11}B NMR (C$_6$D$_6$) δ 70 (Δ v$_{1/2}$ = 250 Hz); IR (cm^{-1}) 1768 (v$_{TaH}$) (1278

(v$_{TaD}$)); Anal. calcd for C$_{14.2}$H$_{20.8}$BO$_2$Ta: C, 49.8; H, 4.27. Found: C, 49.6; H, 4.17. *exo*–

Cp$_2$TaH$_2$(BCat): δ 7.11 (m, 2H, O$_2$C$_6$*H$_4$*), 6.84 (m, 2 H, O$_2$C$_6$*H$_4$*), 4.83 (s, 10 H, C$_5$*H$_5$*), –

4.20 (d, *J* = 5.5 Hz, 1 H, Ta*H$_2$*); –5.17 (s, 1 H, Ta*H$_2$*); ^{11}B NMR (C$_6$D$_6$) δ 65 (Δ v$_{1/2}$ = 190

Hz); IR (cm^{-1}) 1771, 1703 ((v$_{TaH}$) 1283 (v$_{TaD}$)). **endo–1–*d$_2$*** and **exo–1–*d$_2$*** were similarly

prepared from {Cp$_2$TaD$_2$Li}$_x$.

endo–Cp$_2$TaH$_2$(BO$_2$C$_6$H$_4$) (endo–1). HBCat (805 mg, 6.76 mmol) was dissolved

in 10 mL toluene and then added via cannula to a 100 mL toluene solution of **27** (950 mg,

2.70 mmol). The solution was stirred for two h during which time the color gradually

darkened to a dark yellow color. The solvent was then placed overnight in a –15 °C

freezer. The solvent was removed by filtration and the yellow microcrystals dried under

vacuum (915 mg, 78%): mp 141–143 °C (dec); ^{1}H NMR (C$_6$D$_6$) δ 7.15 (m, 2 H, O$_2$C$_6$*H$_4$*),

6.83 (m, 2 H, O$_2$C$_6$*H$_4$*), 4.85 (s, 10 H, C$_5$*H$_5$*), –4.23 (s, 2 H, Ta*H*); ^{11}B NMR (C$_6$D$_6$) δ 70

(Δ v$_{1/2}$ = 250 Hz); IR (cm^{-1}) 1751 (v$_{TaH}$).

endo–Cp*$_2$Nb(H$_2$BO$_2$C$_6$H$_4$). A 15 mL toluene solution of **3** (219 mg, 0.540

mmol) was cooled to –78 °C. HBCat (0.161 mL, 1.35 mmol) was added to this stirred

solution via syringe. The resulting solution was warmed to room temperature and stirred

for two h. During the course of the reaction, the color of the solution gradually lightened

from deep red to orange–red, and solvent evaporation gave a deep orange solid. The

reaction mixture was dissolved in a minimal volume of toluene and cooled to –80 °C.

The product was isolated as orange microcrystals (207 mg, 79%): mp 171–173 °C; ^{1}H

NMR (C$_6$D$_6$) δ 7.07 (m, 2 H, O$_2$C$_6$*H$_4$*), 6.85 (m, 2 H, O$_2$C$_6$*H$_4$*), 1.83 (s, 30 H, C$_5$(C*H$_3$*)$_5$),

–8.27 (br, 2 H, Nb*H$_2$*); ^{11}B NMR (C$_6$D$_6$) δ 60 (Δ v$_{1/2}$ = 240 Hz); IR (cm^{-1}) 1653 (v$_{NbH}$);

Anal. calcd for C$_{26}$H$_{36}$BNbO$_2$: C, 64.5; H, 7.44. Found: C, 64.1; H, 7.26.

endo-Cp*$_2$Nb(H$_2$BO$_2$C$_6$H$_3$–4–^{t}Bu) (*endo*–4). A 20 mL toluene solution of 3 (400 mg, 0.985 mmol) was cooled to –78 °C. HBO$_2$C$_6$H$_3$–4–^{t}Bu (0.360 mL, 2.07 mmol) was then added via syringe to the stirred solution, and the solution was warmed to room temperature. After two h, the toluene was removed in vacuo, leaving a viscous red oil. The oil was dissolved in a minimal volume of heptane and placed in a –80 °C freezer. Upon standing overnight, deep red microcrystals were deposited. After the filtrate was removed, the crystals were washed with cold pentane and dried in vacuo (396 mg, 75%): mp 154–157 °C; ^{1}H NMR (C$_6$D$_6$) δ 7.30 (d, J = 2.1 Hz, 1 H, O$_2$C$_6$$H_3$), 7.04 (d, J = 8.1 Hz, 1 H, O$_2$C$_6$$H_3$), 6.90 (dd, J = 7.8, 1.95 Hz, 1 H, O$_2$C$_6$$H_3$), 1.85 (s, 30 H, C$_5$(C$H_3$)$_5$), 1.30 (s, 9 H, O$_2C_6H_3$(4–C(C$H_3$)$_3$)), –8.19 (br, 2 H, Nb$H_2$); ^{11}B NMR (C$_6D_6$) δ 60 (Δ v$_{1/2}$ = 300 Hz); IR (cm^{-1}) 1653 (v$_{NbH}$). *endo*–4–d_2 was similarly prepared from 3 and DBO$_2$C$_6$H$_3$–4–^{t}Bu: ^{1}H NMR (C$_6$D$_6$) δ 7.28 (d, J = 1.8 Hz, 1 H, O$_2$C$_6$$H_3$), 7.03 (d, J = 8.1 Hz, 1 H, O$_2$C$_6$$H_3$), 6.89 (dd, J = 8.1, 1.95 Hz, 1 H, O$_2$C$_6$$H_3$), 1.83 (s, 30 H, C$_5$(C$H_3$)$_5$), 1.30 (s, 9 H, O$_2C_6H_3$(4–C(C$H_3$)$_3$)); ^{2}H NMR (C$_6H_6$) δ –9.29 (br, Nb$D_2$); ^{11}B NMR (C$_6D_6$) δ 57 (Δ v$_{1/2}$ = 270 Hz).

endo-Cp*$_2$Nb(H$_2$BO$_2$C$_6$H$_3$–3–^{t}Bu) (*endo*–12). A 10 mL toluene solution of 3 (251 mg, 0.618 mmol) was cooled to –78 °C. HBO$_2$C$_6$H$_3$–3–^{t}Bu (229 mg, 1.30 mmol) was dissolved in 5 mL toluene, and the borane solution was transferred to the propylene–hydride complex via cannula. Once the addition was complete, the resulting solution was allowed to warm to room temperature and stir for three h. The toluene was then evaporated, leaving a tacky, deep orange–red solid. The crude mixture was dissolved in a minimal volume of pentane and placed in a –80 °C freezer. Orange–red microcrystals were deposited overnight. The product was collected, washed with pentane, and dried in vacuo (218 mg, 65%): mp 141–142 °C; ^{1}H NMR (C$_6$D$_6$) δ 7.04 (m, 1 H, O$_2$C$_6$$H_3$), 6.96 (m, 1 H, O$_2C_6$$H_3$), 6.91 (m, 1 H, O$_2C_6$$H_3$), 1.86 (s, 30 H, C$_5$(C$H_3$)$_5$), 1.58 (s, 9 H, O$_2C_6H_3$(3–C(C$H_3$)$_3$)), –7.91 (br, 2 H, Nb$H_2$); ^{11}B NMR (C$_6D_6$) δ 61 (Δ v$_{1/2}$ = 280 Hz); IR (cm^{-1}) 1649 (v$_{NbH}$).

endo*–Cp*₂Nb(H₂BO₂(C(CH₃)₂)₂)** (endo*–14).** All manipulations for this reaction were carried out under an Ar atmosphere. Complex **3** (401 mg, 0.988 mmol) was dissolved in 10 mL toluene and cooled in a dry ice/isopropanol bath. HBPin (316 mg, 2.47 mmol) was dissolved in 5 mL toluene. The borane solution was then added via cannula to the stirring propylene–hydride solution. The resulting solution was allowed to warm to room temperature. The volatiles were removed under vacuum after a two h reaction time. The rust–orange solid was dissolved in toluene, concentrated and placed in a –80 °C freezer overnight. The mother liquor was removed by filtration and the rust–orange microcrystalline compound (286 mg, 59%) was dried under vacuum: ^{1}H NMR (C_6D_6) δ 1.88 (s, 30 H, $C_5(CH_3)_5$), 1.18 (s, 12 H, $C(CH_3)_2)_2$), –9.24 (br, 2 H, NbH_2); ^{11}B NMR (C_6D_6) δ 54 (Δ $v_{1/2}$ = 200 Hz).

(Cp*₂NbH)₂–μ–N₂ (15). A 20 mL toluene solution of **3** (775 mg, 1.91mmol) was cooled to –78 °C. HBPin (536 mg, 4.19 mmol) was dissolved in 10 mL toluene. The HBPin solution was then added via cannula to the cooled propylene–hydride complex solution. The stirring solution was allowed to warm to room temperature. After stirring for 2.5 h at room temperature, the volatiles were removed under vacuum. The resulting solid was dissolved in pentane, concentrated and placed in a –80 °C freezer. After 16 h, the mother liquor was removed by filtration and the deep red microcrystalline solid was washed once with cold pentane (–78 °C) and vacuum dried (357 mg, 49%): mp 128–130 °C (dec); ^{1}H NMR (C_6D_6) δ 1.99 (s, 30 H, $C_5(CH_3)_5$), 1.94 (s, 30 H, $C_5(CH_3)_5$), –2.68 (br, 2 H, NbH); Anal. calcd for $C_{40}H_{62}N_2Nb_2$: C, 63.5; H, 8.2, N, 3.7. Found: C, 63.5; H, 8.6, N, 4.0.

***endo*–Cp*₂TaH₂(BO₂C₆H₄).** Catecholborane (0,120 mL, 0.973 mmol) was added to a 10 mL toluene solution of **16** (193 mg, 0.389 mmol) at room temperature. The solution was then stirred for two h during which time the initial pale yellow color gradually turned to a lime green color. Evaporation of the toluene yielded a lime green solid. Washing this solid with pentane followed by drying under vacuum yielded a pale

yellow solid (160 mg, 72%): mp 159–162 °C (dec); ^{1}H NMR (C$_6$D$_6$) δ 7.19 (m, 2 H, O$_2$C$_6$$H_4$), 6.89 (m, 2 H, O$_2C_6$$H_4$), 1.96 (s, 30 H, C$_5$(C$H_3$)$_5$), –2.12 (br, 2 H, Ta$H_2$); ^{11}B NMR (C$_6D_6$) δ 74 (Δ v$_{1/2}$ = 390 Hz); IR (cm^{-1}) 1774, 1709 (v$_{NbH}$).

endo–Cp*$_2$TaH$_2$(BO$_2$C$_6$H$_3$–4–^{t}Bu) (**endo–17**). Toluene (5 mL) was used to dissolve **16** (155 mg, 0.313 mmol). HBO$_2$C$_6$H$_3$–4–^{t}Bu (0.140 mL, 0.784 mmol) was then added via syringe to the stirred solution. The resulting solution was stirred for two h at room temperature, giving a rust orange solution. Evaporation of the toluene yielded a viscous, deep orange oil. Dissolving this oil in pentane and concentrating the resulting orange solution yielded pale yellow microcrystals when placed in a –80 °C freezer overnight. Separation of the filtrate and drying the microcrystals under vacuum gave the pure product (112 mg, 57%): mp 156–158 °C; ^{1}H NMR (C$_6$D$_6$) δ 7.42 (d, J = 2.1 Hz, 1 H, O$_2$C$_6$$H_3$), 7.19 (d, J = 11.4 Hz, 1 H, O$_2$C$_6$$H_3$), 6.95 (dd, J = 8.4, 1.95 Hz, 1 H, O$_2$C$_6$$H_3$), 1.98 (s, 30 H, C$_5$(C$H_3$)$_5$), 1.29 (s, 9 H, O$_2C_6H_3$(4–C(C$H_3$)$_3$)), –2.05 (br, 2 H, Ta$H_2$); ^{11}B NMR (C$_6D_6$) δ 73 (Δ v$_{1/2}$ = 610 Hz); IR (cm^{-1}) 1767, 1720 (v$_{NbH}$); Anal. calcd for C$_{30}$H$_{44}$BO$_2$Ta: C, 57.4; H, 7.01. Found: C, 57.6; H, 7.29. **endo–17–d_2** was similarly prepared from **16** and DBO$_2$C$_6$H$_3$–4–^{t}Bu: ^{1}H NMR (C$_6$D$_6$) δ 7.41 (d, J = 1.8 Hz, 1 H, O$_2$C$_6$$H_3$), 7.18 (d, J = 8.1 Hz, 1 H, O$_2$C$_6$$H_3$), 6.95 (dd, J = 8.1, 1.8 Hz, 1 H, O$_2$C$_6$$H_3$), 1.97 (s, 30 H, C$_5$(C$H_3$)$_5$), 1.29 (s, 9 H, O$_2C_6H_3$(4–C(C$H_3$)$_3$)); ^{2}H NMR (C$_6H_6$) δ –2.02 (br, Ta$D_2$); ^{11}B NMR (C$_6D_6$) δ 72 (Δ v$_{1/2}$ = 660 Hz). **endo–17–d_0–d_2** was prepared as a mixture of isotopomers by adding equal volumes HBO$_2$C$_6$H$_3$–4–^{t}Bu and DBO$_2$C$_6$H$_3$–4–^{t}Bu of to a toluene solution of **16**. The work up was analogous to that described above: ^{1}H NMR (C$_6$D$_6$) δ 7.41 (m, 1 H, O$_2$C$_6$$H_3$), 7.17 (m, 1 H, O$_2C_6$$H_3$), 6.82 (m, 1 H, O$_2C_6$$H_3$), 1.98 (s, 30 H, C$_5$(C$H_3$)$_5$), 1.29 (s, 9 H, O$_2C_6H_3$(3–C(C$H_3$)$_3$)), –2.06 (br, 2 H, Ta$H$D); ^{2}H NMR (C$_6H_6$) δ –2.02 (br, TaH$D$); ^{11}B NMR (C$_6D_6$) δ 70 (Δ v$_{1/2}$ = 650 Hz).

Cp$_2$NbH(BO$_2$C$_6$H$_4$)$_2$ (18). A 10 mL toluene solution of Cp$_2$NbH(η^2–CH$_2$=CH$_2$) (274 mg, 1.09 mmol) was added to catecholborane (522 mg, 4.36 mmol). The resulting solution was stirred overnight at room temperature. The color gradually changed to a

orange–red and during the course of the reaction a yellow solid precipitated out of solution. The solids were then allowed to settle and the filtrate was removed via cannula. The solids were then washed with cold toluene. The product was isolated as yellow microcrystals (137 mg, 27%): mp 178–181 °C (dec); ^{1}H NMR (C_6D_6) δ 7.00 (m, 2 H, $O_2C_6H_4$), 6.93 (m, 2 H, $O_2C_6H_4$), 6.63 (m, 2 H, $O_2C_6H_4$), 6.57 (m, 2 H, $O_2C_6H_4$), 5.11 (s, 10 H, C_5H_5), –7.71 (br, 1 H, NbH); ^{1}H NMR (THF–d_8) δ 6.89 (m, 2 H, $O_2C_6H_4$), 6.82 (m, 2 H, $O_2C_6H_4$), 6.69 (m, 2 H, $O_2C_6H_4$), 6.66 (m, 2 H, $O_2C_6H_4$), 5.59 (s, 10 H, C_5H_5), –7.81 (br, 1 H, NbH); ^{11}B NMR (C_6D_6) δ 64 (Δ $v_{1/2}$ = 800 Hz), δ 60 (Δ $v_{1/2}$ = 310 Hz); IR (cm^{-1}) 1651 (v_{NbH}). **18–d** was similarly prepared from $Cp_2NbH(\eta^2$–CH_2=CH_2) and catecholborane–d_1: ^{1}H NMR (THF–d_8) δ 6.85 (m, 2 H, $O_2C_6H_4$), 6.77 (m, 2 H, $O_2C_6H_4$), 6.66 (m, 2 H, $O_2C_6H_4$), 6.62 (m, 2 H, $O_2C_6H_4$), 5.55 (s, 10 H, C_5H_3), ^{2}H NMR (THF) –7.98 (br, NbD); ^{11}B NMR (THF–d_8) δ 645 (Δ $v_{1/2}$ = 880 Hz), δ 60 (Δ $v_{1/2}$ = 270 Hz).

Phenethyl Alcohol Formation. Complex **3** (15.3 mg, 0.038 mmol) was dissolved in 0.6 mL benzene–d_6 along with styrene (63.1 mg, 0.607 mmol) and $HBO_2C_6H_3$–4–^{t}Bu (106 mg, 0.602 mmol). The solution was placed in an NMR tube and flame sealed. The tube was then maintained at 75 °C for four d in a constant temperature oil bath. Conversion of free borane to the alkyl borane product was monitored by ^{1}H NMR. Integration revealed 64% hydroboration products along with 11% of a boron decomposition product[35,36] and 25% unreacted borane. The contents were then converted to the corresponding alcohol by literature method.[145] The products of the oxidative workup were analyzed by gas chromatography with phenethyl alcohol and sec–phenethyl alcohol detected in a 3.72:1 ratio.

NMR Tube Reactions

3 + cis–cyclooctene + $HBO_2C_6H_3$–4–^{t}Bu. Complex **3** (11.8 mg, 0.029 mmol) was dissolved in 0.6 mL benzene–d_6 with cis–cyclooctene (3.2 mg, 0.029 mmol) and HBCat´ (4.4 mg, 0.025 mmol). The resulting solution was transferred to a NMR tube

which was flame sealed. The was kept at room temperature for 2.5 h. A ^{1}H NMR spectrum showed primary hydroboration occurred with the bound propylene fragment on the niobium complex with some hydroboration of the *cis*–cyclooctene. Integration of the appropriate ^{t}Bu resonances established the ratio of *cis*–cyclooctene:propylene hydroboration as 1:5.08. The tube was held at room temperature overnight and integration of another ^{1}H NMR spectrum determined the ratio of *cis*–cyclooctene:propylene hydroboration to be 1:3.81.

3 + *cis*–cyclooctene + propylene + HBO$_2$C$_6$H$_3$–4–^{t}Bu. Complex **3** (9.8 mg, 0.029 mmol) was dissolved in 0.6 mL benzene–d_6. HBCat' (51.0 mg, 0.290 mmol) and *cis*–cyclooctene (16.0 mg, 0.145 mmol) were added to the solution which was then placed in a NMR tube. The was then frozen with liquid nitrogen and evacuated. Propylene (0.145 mmol) was then admitted with the aid of a calibrated volume vessel. The NMR tube was then flame sealed and the contents of the tube heated at 60 °C for three d. The rate of hydroboration for propylene was faster than that of *cis*–cyclooctene based on integrated ^{1}H spectra (propylene:*cis*–cyclooctene = 4.53:1). Repeating the reaction without the use of the niobium complex required heating the reaction at 120 °C for three d and resulted in nearly identical rates of hydroboration; however, the rate for *cis*–cyclooctene was slightly faster (propylene:*cis*–cyclooctene = 0.93:1).

Cp*$_2$Nb(H$_2$BO$_2$C$_6$H$_4$) + CO. A 10 mg (0.210 mmol) sample of Cp*$_2$Nb(H$_2$BO$_2$C$_6$H$_4$) was dissolved in 0.8 mL benzene–d_6. This solution was placed in an NMR tube and frozen with liquid nitrogen. The NMR tube was evacuated and one atm of CO gas admitted. The tube was then flame sealed and allowed to warm to room temperature. ^{1}H and ^{11}B NMR spectra indicated elimination of HBCat, and **26** was the only Nb–containing product detected. Integration of the ^{11}B spectrum indicated 91% catecholborane (δ 29, d, J_{HB} = 180 Hz) and 9% of a B$_2$Cat$_3$ (δ 23, s).

Cp*$_2$Nb(H$_2$BO$_2$C$_6$H$_4$) + B$_2$H$_6$. A 15 mg (0.031 mmol) sample of the niobium complex was dissolved in 0.6 mL toluene–d_8 and placed in a NMR. The solution was

frozen with liquid nitrogen and then evacuated. Diborane generation was performed in the following way: A Schlenk tube was charged with $NaBD_4$ (130 mg, 3.43 mmol) and DME (0.875 mL). This slurry was cooled in a liquid nitrogen bath, and $BF_3 \cdot Et_2O$ (0.580 mL, 3.52 mmol) was added under a counter flow of N_2 gas. The Schlenk tube was fitted with an adapter and the assembly was attached to a high vacuum manifold. After the reaction vessel had been evacuated, the suspension was allowed to slowly warm to room temperature with generation of B_2H_6. From a calibrated bulb, approximately 0.150 mmol of diborane was condensed into a NMR tube. Once the addition of diborane was completed, the NMR tube was flame sealed. ^1H and ^{11}B NMR spectra were initially taken at -5 °C, with the temperature gradually raised to 20 °C over the course of three h. The reaction cleanly formed **13** and catecholborane, with ^{11}B spectra indicating 92% catecholborane (δ 28, d, J_{HB} = 190 Hz) and 8% of a boron decomposition product (δ 22, s).

4 + C₂H₄. A 15 mg (0.031 mmol) sample of the niobium complex was dissolved in 0.6 mL toluene–d_8 and placed in a NMR. This tube was then frozen with liquid nitrogen and evacuated. Ethylene (one atm) was then admitted to the frozen contents of the NMR tube, which was then flame sealed. ^1H and ^{11}B spectra were initially taken at 10 °C and increased to 40 °C over the course of the three h reaction time. The products of the reaction were $Cp*_2NbH(\eta^2\text{–}CH_2=CH_2)$ and free borane. Integration of the final ^{11}B spectrum showed 18% $EtBO_2C_6H_3\text{–}4\text{–}^tBu$ (δ 36, s), 74% of free borane (δ 29, d, J_{HB} = 190 Hz) and 8% of a boron decomposition product (δ 23, s).

4 + C₃H₆. A 15 mg (0.028 mmol) sample of **4** was dissolved in 0.6 mL toluene–d_8. This solution was placed in a NMR tube and frozen with liquid nitrogen, followed by evacuation of the gases. Approximately one atmosphere of propylene was then admitted to the frozen contents of the NMR tube, after which it was flame sealed. Initial ^1H and ^{11}B NMR spectra (taken at 0 °C) showed the formation of **3** and free borane. However, as the reaction proceeded the concentration of the free borane diminished and the

concentration of *n*-propylborane increased. After the three h reaction time, during which the temperature had been gradually raised to 40 °C and then lowered to 25 °C, a ^{11}B spectrum indicated clean conversion to *n*-propylborane (93%, δ 36, s) and a boron containing decomposition product (7%, δ 22, s). A final ^{1}H spectrum revealed the presence of **3**.

4 + H$_2$. A benzene–d_6 (0.6 mL) solution of **4** (15.0 mg, 0.028 mmol) was placed in a NMR tube. This solution was frozen using liquid nitrogen. Addition of one atm of H$_2$ gas was preceded by evacuation of the frozen NMR tube. ^{1}H and ^{11}B spectra, initially taken at 20 °C and gradually raised to 50 °C over the four h reaction time, indicated formation of Cp*$_2$NbH$_3$ and free borane. Integration of the final ^{11}B NMR spectrum showed 80% of free borane (δ 28.5, d, J_{HB} = 190 Hz) and 20% of a boron decomposition product, B$_2$Cat$_3$ (δ 22.2, s).

***exo* and *endo*–27 + HBCat.** A 21 mg (0.059 mmol) sample of **27** was dissolved in benzene–d_6 along with HBCat (15 mg, 0.12 mmol). The resulting solution was placed in a NMR tube and flame sealed. An immediate ^{1}H NMR demonstrated that *endo*–**27** is used preferentially at early reaction times with the formation of only one set of alkylborane resonances with predominant formation of *endo*–**1** and slight formation of *exo*–**1**. Only *exo*–**27** remained (44% of the original *exo*–**27** present) upon standing at room temperature for 12 h in the dark. Another ^{1}H NMR spectrum, after the tube was heated at 40 °C for 2.5 h, revealed one set of alkylborane resonances, *endo*–**1** (84%) and *exo*–**1** (16%) with no detection of remaining *exo*–**27**.

***endo*–27 + DBCat.** A 12 mg (0.035 mmol) sample of *endo*–**27** was dissolved in 0.6 mL toluene with 8 mg DBCat (0.07 mmol) and placed in an NMR tube. The resulting solution was allowed to react for several hours at room temperature. A ^{2}H NMR spectrum was recorded. Deuterium incorporation was witnessed only the hydride position of *endo*–**1** and the α–carbon position of *n*–PrBCat. Integration of the ^{2}H NMR spectrum revealed

40% of the deuterium label was located in the alkyl borane and 60% of the label was located in the hydride position of the tantalum boryl complex.

***endo*–27 + DBCat.** Complex **27** (12 mg, 0.034 mmol) was dissolved in 0.6 mL toluene–d_8 along with 8 μL DBCat (0.07 mmol) and placed in an NMR tube. The resulting solution was allowed to react at room temperature for several hours. Integration of the *n*–PrBCat alkyl resonances resulted in the ratio between α, β, and γ protons as 1.5:2:3.

Generation of 20. Complex **19** (20 mg, 0.076 mmol) was dissolved in 0.6 mL toluene–d_8 and placed in a J–Young NMR tube. HBCat (9 μL, 0.08 mmol) was added to the headspace of the NMR tube. The NMR tube was kept horizontal to prevent mixing of the reagents. Upon removal from the glove box, the NMR tube was immediately placed in a dry ice/isopropanol bath. Once the tube had been cooled, the contents of the NMR tube were allowed to mix. The reaction was monitored at –20 °C. ^{1}H NMR (toluene–d_8) δ 7.08 (m, 2H, $O_2C_6H_4$), 6.83 (m, 2H, $O_2C_6H_4$), 4.88 (s, 10H C_5H_5), –4.40 (s, 1H, Nb*H*), – 6.00 (br, 1H, Nb*H*); ^{11}B NMR (toluene–d_8) δ 59 ($\Delta v_{1/2}$ = 490 Hz). A NOESY spectrum revealed a cross peak between the two hydride positions of **20**.

19 + DBCat. A 23 mg (0.085 mmol) sample of **19** was dissolved in 0.6 mL toluene and added to a J–Young NMR tube. DBCat (10 μL, 0.08 mmol) was added to the head space of a J–Young NMR tube which was then capped. The tube was kept horizontal to prevent mixing of the two reagents. Upon removal from the glove box, the tube was immediately cooled in a dry ice/isopropanol bath. The contents of the NMR tube were allowed to react at –20 °C as periodic ^{2}H NMR spectra were recorded. Exclusive deuterium incorporation was observed at the high–field resonance of **20** (^{2}H NMR δ – 6.21) at early reaction times. A gradual mixing of the deuterium label was seen between the two hydride positions of **20** over 12 h at room temperature (^{2}H NMR δ –4.42 and δ – 6.21)

In a separate experiment, **19** (10 mg, 0.039 mmol) was loaded into a J–Young NMR tube. A solution of DBCat (10 mg, 0.078 mmol) in 0.6 ml toluene was then added to the NMR tube. The resulting NMR sample was quickly capped and kept at room temperature for 6 h. A ^{2}H NMR spectrum revealed the formation of **2**–d_{0-2}, **18**–d_{0-1}, propane–d_{0-2} and n–PrBCat–d_{0-2}. The ratio for deuterium incorporation at n–PrBCat, propane and hydride positions was found to be 29:28:43 by integrating ^{2}H NMR spectra (C_7H_8, –20 °C). The isotopic distribution of deuterium between α, β, and γ carbons in n–PrBCat was 57:20:23. For propane, deuterium was preferentially incorporated at the methyl positions as the methyl and methylene resonances integrate in a 10:1 ratio.

19 + HBCat + CO. An 18 mg (0.067 mmol) sample of **19** was dissolved in 0.6 mL toluene–d_8 and placed in a high pressure NMR tube. HBCat (8 μL, 0.07 mmol) was then added to the head space of the NMR tube which was sealed with a teflon plug. The tube is maintained as close to horizontal as possible to prevent a reaction from immediately occurring. The tube is immediately placed in a dry ice/isopropanol bath upon removal from the glove box. Once the toluene solution is cooled, the contents of the tube are allowed to react at –20 °C for 30 m. A ^{1}H NMR (–20 °C) is then taken to assure **20** had formed. The tube was then placed back in a dry ice/isopropanol bath and pressurized to 100 psi with CO. The contents of the tube were allowed to warm to room temperature. A ^{1}H NMR taken at 25 °C revealed the formation of **25** as the major product along with **2** and **18**.

Niobium Kinetics

*endo–***4** + CO. Typical sample preparation was as follows: *endo–***4** (5 mg, 0.00926 mmol) was dissolved in 0.550 mL toluene–d_8 with a gas free syringe. The solution was then placed in a high pressure NMR tube and closed. The NMR tube was removed from the glove box and cooled in a dry ice/isopropanol bath. The NMR tube was then loosely attached to a high pressure manifold while still immersed in the bath. The entire system was purged with CO for several minutes. The manifold/NMR tube adapter was then

tightened and the NMR tube opened to the CO manifold. The tube was pressurized to 200 psi. The pressure was released to roughly 30 psi by cracking at the NMR tube cap/manifold adapter junction and bleeding off excess CO. This cycle was repeated four times. The NMR tube was closed following the final pressurization. The NMR tube was removed from the manifold and kept in the cold bath. The NMR tube was quickly transferred from the cold bath to the NMR probe precooled to 0°C. The reaction was monitored through three half–lives with a kinetics program loaded on the NMR instrument. Data were analyzed using KaleidaGraph.

endo–4–d_2 + CO. The preparations and subsequent kinetic reactions were performed in the same manner as that described above.

endo–4 + X 4–tert–butyl catecholborane + CO. A typical preparation is as follows: endo–4 (5 mg, 0.00926 mmol) was dissolved in a minimal amount of toluene–d_8. To this solution varying quantities of 4–tert–butyl catecholborane was added followed by enough toluene–d_8 so the final volume was 0.550 mL. This solution was placed in a high pressure NMR tube which was then removed from the glove box. The pressurization of the NMR tube and the subsequent kinetics reaction was accomplished exactly as was above.

endo–4 + 4–tert–butyl catecholborane + X CO. A typical preparation is as follows: endo–4 (5 mg, 0.00926 mmol) was dissolved in a minimal amount of toluene–d_8 along with 10 mg of 4–tert–butyl catecholborane (0.0569 mmol). Additional toluene–d_8 was added so the final volume was 0.550 mL. This solution was placed in a high pressure NMR tube which was then removed from the glove box. The pre–pressurization of the NMR tube was followed as explained above with the final pressure cycle halted at various CO pressures.

endo–4 + CO at various temperatures. A typical sample preparation was as follows: endo–4 (5 mg, 0.00926 mmol) was dissolved in 0.550 mL toluene–d_8 with a gas free syringe. The solution was placed in a high pressure NMR tube which was then

removed from the glove box. Pressurization of the NMR tube was accomplished as described above. The NMR probe was cooled to different temperatures prior to the tube transfer. Data analysis was performed in the same manner as described above.

Tantalum Kinetics

endo–**17** + **CO.** Typical sample preparation was as follows: 5 mg *endo*–**17** (0.00797 mmol) was dissolved in 0.550 mL toluene–d_8 with a gas free syringe. The solution was then placed in a high pressure NMR tube and closed. The NMR tube was removed from the glove box and cooled in a dry ice/isopropanol bath. The NMR tube was then loosely attached to a high pressure manifold while still immersed in the bath. The entire system was purged with CO for several minutes. The manifold/NMR tube adapter was then tightened and the NMR tube opened to the CO manifold. The tube was pressurized to 100 psi. The pressure was released to roughly 30 psi by cracking at the NMR tube cap/manifold adapter junction and bleeding off excess CO. This cycle was repeated four times. The NMR tube was closed following the final pressurization. The NMR tube was removed from the manifold and heated in a constant temperature oil bath maintained at 70 °C. At recorded time intervals, the reaction was quenched by rapid cooling in an ice water bath. NMR were then recorded at ambient temperature. The progress of the reactions was monitored by the ratio of the intensity of the Cp* resonance of *endo*–**17** versus the total "intensity" of the Cp* resonances of *endo*–**17** and **32**. Data were analyzed using KaleidaGraph.

Equilibrium Measurements

endo–**4** + **HBO₂C₆H₃–3–'Bu.** Three independent NMR tubes were prepared in the same manner. *endo*–**4** (10.6 mg, 0.0196 mmol) was dissolved with 4.6 mg HBO₂C₆H₃–3–'Bu (0.0262 mmol) and 2 μL hexamethyldisiloxane (as a convenient internal standard) in 0.550 mL benzene–d_6. The resulting solution was loaded in a NMR tube and allowed to stand in the glove box. At three different time periods, ranging from 8 h to 2 d, NMR spectra were taken at 25 °C of each tube. Once equilibrium had been achieved, the

equilibrium constant was calculated using the integrated area of the respective methyl resonance of the four species in solution. The NMR tubes were stored in a glove box while spectra were not being acquired. All other equilibria experiments, using different catecholboranes and borane adduct compounds, were conducted in the same manner as described here, utilizing the integrated areas of convenient, well resolved resonances.

Single Crystal X–ray Structural Determinations and Refinement.

Determination and Refinement of *endo* and *exo*–1. Diffraction quality crystals of *endo*–1 and *exo*–1 were grown by slowly cooling concentrated toluene solutions to –80 °C. Crystals of *endo*–1·$(C_7H_8)_{1/2}$ were coated with Paratone–n and a suitable crystal was chosen and mounted on a glass fiber. Data were collected at –100 °C on a Rigaku AFC6 diffractometer using Mo Kα radiation (λ = 0.71069 Å). Cell parameters were determined from a list of reflections collected using an automated random search program. Three standard reflections were recollected after every 150 scanned reflections with no significant change in intensity noted. Crystals of *exo*–1 were mounted in similar fashion and data were collected at –85 °C on a Nicolet (Siemens P3) Autodiffractometer using Mo Kα radiation (λ = 0.71069 Å). Cell parameters were determined by least–squares analyses of 30 centered reflections chosen from precession photographs. Three standard reflections were recollected after every 150 scanned reflections with no significant change in intensity noted.

Structures were solved using direct methods and Patterson techniques available in the teXsan package of crystallographic programs and SHELXS–86. Positional and thermal parameters were refined using SHELXL–93 and the TEXSAN software. Ψ–scan based empirical absorption corrections were applied to each data set. All non–hydrogen atoms were refined anisotropically and difference maps revealed over 70% of the hydrogen atoms on the cyclopentadienyl and catecholate groups which justified using their calculated positions in later least–squares cycles. In both cases, hydride positions

were located in the final difference maps and positional and isotropic thermal parameters were refined in the last least–squares cycles.

endo–1 crystallized in a monoclinic crystal system with systematic absences indicating the space group $P2_1/n$ (#14) with the following cell parameters: a = 10.594(6) Å, b = 10.902(8) Å, c = 14.545(8) Å, β = 92.07(5)°, V = 1679(2) Å^3, Z = 4. Density (calculated) = 1.892 mg/cm^3. The 2686 independent reflections were collected between 4.66 ≤ 2Θ ≤ 49.9° using ω/2Θ scans. Full–matrix least–squares refinement on F^2 (2686 data, 100 restraints, 353 parameters) converged to give the following values: $R1$ = 0.0211, $wR2$ = 0.0503, GOF = 1.137 for [I > 2σ(I)]. For all data: $R1$ = 0.0357, $wR2$ = 0.1348. $R1 = \Sigma(F_o^2 - F_c^2)/\Sigma F_o^2$, $wR2 = [(w(F_o^2 - F_c^2)^2/\Sigma(F_o^2)^2)]^{1/2}$ and GOF = $(\Sigma(|F_o^2| - |F_c^2|)/\sigma)/(n - m)$ where $w = 1/\sigma^2(F_o^2)$, n is the number of reflections used and m is the number of variables.

exo–1 crystallized in a orthorhombic crystal system with systematic absences indicating the space group *Pbca* (#61) with the following cell parameters: a = 15.859(4) Å, b = 18.131(5) Å, c = 10.025(3) Å, V = 2882.6(14) Å^3, Z = 8. Density (calculated) = 1.991 mg/cm^3. The 3325 independent reflections were collected between 5.14 ≤ 2Θ ≤ 55.12° using ω/2Θ scans. Full–matrix least–squares refinement on F^2 (3325 data, 0 restraints, 246 parameters) converged to give the following values: $R1$ = 0.0452, $wR2$ = 0.0962, GOF = 1.062 for [I > 2σ(I)]. For all data: $R1$ = 0.0752, $wR2$ = 0.1098. $R1 = \Sigma(F_o^2 - F_c^2)/\Sigma F_o^2$, $wR2 = [(w(F_o^2 - F_c^2)^2/\Sigma(F_o^2)^2)]^{1/2}$ and GOF = $(\Sigma(|F_o^2| - |F_c^2|)/\sigma)/(n - m)$ where $w = 1/\sigma^2(F_o^2)$, n is the number of reflections used and m is the number of variables.

Determination and Refinement of *endo*–12. Data were collected at 173 K on a Rigaku AFC6 diffractometer using Mo Kα radiation (λ = 0.71069 Å). Final unit cell parameters were obtained by least–squares refinement of 25 reflections that had been accurately centered. Three standard reflections were recorded after every 150 scans, with no significant change in intensity noted. The structures were solved using SHELXL–86. Atomic coordinates and thermal parameters were refined using the full–matrix least–

squares program, SHELXL–93, and calculations were based on F^2 data. All non–hydrogen atoms were refined using anisotropic thermal parameters. All crystallographic computations were performed on Silicon Graphics Indigo computers.

Orange–red crystals of *endo*–**12** (fw 539.7) were grown from a toluene/heptane solution cooled to –35 °C. The crystals were coated with Paratone–N and a suitable crystal was selected and mounted on a glass fiber. Compound **12** crystallized in a triclinic crystal system with systematic absences indicating the space group P$\bar{1}$ (#2) with the following cell parameters: a = 9.923(3) Å, b = 12.109(4) Å, c = 13.588(4) Å, α = 97.74(2)°, β = 100.86(2)°, γ = 107.09(2)°, V = 1500.9 Å^3, Z = 2. Density (calculated) = 1.298 mg/cm^3. The 8555 independent reflections were collected between 4.0 ≤ 2Θ ≤ 60.0° using ω/2Θ scans.

All non–hydrogen atoms except one Cp* methyl carbon and the toluene solvent molecule were found using SHELXS–86. DIRDIF WFOUR was used to extend and initially "refine" the structure. The toluene solvent molecule was found and modeled later to fit the difference map peaks. SHELXL–93 was used to refine the structure. The hydrogen atoms of each Cp* methyl group were calculated as two sets of half–occupancy positions, rotated initially about the C–C bond by 60° from each other, and refined with occupancy factors of x and 1–x and with a common isotropic displacement parameter. Later, a single set of hydrogen atoms for each Cp* methyl group was placed at the occupancy–weighted average H positions. Restraints were applied separately to each methyl group to make all C–H distances the same, all H–H distances the same, all C–C–H angles the same, and to use a common isotropic displacement parameter. The hydrogen atoms of the boryl ring and its *tert*–butyl group were placed in calculated positions and refined independently without restraints. The toluene solvent molecule is disordered about an inversion center with both half–occupancy molecules coplanar and some atoms (e.g., C32 and C36*, etc.) nearly overlapping each other. The ring protons were restrained to lie 0.95 Å from their carbon atoms and equidistant from the two adjacent

95

carbon atoms. The seven carbon atoms and the five ring hydrogen atoms of the toluene molecule were restrained to lie in a plane. The methyl hydrogen atoms were treated as the Cp* methyl hydrogens above. Full–matrix least–squares refinement on F^2 (8548 data, 181 restraints, 462 parameters) converged to give the following values: $R1 = 0.0502$, $wR2 = 0.1220$, GOF = 1.067 for [$I > 2\sigma(I)$]. For all data: $R1 = 0.0730$, $wR2 = 0.1402$. $R1 = \Sigma(F_o^2 - F_c^2)/\Sigma F_o^2$, $wR2 = [(w(F_o^2 - F_c^2)^2/\Sigma(F_o^2)^2)]^{1/2}$ and GOF = $(\Sigma(|F_o^2| - |F_c^2|)/\sigma)/(n - m)$ where $w = 1/\sigma^2(F_o^2)$, n is the number of reflections used and m is the number of variables.

Determination and Refinement of 13. Data were collected at 173 K on a Rigaku AFC6 diffractometer using Mo Kα radiation ($\lambda = 0.71069$ Å). Final unit cell parameters were obtained by least–squares refinement of 25 reflections that had been accurately centered. Three standard reflections were recorded after every 150 scans, with no significant change in intensity noted. The structures were solved using SHELXL–86. Atomic coordinates and thermal parameters were refined using the full–matrix least–squares program, SHELXL–93, and calculations were based on F^2 data. All non–hydrogen atoms were refined using anisotropic thermal parameters. All crystallographic computations were performed on Silicon Graphics Indigo computers.

Green crystals of **13** (fw 377.7) were grown from a concentrated solution of heptane cooled to –35 °C. The crystals were coated with Paratone–N and a suitable crystal was selected and mounted on a glass fiber. Compound **13** crystallized in a monoclinic crystal system with systematic absences indicating the space group $P2_1/c$ (#14) with the following cell parameters: $a = 8.482(2)$ Å, $b = 25.306(6)$ Å, $c = 9.924(3)$ Å, $\beta = 113.84(2)°$, $V = 1948.39(9)$ Å^3, $Z = 4$. Density (calculated) = 1.298 mg/cm^3. The 3423 independent reflections were collected between $4.0 \leq 2\Theta \leq 50.0°$ using ω scans. All non–hydrogen atoms were located in the solution found by SHELXS–86. Methyl hydrogens for the Cp* ligand were placed in calculated positions (0.95 Å) and their isotropic thermal parameters were allowed to ride on the parent carbon atoms. The

hydrides were located in the difference–fourrier map and were refined isotropically. Full–matrix least–squares refinement on F^2 (3402 data, 30 restraints, 335 parameters) converged to give the following values: $R1 = 0.0455$, $wR2 = 0.1110$, GOF = 1.139 for [I > 2σ(I)]. For all data: $R1 = 0.1125$, $wR2 = 0.1566$. $R1 = \Sigma(F_o^2 - F_c^2)/\Sigma F_o^2$, $wR2 = [(w(F_o^2 - F_c^2)^2/\Sigma(F_o^2)^2)]^{1/2}$ and GOF = $(\Sigma(|F_o^2| - |F_c^2|)/\sigma)/(n - m)$ where $w = 1/\sigma^2(F_o^2)$, n is the number of reflections used and m is the number of variables.

Determination and Refinement for 18. Data were collected at 173 K on a Rigaku AFC6S diffractometer using Mo Kα radiation ($\lambda = 0.71069$ Å). Final unit cell parameters were obtained by least–squares refinement of 25 reflections that had been accurately centered. Three standard reflections were recorded after every 150 scans, with no significant change in intensity noted. The structures were solved using SHELXL–86 in the teXsan software package. Atomic coordinates and thermal parameters were refined using the full–matrix least–squares program, SHELXL–93, and calculations were based on F^2 data. All non–hydrogen atoms were refined using anisotropic thermal parameters. All crystallographic computations were performed on Silicon Graphics Indigo computers.

Lemon yellow crystals of **18** (fw 461.5) were grown from a concentrated acetone solution cooled to –80 °C. The crystals were coated with Paratone–N and a suitable crystal was selected and mounted on a glass fiber. Compound **18** crystallized in a monoclinic crystal system with systematic absences indicating the space group C2/c (#15) with the following cell parameters: $a = 15.585(6)$ Å, $b = 13.789(9)$ Å, $c = 12.701(7)$ Å, $\beta = 120.86(3)°$, $V = 2343(2)$ Å^3, $Z = 4$. Density (calculated) = 1.309 mg/cm^3. The 2029 independent reflections were collected between $4.0 \leq 2\Theta \leq 50.0°$ using $\omega/2\Theta$ scans.

All non–hydrogen atoms were located in the solution found by SHELXS–86. The hydrogen atoms of the Cp ring and the boryl ring were placed in calculated positions and refined independently without restraints. The hydride was located in the difference–fourrier map and was refined isotropically. Full–matrix least–squares refinement on F^2 (2029 data, 0 restraints, 184 parameters) converged to give the following values: $R1 =$

0.0542, $wR2$ = 0.1411, GOF = 1.077 for [I > 2σ(I)]. For all data: $R1$ = 0.1167, $wR2$ =

0.1771. $R1$ = $\Sigma(F_o^2 - F_c^2)/\Sigma F_o^2$, $wR2$ = $[(w(F_o^2 - F_c^2)^2/\Sigma(F_o^2)^2)]^{1/2}$ and GOF = $(\Sigma(|F_o^2| -$

$|F_c^2|)/\sigma)/(n - m)$ where w = $1/\sigma^2(F_o^2)$, n is the number of reflections used and m is the

number of variables.

Determination and Refinement for *endo*-17. Data were collected at 143 K on a

Siemens CCD diffractometer using Mo Kα radiation (λ = 0.71073 Å). Data were

collected as 90 second frames in a hemisphere of space. Final unit cell parameters were

obtained by least–squares refinement of accurately centered reflections obtained from 60

frames of collected data. Smart was employed to obtain a unit cell and Saint was utilized

to integrate the 1024 collected frames. SADABS was then used to apply absorption

corrections to the data. The structures were solved using SHELXL–86. Atomic

coordinates and thermal parameters were refined using the full–matrix least–squares

program, SHELXL–97, and calculations were based on F^2 data. All non–hydrogen atoms

were refined using anisotropic thermal parameters. All crystallographic computations

were performed on Silicon Graphics Indigo computers.

Colorless crystals of *endo*-17 (fw 628.4) were grown from a concentrated pentane

solution cooled to –35 °C. The crystals were coated with Paratone–N oil and a suitable

crystal was selected and mounted on a glass fiber. Compound **17** crystallized in a

monoclinic crystal system with systematic absences indicating the space group *C2/c*

(#15) with the following cell parameters: a = 36.608(7) Å, b = 9.974(2) Å, c = 15.702(3)

Å, β = 103.29(3)°, V = 5579.8(19) Å^3, Z = 8. Density (calculated) = 1.496 mg/cm^3. The

16046 independent reflections were collected between 4.14 ≤ 2Θ ≤ 56.72°.

All non–hydrogen atoms were found using SHELXS–86. DIRDIF WFOUR was

used to extend and initially "refine" the structure. SHELXL–97 was used to refine the

structure. The hydrogen atoms of each Cp* methyl group were placed in calculated

positions and allowed to "ride" their parent carbon atoms without restraints. Likewise,

hydrogen atoms of the catecholate ring and the *tert*-butyl group were placed in calculated

positions and allowed to "ride" their parent carbon atoms without additional restraints. The two hydrogen atoms bound to tantalum were found through difference maps and were refined isotropically. Full–matrix least–squares refinement on F^2 (6466 data, 0 restraints, 315 parameters) converged to give the following values: $R1 = 0.0716$, $wR2 = 0.1220$, $GOF = 1.053$ for $[I > 2\sigma(I)]$. For all data: $R1 = 0.0876$, $wR2 = 0.1462$. $R1 = \Sigma(F_o^2 - F_c^2)/\Sigma F_o^2$, $wR2 = [(w(F_o^2 - F_c^2)^2/\Sigma(F_o^2)^2)]^{1/2}$ and $GOF = (\Sigma(|F_o^2| - |F_c^2|)/\sigma)/(n - m)$ where $w = 1/\sigma^2(F_o^2)$, n is the number of reflections used and m is the number of variables.

APPENDICIES

Derivation of Model for Possible *endo*–1 Equilibrium
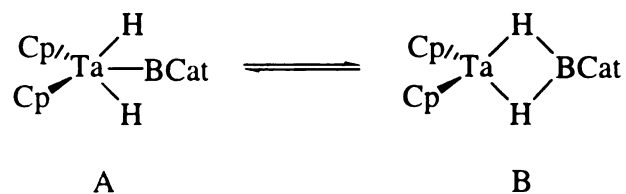
C_1 is defined as $e^{-\Delta E/RT}$ where R = 1.9872 cal/mol K

a is the mole fraction of A and b is the mole fraction of B

$C_1 = b/a$

$a + b = 1$

$b = 1 - a$

$C_1 = (1 - a)/a$

$C_1 = 1/a - 1$ $\qquad$ $b = 1 - [1/(C_1 + 1)]$

$C_1 + 1 = 1/a$ $\qquad$ $b = (C_1 + 1)/(C_1 + 1) - 1/(C_1 + 1)$

$1/(C_1 + 1) = a$ $\qquad$ $b = C_1/(C_1 + 1)$

$\delta_{obs} = a(\delta_A) + b(\delta_B)$

$\delta_{obs} = 1/(C_1 + 1)(\delta_A) + C_1/(C_1 + 1)(\delta_B)$

$\delta_{obs} = [\delta_A + C_1(\delta_B)]/(C_1 + 1)$

$\delta_{obs} = [\delta_A + e^{-\Delta E/RT}(\delta_B)]/(e^{-\Delta E/RT} + 1)$

APPENDIX B

Derivation of the Rate Law for Pathways C and D for the Reaction of 17 plus CO

$$\frac{-d\,[A]}{dt} \;=\; k_1\,[A] - k_{-1}\,[B]$$

$$\frac{d\,[B]}{dt} \;=\; k_1\,[A] - k_{-1}\,[B] - k_2\,[B][CO] + k_{-2}\,[C] = 0$$

$$\frac{d\,[C]}{dt} \;=\; k_2\,[B][CO] - k_{-2}\,[C] - k_3\,[C] = 0$$

$$k_2\,[B]\,[CO] \;=\; k_{-2}\,[C] + k_3\,[C]$$

$$k_2\,[B][CO] \;=\; [C](k_{-2} + k_3)$$

$$[C] \;=\; \frac{k_2\,[B]\,[CO]}{k_{-2} + k_3}$$

$$k_1\,[A] - k_{-1}\,[B] - k_2\,[CO]\,[B] + k_{-2}\left(\frac{k_2\,[B]\,[CO]}{k_{-2} + k_3}\right) = 0$$

$$k_{-1}\,[B] + k_2\,[CO]\,[B] - \left(\frac{k_{-2}\,k_2\,[B]\,[CO]}{k_{-2} + k_3}\right) = k_1\,[A]$$

$$\frac{k_{-2}\,k_2\,[B]}{k_{-2}+k_3} + \frac{k_{-1}\,k_3\,[B]}{k_{-2}+k_3} + \frac{k_{-2}\,k_2\,[B]\,\cancel{[CO]}}{\cancel{k_{-2}}+k_3} - \frac{k_{-2}\,k_2\,[B]\,\cancel{[CO]}}{\cancel{k_{-2}}+k_3} + \frac{k_2\,k_3\,[B]\,[CO]}{k_{-2}+k_3}$$

$$= k_1\,[A]$$

$$[B]\left\{\frac{k_{-2}\,k_2}{k_{-2}+k_3} + \frac{k_{-1}\,k_3}{k_{-2}+k_3} + \frac{k_2\,k_3\,[CO]}{k_{-2}+k_3}\right\} = k_1\,[A]$$

$$[B]\left\{\frac{k_{-2}\,k_2 + k_{-1}\,k_3 + k_2\,k_3\,[CO]}{k_{-2}+k_3}\right\} = k_1\,[A]$$

$$[B] = k_1\,[A]\left\{\frac{k_{-2}+k_3}{k_{-2}\,k_2 + k_{-1}\,k_3 + k_2\,k_3\,[CO]}\right\}$$

$$\frac{-d\,[A]}{dt} = k_1\,[A] - k_{-1}\ k_1\,[A]\left\{\frac{k_{-2}+k_3}{k_{-2}\,k_2\ +\ k_{-1}\,k_3\ +\ k_2\,k_3\,[CO]}\right\}$$

$$\frac{-d\,[A]}{dt} = k_1\,[A] - k_{-1}\,k_1\,[A]\left\{\frac{k_{-2}+k_3}{k_{-2}\,k_2\ +\ k_{-1}\,k_3\ +\ k_2\,k_3\,[CO]}\right\}$$

$$\frac{-d\,[A]}{dt} = [A]\ \ k_1 - \left\{\frac{k_1\,k_{-1}\,k_{-2}+k_1\,k_{-1}\ k_3}{k_{-2}\,k_2\ +\ k_{-1}\,k_3\ +\ k_2\,k_3\,[CO]}\right\}$$

at high [CO]: $\dfrac{-d\,[A]}{dt}\ =\ k_1\,[A]$

APPENDIX C

IR Spectroscopic Data for Cp′$_2$M(H$_2$BX$_2$) and Cp′$_2$MH$_3$ Compounds

Compound	$\nu_{BHM}(cm^{-1})^a$	$\nu_{MH}(cm^{-1})^a$
Cp*$_2$Nb(H$_2$BCat)[59]	1653	
Cp*$_2$Nb(H$_2$BCat′) (4)[59]	1653	
Cp*$_2$Nb(H$_2$BO$_2$C$_6$H$_3$–3–^{t}Bu) (12)[59]	1649	
Cp$_2$NbH$_2$(BCat)[20]	1742, 1675^b	
Cp$_2$Nb(H$_2$BC$_8$H$_{14}$)[20]	1605	
Cp$_2$NbH(BCat)$_2$ (18)[146]	1651	
Cp*$_2$NbBH$_4$ (13)[114]	1728, 1620	
Cp$_2$NbBH$_4$[147]	1745, 1628	
Cp*$_2$TaH$_2$(BCat)[59]	1774, 1709	
Cp*$_2$TaH$_2$(BCat′) (17)[59]	1767, 1720	
endo–Cp$_2$TaH$_2$(BCat) (endo–1)[60]	1768	
exo–Cp$_2$TaH$_2$(BCat) (exo–1)[60]	1771, 1703	
Cp*CpTaBH$_4$[137]	1747, 1621	
Cp$_2$TaBH$_4$[148]	1882–1860	
Cp*$_2$NbH$_3$[114]		1747, 1695
Cp$_2$NbH$_3$[149]		1710
Cp*$_2$TaH$_3$ (33)[68]		1750, 1720
Cp$_2$TaH$_3$[150]		1735

^{a} Recorded as Nujol mulls unless otherwise indicated. ^{b} KBr pellet.

REFERENCES

REFERENCES

(1) Grimes, R. N. *Transition Metal Metallacarboranes*; Pergammon: New York, 1995; Vol. 1, pp 373–430.

(2) Braunschweig, H.; Kollann, C.; Englert, U. *Angew. Chem., Int. Ed. Engl.* **1998**, *37*, 3179–3180.

(3) Peters, J. C.; Odom, A. L.; Cummins, C. C. *J. Chem. Soc., Chem. Commun.* **1997**, 1995–1996.

(4) Braunschweig, H. *Angew. Chem., Int. Ed. Engl.* **1998**, *37*, 1786–1801.

(5) Irvine, G. J.; Lesley, M. J. G.; Marder, T. B.; Norman, N. C.; Rice, C. R.; Robins, E. G.; Roper, W. R.; Whittell, G. R.; Wright, L. J. *Chem. Rev.* **1998**, *98*, 2685–2722.

(6) Wadepohl, H. *Angew. Chem., Int. Ed. Engl.* **1997**, *36*, 2441–2444.

(7) Miyaura, N.; Suzuki, A. *Chem. Rev.* **1995**, *95*, 2457–2483.

(8) Littke, A. F.; Fu, G. C. *Angew. Chem., Int. Ed.* **1998**, *37*, 3387–3388.

(9) Fischer, E. O.; Maasböl, A. *Angew. Chem., Int. Ed. Engl.* **1964**, *3*, 580–581.

(10) Gagné, M. R.; Marks, T. J. *J. Am. Chem. Soc.* **1989**, *111*, 4108–4109.

(11) Gagné, M. R.; Nolan, S. P.; Marks, T. J. *Organometallics* **1990**, *9*, 1716–1718.

(12) Gagné, M. R.; Stern, C. L.; Marks, T. J. *J. Am. Chem. Soc.* **1992**, *114*, 275–294.

(13) Gagné, M. R.; Brard, L.; Conticello, V. P.; Giardello, M. A.; Stern, C. L.; Marks, T. J. *Organometallics* **1992**, *11*, 2003–2005.

(14) Beletskaya, I.; Pelter, A. *Tetrahedron* **1997**, *53*, 4957–5026.

(15) Harrison, K. M.; Marks., T. J. *J. Am. Chem. Soc.* **1992**, *114*, 9220–9221.

(16) Seyferth, D.; Raab, G.; Grim, S. O. *J. Org. Chem.* **1961**, *26*, 3034–3035.

(17) Johnson, M. P.; Shriver, D. F.; Shriver, S. A. *J. Am. Chem. Soc.* **1966**, *88*, 1588–1589.

(18) Nöth, H.; Schmid, G. *Angew. Chem., Int. Ed. Engl.* **1963**, *2*, 623.

(19) Kono, H.; Ito, K.; Nagai, Y. *Chem. Lett.* **1975**, 1095–1096.

(20) Hartwig, J. F.; De Gala, S. R. *J. Am. Chem. Soc.* **1994**, *116*, 3661–3662.

(21) Johnson, M. P.; Shriver, D. F. *J. Am. Chem. Soc.* **1963**, *85*, 3509–3510.

(22) Braunschweig, H.; Wagner, T. *Chem. Ber.* **1994**, *127*, 1613–1614.

(23) Braunschweig, H.; Wagner, T. *Z. Naturforsch. Sect. B* **1996**, *51*, 1618–1620.

(24) Baker, R. T.; Ovenall, D. W.; Calabrese, J. C.; Westcott, S. A.; Taylor, N. J.; Williams, I. D.; Marder, T. B. *J. Am. Chem. Soc.* **1990**, *112*, 9399–9400.

(25) Westcott, S. A.; Taylor, N. J.; Marder, T. B.; Baker, R. T.; Jones, N. L.; Calabrese, J. C. *J. Chem. Soc., Chem. Commun.* **1991**, 304–305.

(26) Nguyen, P; Blom, H. P.; Westcott, S. A.; Taylor, N. J.; Marder, T. B. *J. Am. Chem. Soc.* **1993**, *115*, 9329–9330.

(27) Hartwig, J. F.; Huber, S. *J. Am. Chem. Soc.* **1993**, *115*, 4908–4909.

(28) Männig, D.; Nöth, H. *Angew. Chem., Int. Ed. Engl.* **1985**, *24*, 878–879.

(29) Burgess, K.; Ohlmeyer, M. J. *Chem. Rev.* **1991**, *91*, 1179–1191.

(30) Dorigo, A. E.; Schleyer, P. v. R. *Angew. Chem., Int. Ed. Engl.* **1995**, *34*, 115–118.

(31) Musaev, D.G; Mebal, A. M.; Morokuma, K. *J. Am. Chem. Soc.* **1994**, *116*, 10693–10792.

(32) Baker, R. R.; Calabrese, J. C.; Westcott, S. A.; Nguyen, P.; Marder, T. B. *J. Am. Chem. Soc.* **1993**, *115*, 4367–4368.

(33) Hartwig, J. F.; Bhandari, S.; Rablen, P. R. *J. Am. Chem. Soc.* **1994**, *116*, 1839–1844.

(34) Pereira, S.; Srebnik, M. *Organometallics* **1995**, *14*, 3127–3128.

(35) Westcott, S. A.; Blom, H. P.; Marder, T. B.; Baker, R. T.; Calabrese, J. C. *Inorg. Chem.* **1993**, *32*, 2175–2182.

(36) Burgess, K.; Jaspars, M. *Tetrahedron Lett.* **1993**, *34*, 6813–6816.

(37) He, X.; Hartwig, J. F. *J. Am. Chem. Soc.* **1996**, *118*, 1696–1702.

(38) Bijpost, E.A.; Duchateau, R.; Teuben, J.H. *J. Mol. Cat. A: Chem.* **1995**, *95*, 121–128.

(39) Motry, D. H.; Smith, M. R., III *J. Am. Chem. Soc.* **1995**, *117*, 6615–6616.

(40) Motry, D. H.; Brazil, A. G.; Smith, M. R., III *J. Am. Chem. Soc.* **1997**, *119*, 2743–2744.

(41) Motry, D. H. Ph. D. Thesis, Michigan State University, 1995.

(42) Bunker, M. J.; De Cian, A.; Green, M. L. H.; Moreau, J. J. E.; Siganporia, N. *J. Chem. Soc., Dalton Trans.* **1980**, 2155–2161.

(43) The endo/exo designation refers to stereochemical orientations within the metallocene wedge. For the olefin complexes $Cp'_2MH(\eta^2–CH_2=CHMe)$, the propylene

β–C of the endo isomer occupies the central position in the metallocene wedge, while the propylene β–C of the exo isomer coordinates at an external site. Similar designations for Cp'_2MH_2BCat complexes refer to orientation of the BCat group.

(44) The isomeric silylhydrides were not separated as pure compounds.

(45) Lauher, J. W.; Hoffman, R. *J. Am. Chem. Soc.* **1976**, *98*, 1729–1742.

(46) Manriquez, J. M.; McAlister, D. R.; Sanner, R. D.; Bercaw, J. E. *J. Am. Chem. Soc.* **1976**, *98*, 6733–6735.

(47) Erker, G.; Rosenfeldt, F. *Angew. Chem., Int. Ed. Engl.* **1978**, *17*, 605–606.

(48) Glusker, J. P.; Trueblood, K. N. *Crystal Structure Analysis*; 2nd ed.; Oxford University Press: New York, 1985.

(49) Wilson, R. D.; Koetzle, T. F.; Hart, D. W.; Kvick, Å.; Tipton, D. L.; Bau, R. *J. Am. Chem. Soc.* **1977**, *99*, 1775–1781.

(50) Hartwig, J. F.; Muhoro, C. N.; He, X.; Eisenstein, O.; Bosque, R.; Maseras, F. *J. Am. Chem. Soc.* **1996**, *118*, 10936–10937.

(51) Saunders, M.; Telkowski, L.; Kates, M. R. *J. Am. Chem. Soc.* **1977**, *99*, 8070–8071.

(52) Saunders, M.; Kates, M. R. *J. Am. Chem. Soc.* **1977**, *99*, 8071–8072.

(53) Jameson, C. J.; Osten, H. J. *Annu. Rep. NMR Spectroscop.* **1986**, *17*, 1.

(54) Vibrational zero point energies can be expressed as a function of the force constant and the reduced mass by using simple harmonic oscillator approximations: $E_n = (n + \frac{1}{2})(hc\omega)$, where ω is the vibrational constant equal to $\{1/(2\pi c)\}(k/\mu)^{1/2}$. The force constant is k and the reduced mass is μ. The reduced mass $(\mu) = m_1m_2/(m_1+ m_2)$. Because of deuterium's larger mass, the zero point energies of deuterium isotopomers will be lower than their hydrogen compliments. If the force constants for the hydride vibrational modes are not the same in the two limiting structures, deuteration will shift the equilibrium between the two structures. In a limiting structure, the change of nuclear mass (changing isotopes) will not affect the electronic energy of a system. The force constant (k) and the depth of the potential energy well will remain unchanged with the only change manifesting in the reduced mass (μ) of the system. If equilibrium is rapid on the NMR time scale, the observed hydride shift will be a weighted average of the chemical shifts for the hydride ligands of the limiting structures, and the isotopic perturbation or the equilibrium between the two extremes will lead to a shift in the hydride/deuteride resonance. The large chemical shift perturbations provide strong evidence for equilibrium between structural extremes in this system but the structures that participate in the equilibria cannot be unambiguously assigned from the data.

(55) Balzer, H. H.; Berger, S. *J. Phys. Org. Chem.* **1997**, *10*, 187–189.

(56) Friebolin, H. P. *Basic One– and Two–Dimensional NMR Spectroscopy*; VCH Publishers: New York, 1991.

(57) Drago, R. S. *Physical Methods for Chemists*; 2nd ed.; Saunders College Publishing: Orlando, Fl, 1992.

(58) Oldham, W. J. Jr.; Hinkle, A. S.; Heinekey, D. M. *J. Am. Chem. Soc.* **1997**, *119*, 11028–11036.

(59) Lantero, D. R.; Ward, D. L.; Smith, M. R., III *J. Am. Chem. Soc.* **1997**, *119*, 9699–9708.

(60) Lantero, D. R.; Motry, D. H.; Ward, D. L.; Smith, M. R., III *J. Am. Chem. Soc.* **1994**, *116*, 10811–10812.

(61) Heinekey, D. M.; Oldham, W. J. Jr. *J. Am. Chem. Soc.* **1994**, *116*, 3137–3138.

(62) An equilibrium consisting of three compounds (a Ta^V dihydridoboryl, a Ta^{III} borohydride and a Ta^{III} borane adduct complex) in solution, while possible, was not modeled.

(63) Jameson, C. J. *J. Chem. Phys.* **1977**, *66*, 4977–4982.

(64) Jameson, C. J. *J. Chem. Phys.* **1977**, *66*, 4893–4988.

(65) A possible explanation for the downfield chemical shift of the hydride resonances can be attributed to an interaction between the Ta–H electrons and the atomic orbitals of the other atoms in the metallocene wedge. The atomic orbitals can serve to siphon electron density from the bond which reduces the shielding of the hydride ligand causing a downfield shift in resonance. There is not a static structure of the boryl fragment with the boryl fragment plane orthogonal to the metallocene wedge plane in solution which limits the utility of this explanation. Another possible explanation deals with the ring current from the catecholate ligand interacting with the hydride ligands. The boryl fragment plane is orthogonal to the metallocene wedge plane in the limiting structure in the solid state which would serve to further shield the hydride ligands and shift the resonance upfield. Because the chemical shift moves downfield, this explanation would also be of limited usefulness.

(66) Collman, J. P.; Hegedus, L. S.; Norton, J. R.; Finke, R. G. *Principles and Applications of Organotransition Metal Chemistry*; University Science Books: Mill Valley, CA, 1987, pp 167.

(67) If dihydride intermediates are involved, the failure to detect deuterated borane porducts would require that $k_H/k_D > 50$.

(68) Gibson, V. C.; Bercaw, J. E.; Bruton, W. J.; Sanner, R. D. *Organometallics* **1986**, *5*, 976–979.

(69) Kirillova, N. I.; Gusev, A. I.; Struchkov, Y. T. *J. Struct. Chem. USSR* **1974**, *15*, 622–624.

(70) Bailey, N. J.; Green, M. L. H.; Leech, M. A.; Saunders, J. F.; Tidswell, H. M. *J. Organomet. Chem.* **1997**, *538*, 111–118.

(71) Müller, G.; Krüger, C *Acta Crystallogr.* **1986**, *C42*, 1856–1859.

(72) Yalpani, M.; Boese, R.; Köster, R. *Chem. Ber.* **1990**, *123*, 1285–1291.

(73) Yalpani, M.; Köster, R.; Boese, R. *Chem. Ber.* **1993**, *126*, 565–570.

(74) Boese, R.; Köster, R.; Yalpani, M. *Z. Naturforsch.* **1994**, *49B*, 1453–1458.

(75) *Internation Tables for X–Ray Crystallography*; The Kynoch Press: Birmingham, England, 1968; Vol. 3.

(76) Sanner, R. D.; Manriquez, J. M.; Marsh, R. E.; Bercaw, J. E. *J. Am. Chem. Soc.* **1976**, *98*, 8351–8357.

(77) Sanner, R. D.; Duggan, D. M.; McKenzie, T. C.; Marsh, R. E.; Bercaw, J. E. *J. Am. Chem. Soc.* **1976**, *98*, 8358–8365.

(78) Berry, D. H.; Procopio, L. J.; Carroll, P. J. *Organometallics* **1988**, *7*, 570–572.

(79) Edema, J. J. H.; Meetsma, A.; Gambarotta, S. *J. Am. Chem. Soc.* **1989**, *111*, 6878–6880.

(80) Dilworth, J. R.; Henderson, R. A.; Hills, A.; Hughes, D. L.; Macdonald, C.; Stephens, A. N.; Walton, D. R. M. *J. Chem. Soc. Dalton Trans.* **1990**, 1077–1085.

(81) Desmangles, N.; Jenkins, H.; Ruppa, K. B.; Gambrotta, S. *Inorg. Chim. Acta* **1996**, *250*, 1–4.

(82) Buijink, J.-K.; Meetsma, A.; Teuben, J. H. *Organometallics* **1993**, *12*, 2004–2005.

(83) Hao, S.; Berno, P.; Minhas, R. K.; Gambarotta, S. *Inorg. Chim. Acta* **1996**, *244*, 37–49.

(84) Song, J.-I.; Berno, P.; Gambrotta, S. *J. Am. Chem. Soc.* **1994**, *116*, 6927–6928.

(85) Churchill, M. R.; Wasserman, H. J. *Inorg. Chem.* **1982**, *21*, 218–222.

(86) Churchill, M. R.; Wasserman, H. J. *Inorg. Chem.* **1981**, *20*, 2899–2904.

(87) Berno, P.; Hao, S.; Minhas, R.; Gambrotta, S. *J. Am. Chem. Soc.* **1994**, *116*, 7417–7418.

(88) Turner, H. W.; Fellmann, J. D.; Rocklage, S. M.; Schrock, R. R.; Churchill, M. R.; Wasserman, H. J. *J. Am. Chem. Soc.* **1980**, *102*, 7809–7811.

(89) Berno, P.; Gambarotta, S. *Organometallics* **1995**, *14*, 2159–2161.

(90) Schrock, R. R.; Wesolek, M.; Liu, A. H.; Wallace, K. C.; Dewan, J. C. *Inorg. Chem.* **1988**, *27*, 2050–2054.

(91) The assignment of the resonances due to each isomer is not trivial. The original assignment of the Cp resonances for the two isomers was incorrect (ref 93). A subsequent reinvestigation of these complexes correctly identified the resonances of the each isomer (ref 115).

(92) Although B–H activation in Figure 42 is depicted as preceding through oxidative addition/reductive elimination sequences, a mechanism predicated on σ-bond metathesis is also plausible.

(93) Klazinga, A. H.; Teuben, J. H. *J. Organomet. Chem.* **1980**, *194*, 309–316.

(94) Otto, E. E. H.; Brintzinger, H. H. *J. Organomet. Chem.* **1978**, *148*, 29–33.

(95) A conceivable, but unlikely, scenario could lead to temperature independent shifts for equilibrating structures. If entropic contributions to ΔG for the borane adduct and the diborylhydride (or any other equilibrating structures) are identical, or the limiting hydride chemical shifts for different structures are coincident, the equilibrium could be temperature dependent.

(96) A process that rapidly exchanges coordinated and uncoordinated oxygen atoms would give two resonances. This exchange would not effect arguments based on $|^1J_{HB}|$, chemical shift or isotope effects on chemical shifts.

(97) Curtis, M. D.; Bell, L. G.; Butler, W. M. *Organometallics* **1985**, *4*, 701–707.

(98) Heinekey, D. M. *J. Am. Chem. Soc.* **1991**, *113*, 6074–6077.

(99) Deutsch, P. P.; Maguire, J. A.; Jones, W. D.; Eisenberg, R. *Inorg. Chem.* **1990**, *29*, 686–690.

(100) Cho, J.-Y., personal communication.

(101) There was no significant electron density located between B and B(A).

(102) Hartwig, J. F.; He, X. *Organometallics* **1996**, *15*, 5350–5358.

(103) Prout, K; Cameron, T. S.; Forder, R.. A. *Acta Crystallogr. B* **1974**, *30*, 2290–2304.

(104) Using an average estimate for a Nb–H distance (1.65 Å), and the extrema for B–H distances in catecholate complexes where B–H interactions are significant, the estimated range for the angle defined by the midpoint of the B–H vector, Nb, and the *exo* boryl ligand is 80 > θ > 74. This value is typical for a d^2 complex and smaller than the range for X–M–X angle in d^0 complexes (94–97°). Clearly this comparison suffers from the ill-defined hydride position in the diboryl compound. Furthermore, the electronic–based argument neglects potential steric contributions, and the inherent asymmetry in the diboryl compound may limit direct comparison to $Cp_2Ti(\eta^2-HBCat)_2$.

(105) Iverson, C. N.; Smith, M. R., III *J. Am. Chem. Soc.* **1995**, *117*, 4403–4404.

(106) Nguyen, P.; Lesley, G.; Taylor, N. J.; Marder, T. B.; Pickett, N. L.; Clegg, W.; Elsegood, M. R. J.; Norman, N. C. *Inorg. Chem.* **1994**, *33*, 4623–4624.

(107) Hartwig, J. F.; He, X. *Angew. Chem., Int. Ed. Engl.* **1996**, *35*, 315–317.

111

(108) Ishiyama, T.; Matsuda, N.; Murata, M.; Ozawa, F.; Suzuki, A.; Miyaura, N. *Organometallics* **1996**, *15*, 713–720.

(109) Lesley, G.; Nguyen, P.; Taylor, N. J.; Marder, T.B.; Scott, A. J.; Clegg, W.; Norman, N. C. *Organometallics* **1996**, *15*, 5137–5154.

(110) Dai, C.; Stringer, G.; Marder, T.B.; Baker, R.T.; Scott, A.J.; Clegg, W.; Norman, N.C. *Can. J. Chem.* **1996**, *74*, 2026–2030.

(111) Dai, C.; Stringer, G.; Corrigan, J. F.; Taylor, N. J.; Marder, T. B.; Norman, N. C. *J. Organomet. Chem.* **1996**, *513*, 273–275.

(112) Jiang, Q.; Carroll, P. J.; Berry, D. H. *Organometallics* **1991**, *10*, 3648–3655.

(113) Nikonov, G. I.; Kuzmina, L. G.; Lemenovskii, D. A.; Kotov, V.V. *J. Am. Chem. Soc.* **1995**, *117*, 10133–10134.

(114) Bell, R. A.; Cohen, S. A.; Doherty, N. M.; Threlkel, R. S.; Bercaw, J. E. *Organometallics* **1986**, *5*, 972–975.

(115) Burger, B. J.; Santarsiero, B. D.; Trimmer, M. S.; Bercaw, J. E. *J. Am. Chem. Soc.* **1988**, *110*, 3134–3146.

(116) β–H elimination from the intermediate $Cp_2TaH(CH_2CHDCH_3)$ will yield *endo*–$Cp_2TaH(CH_2=CD(Me))$ while $Cp_2TaH(CH(CH_2D)CH_3)$ can give *exo*–$Cp_2TaH(CHD=CH(Me))$ or *exo*–$Cp_2TaH(CH_2=CH(CH_2D))$ upon β–H elimination.

(117) Schrock, R. R.; Sharp, P. R. *J. Am. Chem. Soc.* **1978**, *100*, 2389–2399.

(118) van Asselt, A.; Burger, B. J.; Gibson, V. C.; Bercaw, J. E. *J. Am. Chem. Soc.* **1986**, *108*, 5347–5349.

(119) Integration of the Ta deuteride and alkylborane resonances in the ^2H NMR spectrum gives a ratio that predicts preferential deuterium incorporation in the alkylborane. Proton incorporation that can arise from exchange of Ta–D bonds and adventitious proton sources makes integration of the ^2H resonances unreliable for determining the extent of deuterium incorporation in the alkylborane product. Thus, the deuterium incorporation is more accurately determined by integrating the propyl resonances in the ^1H spectrum of *n*–PrBCat.

(120) Doherty, N. M.; Bercaw, J. E. *J. Am. Chem. Soc.* **1985**, *107*, 2670–2682.

(121) Suzuki, A.; Dhillon, R. S. *Top. Curr. Chem.* **1986**, *130*, 23–88.

(122) Collman, J. P.; Finke, R. G.; Matlock, P. L.; Wahren, R.; Komoto, R. G.; Brauman, J. I. *J. Am. Chem. Soc.* **1978**, *100*, 1119–1140.

(123) Sweany, R. L.; Halpern, J. *J. Am. Chem. Soc.* **1977**, *99*, 8335–8337.

(124) Roth, J. A.; Orchin, M. *J. Organomet. Chem.* **1979**, *182*, 299–311.

(125) Sweany, R. L.; Comberrel, D. S.; Dombourian, M. F.; Peters, N. A. *J. Organomet. Chem.* **1981**, *216*, 57–63.

(126) Sweany, R. L.; Butler, S. C.; Halpern, J. *J. Organomet. Chem.* **1981**, *213*, 487–492.

(127) Halpern, J. *Pure Appl. Chem.* **1986**, *58*, 575–584.

(128) Nalesnik, T. E.; Orchin, M. *J. Organomet. Chem.* **1980**, *199*, 265–269.

(129) Nalesnik, T. E.; Freudenberger, J. H.; Orchin, N. A. *J. Mol. Catal.* **1982**, *16*, 43–49.

(130) Roth, J. A.; Wiseman, P.; Ruzzala, L. *J. Organomet. Chem.* **1983**, *240*, 271–275.

(131) Wilkins, R. G. *Kinetics and Mechanisms of Transition Metal Complexes*; VCH: Weiheim, 1991, pp 109.

(132) Crespo, M.; Martinez, M.; de Pablo, E. *J. Chem. Soc., Dalton Trans.* **1997**, 1231–1235.

(133) Bullock, R. M.; Headford, C. E. L.; Hennessy, K. M.; Kegley, S. E.; Norton, J. R. *J. Am. Chem. Soc.* **1989**, *111*, 3897–3908.

(134) Parkin, G.; Bercaw, J. E. *Organometallics* **1989**, *8*, 1172–1179.

(135) Jones, W. D.; Feher, F. J. *J. Am. Chem. Soc.* **1986**, *108*, 4814–4819.

(136) Green, M. L. H.; Wong, L.-L. *J. Chem. Soc., Dalton Trans.* **1989**, 2133–2138.

(137) Green, M. L. H.; Wong, L.-L. *J. Chem. Soc., Chem. Commun.* **1989**, 571–573.

(138) O'Conner, J. M.; Casey, C. P. *Chem. Rev.* **1987**, *87*, 307–318.

(139) Parkin, G.; Bercaw, J. E. *J. Am. Chem. Soc.* **1989**, *111*, 391–393.

(140) The rate law for pathways C and D is –d[A]/dt = k_1[A] under high CO pressures. See Appendix B for a complete derivation of the rate law.

(141) Kerr, J. A. *Strengths of Chemical Bonds*; 71st ed.; CRC Press: Boca Raton, Ann Arbor, London,Tokyo, 1990.

(142) Rablen, P.R.; Hartwig, J.F. *J. Am. Chem. Soc.* **1996**, *118*, 4648–4653.

(143) Klazinga, A. H.; Teuben, J. H. *J. Organomet. Chem.* **1978**, *157*, 413–419.

(144) Lichtenberger, D. L.; Darsey, G. P.; Kellogg, G. E.; Sanner, R. D.; Young, V. G., Jr.; Clark, J. R *J. Am. Chem. Soc.* **1989**, *111*, 5019–5028.

(145) Brown, H. C.; Gupta, S. K. *J. Am. Chem. Soc.* **1975**, *97*, 5249–5255.

(146) Lantero, D. R.; Miller, S. L.; Cho, J.-Y.; Ward, D. L.; Smith, M. R., III *Organometallics* **1999**, *18*, 235–247.

(147) Lucas, C. R.; Green, M. L. H. *J. Chem. Soc., Chem Commun.* **1972**, 1005.

(148) Antiñolo, A.; Fajardo, M.; Otero, A.; Royo, P. *J. Organomet. Chem.* **1983**, *246*, 269–278.

(149) Tebbe, F. N.; Parshall, G. W. *J. Am. Chem. Soc.* **1971**, *93*, 3793–3795.

(150) Green, M. L. H.; McCleverty, J. A.; Pratt, L.; Wilkinson, G. *J. Chem. Soc.* **1961**, 4854–4859.